GEOSCIENCES AND ENGINEERING

A Publication of the University of Miskolc

Volume 2, Number 3 (2013)

Miskolc University Press
2013

GEOSCIENCES AND ENGINEERING
A Publication of the University of Miskolc

Volume 2, Number 3
Miskolc University Press, 2013

UNIVERSITY OF MISKOLC
FACULTY OF EARTH SCIENCE & ENGINEERING

ISSN 2063-6997

EDITORIAL BOARD

Chairman of the Editorial Board:	Dr. h. c. mult. Ferenc Kovács, member of HAS
Editor-in-chief:	Prof. Dr. Gábor Takács DSc
Secretary:	Dr. Ljudmilla Bokányi CSc, Associate Professor
Members:	Dr. Tibor Bódi PhD, Associate Professor
	Prof. Dr. Barnabás Csőke CSc
	Dr. Ákos Debreczeni CSc, Associate Professor
	Dr. Endre Dobos PhD, Associate Professor
	Prof. Dr. Mihály Dobróka DSc
	Prof. Dr. János Földessy CSc
	Prof. Dr. György Less DSc
	Dr. Ferenc Mádai PhD, Associate Professor
	Dr. József Molnár CSc, Associate Professor
	Prof. Dr. Péter Szűcs DSc
	Prof. Dr. László Tihanyi CSc

From the Editor

The Editorial Board would like to express their sincere gratitude to **all our Hungarian and foreign Reviewers** for their correct and precise work of a great value that contributed very much to the high standard of this Volume.

* * *

The Editorial Board regrets to announce that the paper entitled "Application of GMT (Generic Mapping Tools) software for volume computation in mining industry" as published in Vol. 1, No. 1 of our Journal (pp. 139–145) contained a printing error and the author names were improperly given.

The authors of this paper are as follows

István Havasi–Marcell Ferenc

Our sincere apologies for the mistake.

Miskolc, July 1, 2013

Prof. Dr. Gábor TAKÁCS
Editor-in Chief

Preface

The publication of the present issue of Geosciences and Engineering was financially fully supported by the TÁMOP-4.2.2/B-10/1-2010-0008 project in the framework of the New Hungarian Development Plan. The realization of this TÁMOP project is supported by the European Union, co-financed by the European Social Fund.

I am proud to inform the distinguished Reader that this issue includes 13 high quality publications from the supervisors and the PhD students of the Mikoviny Sámuel Earth Science Doctoral Schools. One of the main objectives of the above-mentioned TÁMOP project was to care the most talented PhD students belonging to the Faculty of Earth Science and Engineering. This project will be finished at the end of September, 2013 after a two-year-long successful operation. A substantial financial support, altogether 46 million HUF, was spent on different project elements like PhD scholarships, conference mobility, professional short courses, scientific books, laboratory materials and publications during this time period. As a result of the project operation, we could witness significant improvements in our educational and research programs at the Doctoral School. This special issue of Geosciences and Engineering can also prove the increased research activity of our talented PhD students conducting different challenging topics. Due to this promising activity, more and more students have had the opportunity to defend their PhD theses work.

I personally thank the Editor-Chief, Prof. Dr. Gábor Takács and the Secretary of the Editorial Board, Assoc. Prof. Dr. Ljudmilla Bokányi for their efforts and high quality work to finalize the manuscripts and the whole issue after the review process.

Miskolc-Egyetemváros, July 8, 2013

Prof. Dr. Péter Szűcs
dean

CONTENTS

From the Editor 3

Preface 5

L. Tihanyi–I. Szunyog: CO_2 Emission Trends in Hungary 9

L. Kompár–E. Dobos–P. Szűcs: The Estimation of Natural Groundwater Recharge on the Example of Two Research Sites 19

G. Takács: Detailed Design of an ESP Installation for a Geothermal Well 25

B. Csuhanics–Á. Debreczeni: Development of Automatic Control of Multi-Stage Triaxial Tests at the University of Miskolc 37

M. Tóth–F. Móricz–B. Kovács: Investigation of Heavy Metals Extraction Surface of a Waste Dump of Rudabánya 45

G. Pethő: Bases of FD Modelling for EM Underground Transillumination with Vertical Electric Dipoles in 2D Anisotropic Conductivity Structures 51

J. Somogyi Molnár–M. Dobróka–T. Bodoky: Explanation of Pressure Dependence of Acoustic Velocity Based on the Change of Pore Volume 63

A. N. Paripás–T. Ormos: New Inversion Technique for the Elimination of Trigger Errors in Seismic Refraction Data 73

H. Szegedi–M. Dobróka–T. Bodoky: New Inversion Algorithm for the Computation of Fourier Transform – Examination on a Synthetic Data Set 83

L. Lénárt–E. Szegediné Darabos: The Hydrogeological Relations of the Thermal Karst of the Bükk Mountains Based on Monitoring Data 91

Z. Fejes–P. Szűcs: Potential Tepid and Hot Water Resources in the Tokaj Mountains 101

N. Gonda–B. Kovács: Vacuum Enhanced Compression of Recsk Type Flotation Slurry 111

T. Hauck: Bioenergy Production in Mátra Power Plant 117

Geosciences and Engineering, Vol. 2, No. 3 (2013), pp. 9–17.

CO_2 EMISSION TRENDS IN HUNGARY

LÁSZLÓ TIHANYI[1]–ISTVÁN SZUNYOG[2]
Petroleum and Natural Gas Institute, University of Miskolc
H-3515 Miskolc-Egyetemváros, Hungary
[1]tihanyil@kfgi.uni-miskolc.hu, [2]szunyogi@kfgi.uni-miskolc.hu

ABSTRACT

At the end of 2010, Hungarian authorities issued a national action plan on the use of renewables in the energy system, and a year later the Parliament adopted a document entitled National Energy Strategy 2030 (in Oct, 2011). Both documents primarily focus on the climate challenge, targeting substantial reduction in current CO_2 emission. Based on the statistical analysis of national and international fuel consumption data, this paper tends to summarize past trends and give projections on the future perspectives of feasible decarbonisation options.

INTRODUCTION

Scientific research conducted on arctic ice cores and marine deposit samples estimate the original level of atmospheric CO_2 content to have been between 180 *ppm* - 300 *ppm* along the past 650 000 years. Since the industrial revolution, the amount of CO_2 in the atmosphere has increased from 280 *ppm* to about 385 *ppm*, and is still being at a constant rise. According to the International Energy Agency (IEA) database, in 2010 cca. 30 billion tonnes of CO_2 was emitted into the atmosphere. The values are appalling.

As for methane concentration, the rise is even more drastic: the past few centuries produced a shift from a natural level of 715 *ppb* (parts per billion) to approximately 1 774 *ppb*. Considering the summed total concentration of greenhouse gases (GHG) in the atmosphere, we get as much as 445 *ppm* (expressed in carbon dioxide equivalent). This value exceeds the level of the pre-industrialized period by about 60%.

Diversifying the above data by emissive sources, surveys show that 41% of total CO_2 emission derives from electricity and heat generation, 23% comes from transport, 20% and 6% is produced by the industrial and residential sectors, respectively. The most substantial shares are attributable to carbon-based energy generation worldwide. Australia, China, India and Poland for instance, still provide 70–90% of their domestic electricity supply from coal-fired plants. The prior emittants are the developing countries: first of all China, almost directly followed by India and Russia. The United States occupies the second place in the list. While in 2008–2009, global CO_2 emission dropped by about 2%, China's contribution alone rose by 5% and countries of the Middle East an additional 4%. As compared, the European Union managed to achieve a 7% cut in CO_2 emission that is remarkable.

GREENHOUSE GASES

Referential values of the respective gases are published in the 2008 IEA report (in accordance with the Kyoto Protocol). As seen in *Figure 1*, methane, nitrogen-oxides and fluorous gases considerably contribute to negative climate effects, still, CO_2 is responsible for 80% of the world's emission. Energy-related CO_2 emissions (including from the industrial sector) make approximately 65% of the total amount of GHG gases and make an 80% share in the total CO_2 amount.

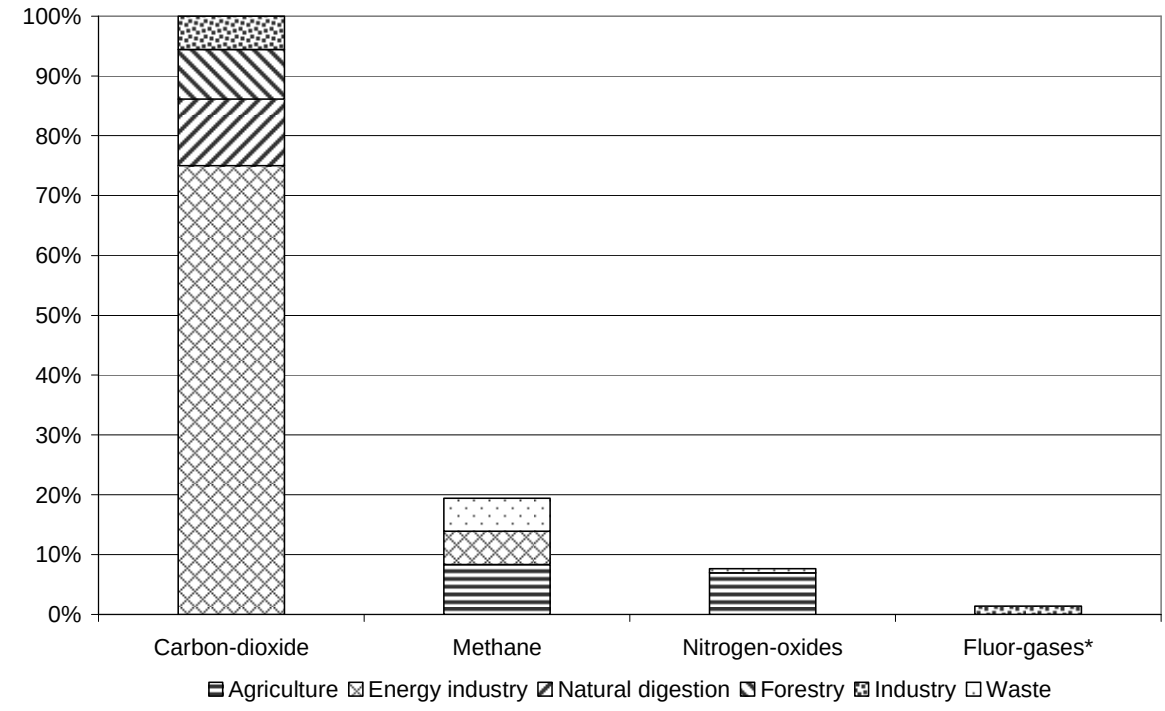

Figure 1.
Shares in the emission of distinctive greenhouse gases (expressed in CO_2 units) by sectors
Source: IEA, World Energy Outlook, 2008

The bulk of CO_2 emission relates to activities of the energy industry, basically electricity and heat generation, as well as transport. Other sources of industrial CO_2 include the utilization of fossil energy resources for non-energy purposes, the direct burning of fuels, and other polluting by-products of applied technological processes. Nitrogen-oxides are emitted into the atmosphere primarily from agricultural and industrial waste. Methane, the second most critical greenhouse gas, is being released mainly from agricultural biomass (landfill degradation) and leftovers of animal husbandry. Industry-related methane emission derives from coal mining, gas leakages and uncontrolled storage conditions. Organic waste also contributes to methane emission. Reducing methane from waste depletion (both agricultural and industrial) is a common preference for environmental protectionists and promoters of energy efficiency. Proper legal regulations are already at hand, applicable technologies being available, implementation now depends on governmental decision-makers and financing.

CO_2 EMISSION OF HUNGARY AND CENTRAL EUROPEAN COUNTRIES

Figure 2 shows CO_2 emission for the EU Member States. Each value is represented against the level of 1990 (taken as base value or 100%). In 2000, some countries happened to overrate the indicatory level however, most Member States achieved substantial reduction over the first decade. The majority of the countries continued steady falling tendencies over the second decade as well. Comparing these lines to that of Hungary, massively declining emission trends can be observed: to 81% by 2000 and to 74% by 2010.

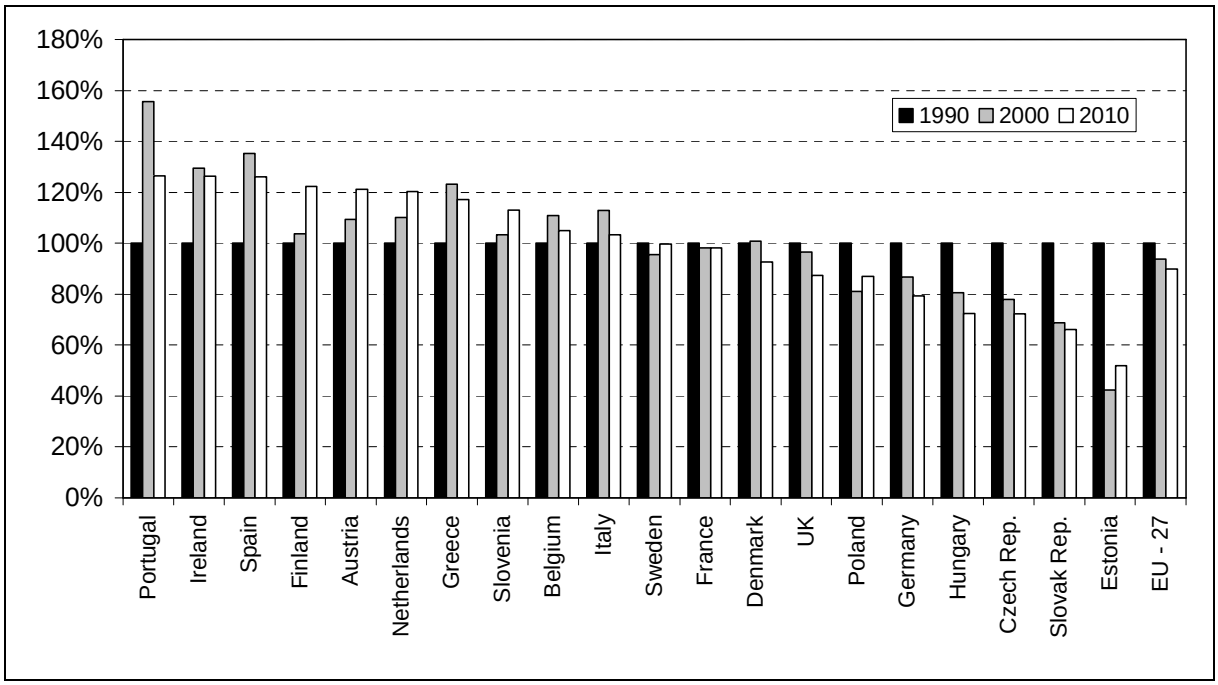

Figure 2.
CO_2 emission trends in EU Member States
Source: IEA, CO_2 Emissions from Fuel Combustion Highlights, OECD/IEA, 2012

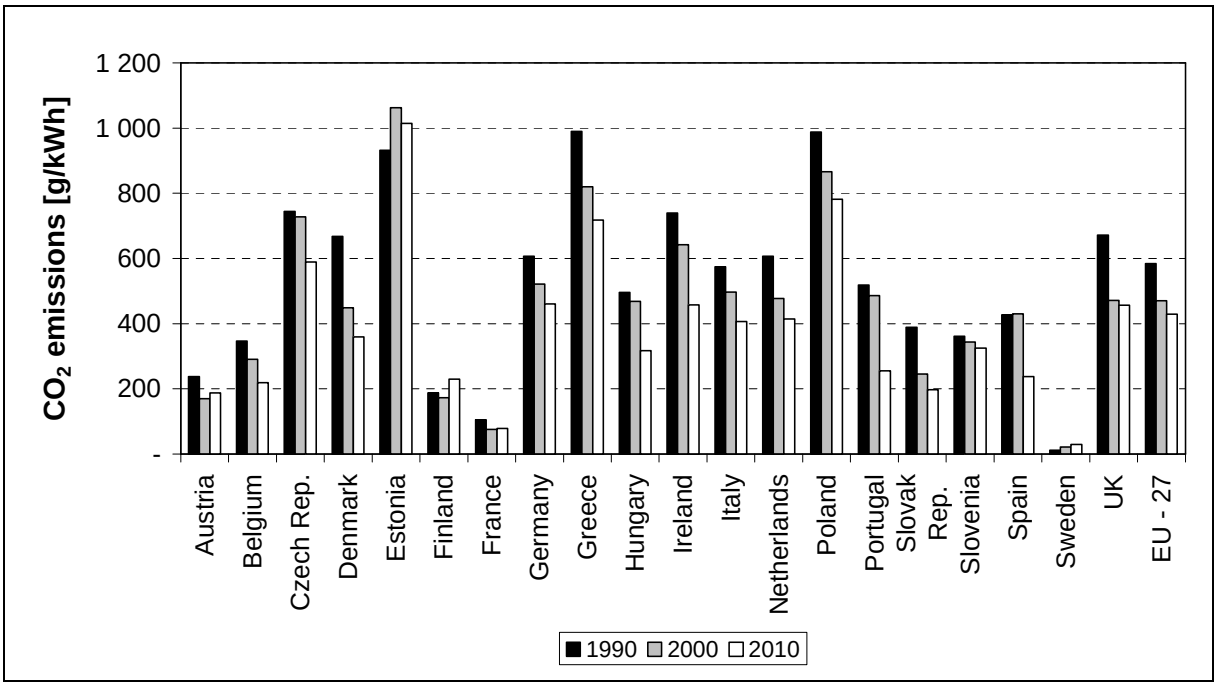

Figure 3.
CO_2 emission from electricity generation
Source: IEA, CO2 Emissions from Fuel Combustion Highlights, OECD/IEA, 2012

Figure 3 represents the CO_2 emission rates of EU states per unit volume of electricity. In this respect, Hungary falls into the OECD EU average. In countries where electricity is mostly supplied from hydroelectric plants or nuclear power stations, the indicators are kept very low. Whereas, in other countries that are heavily dependent on coal-based electricity generation, the indicators are extremely high. The figure also shows that specific CO_2 emission from electricity generation has been reduced in most countries over the past 20 years.

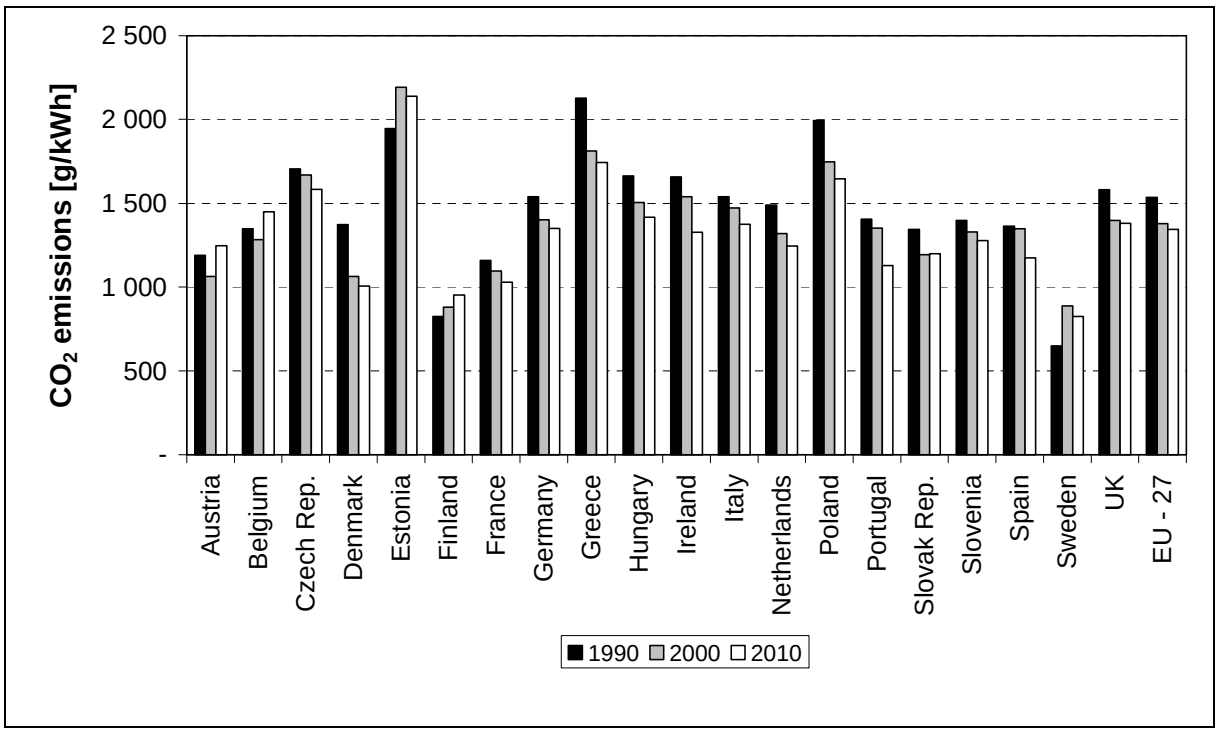

Figure 4.
CO_2 emissions from electricity generation using coal/peat
Source: IEA, CO_2 Emissions from Fuel Combustion Highlights, OECD/IEA, 2012

Considering coal-based fuel plants – as seen in *Figure 4* – no substantial emission reduction is observable over the past 20 years. Indicators mostly exceed 1000 *g/kWh*, in some countries even 2000 *g/kWh*.

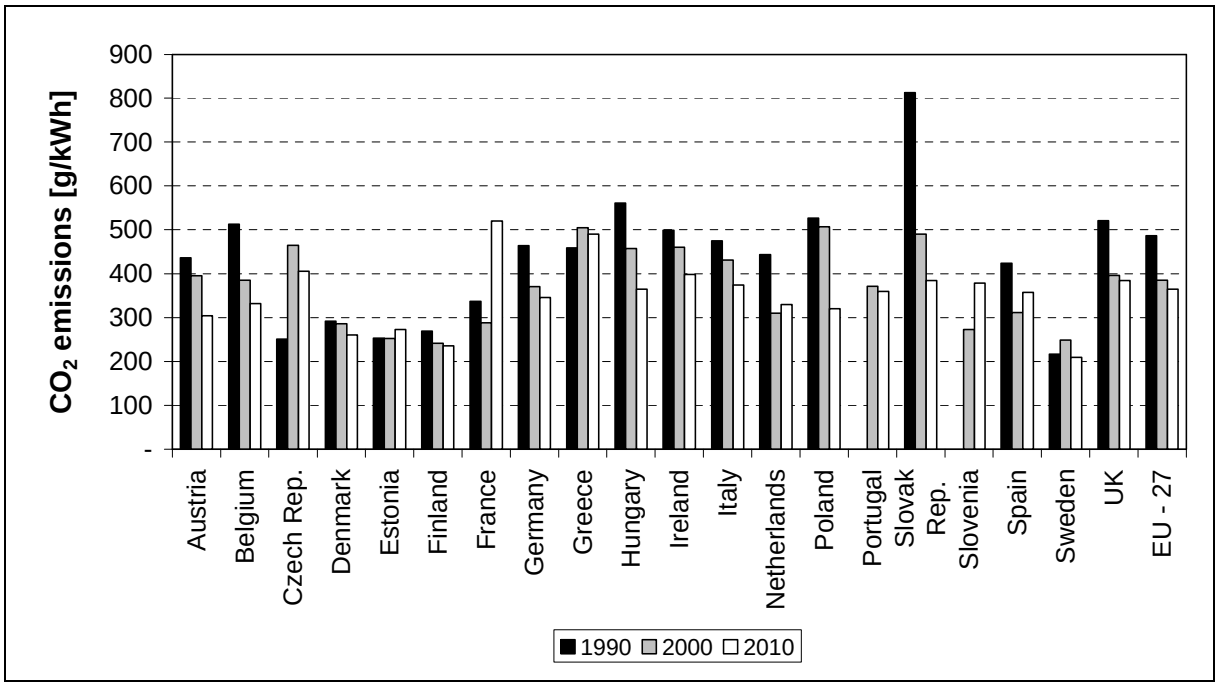

Figure 5.
CO_2 emissions from electricity generation using natural gas
Source: IEA, CO_2 Emissions from Fuel Combustion Highlights, OECD/IEA, 2012

As compared to the above data, specific CO_2 emission rates are a lot more favorable for gas plants. As shown in *Figure 5*, the indicators for most countries stay below 500 *g/kWh*, and a falling tendency is observable.

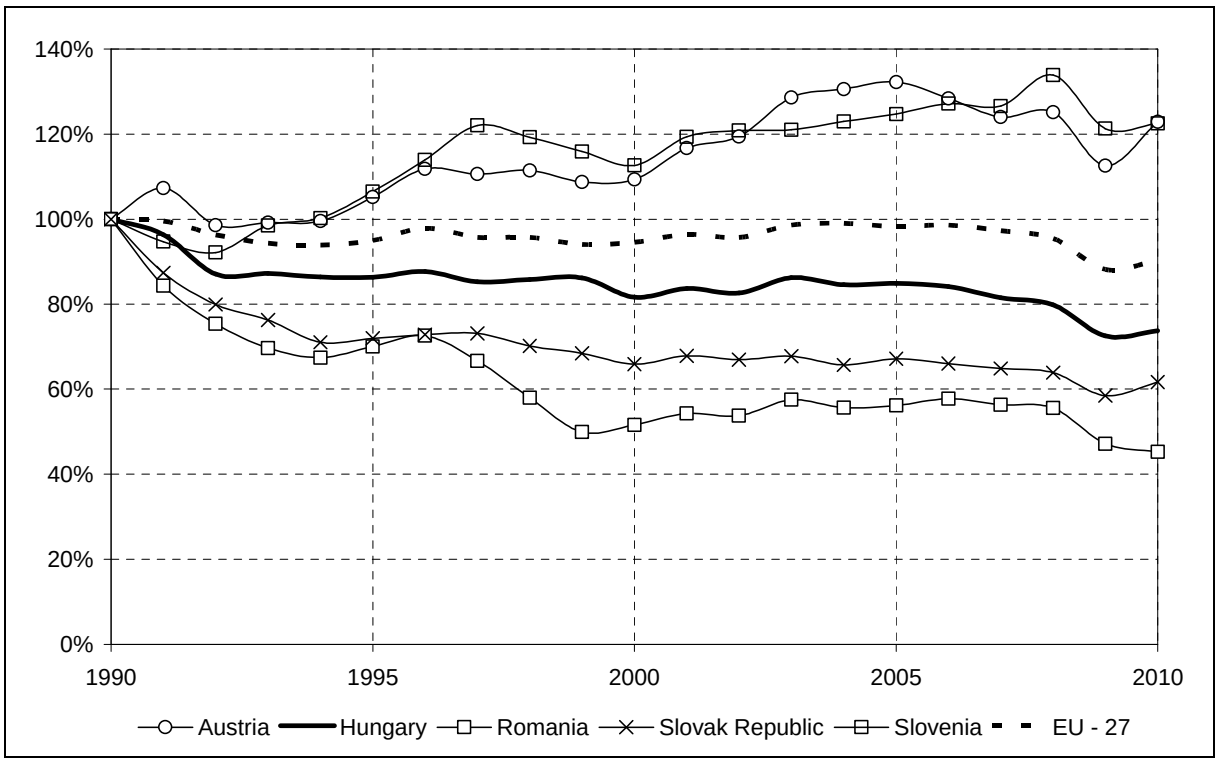

Figure 6.
Trends in CO_2 emission, with reference to the 1990 base level
Source: IEA, CO_2 Emissions from Fuel Combustion Highlights, OECD/IEA, 2012

Figure 6 represents CO_2 emission trends in Hungary and the neighbouring countries between 1990 and 2010. As seen, the EU-27 and Slovenia are showing similar patterns as Hungary, yet, the emission of these two countries notably overrated the level of 1990 between 1995 and 2010. The trends of Hungary and Slovakia are alike in achieving considerable reduction by 2010, in due accordance with the EU-27. Romania is characterized by a peculiar curve, reaching final decline from 2000 on.

To conclude, Hungary seems to have performed remarkably well in achieving substantial CO_2 emission reductions between 1990 and 2010; results forecast, with great certainty, that the country will be able to successfully accomplish the Kyoto target. In the light of historical data, reflecting a leveled precession over the past decades, the Kyoto mandate seems realistic.

On the basis of IEA database (IEA, 2012), *Figure 7* represents Hungary's annual CO_2 emission levels between 1971 and 2010. As clearly seen from the graph, a period of intensive increase up to the early 1980s was followed by a sharp decrease. Around 2000, CO_2 emission levels stayed constant then started falling again.

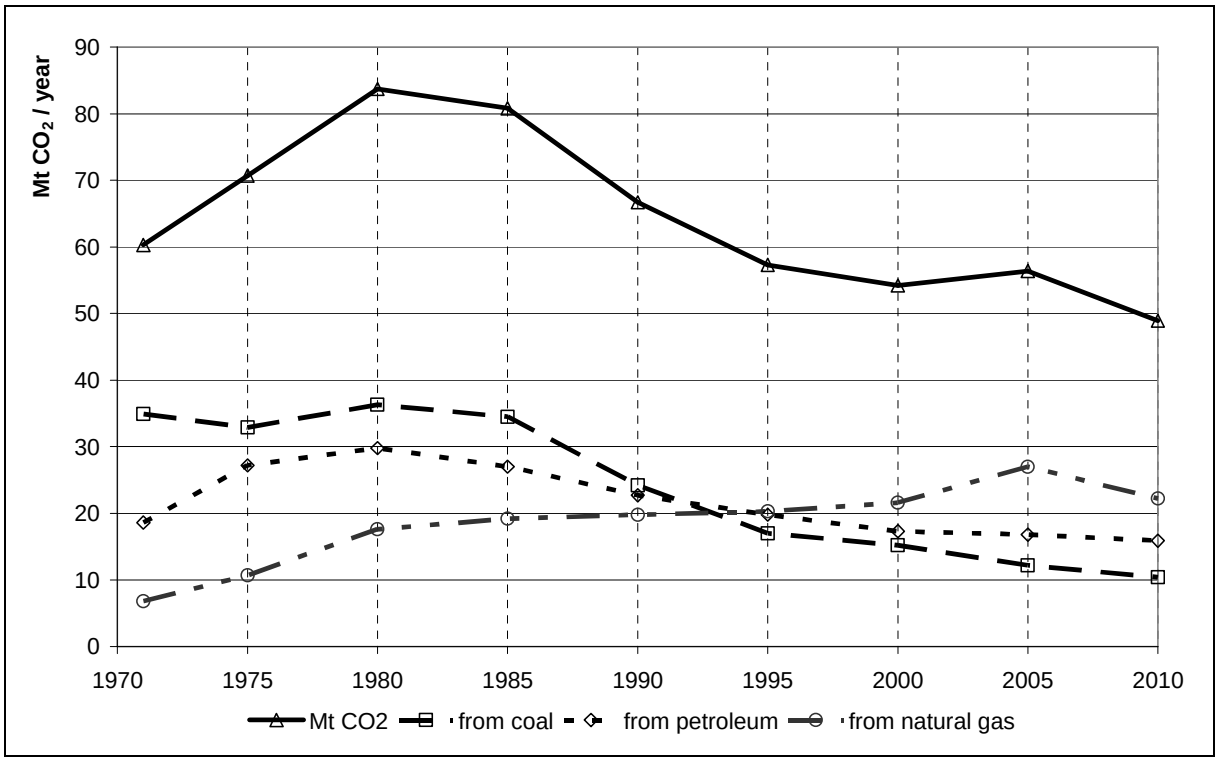

Figure 7.
Hungary's CO_2 emission between 1971 and 2010
Source: IEA, CO_2 Emissions from Fuel Combustion Highlights, OECD/IEA, 2012

As shown, Hungary's CO_2 emission fell drastically in the 1980s. Rather than resulting from conscious energy policy measurements, this trend is basically attributable to heavy setbacks in agricultural and industrial production and to the decline of the formerly operating energy system. Besides radical political changes of the time, Hungary's entire energy infrastructure underwent basic transformations. Solid and fluid fossil fuels were being gradually replaced by natural gas. The dominant role of heavy industry became underplayed by light industry and effective low-carbon technologies were implemented. Developments in the 2000s brought new types of energy demand, leading to increased levels of CO_2 emission once more.

In the context of joint commitment by the Member States to the Kyoto Protocol, Hungary has agreed to achieve a 6% reduction of GHG emissions over the period of 2008–2012, as compared to the base levels of 1985–87. In the past two decades, Hungarian economy and industry underwent fundamental structural transformations leading into a more efficient and competitive low-carbon energy system. As a result, the country's CO_2 emission stayed 43% below the Kyoto base level in 2009, even allowing for extended facilities of emission allowance trading.

AIMS AND EFFORTS IN HUNGARY

The First Paragraph of Parliamentary Order No. 77/2011 (X. 14) declares the requirement of restructuring the entire energy system unavoidable, entangling an increased share of renewable resources in electricity generation, the implementation of new, innovative technologies, heating capacity extension using alternative fuels or green power, the deployment of biofuel vehicles and other low-carbon means of transport. However, as clearly reflected in the document, the current high share of natural gas in the energy market is not expected to be replaced by competitive alternatives, nor other fossil fuels are likely to become eliminable from the energy mix. Thus, there is little chance of experiencing rapid and unprecedented drop in CO_2 emission. Hungary has great potentials to capture and store CO_2 originating from combined heat and power plants, which can largely contribute to realizing the Kyoto targets and making low-carbon energy structure a feasible option.

Further initiatives are set to lower primary energy consumption from 1085 *peta joule [PJ]* (2010 level) by 2030, but not in the worst case exceed 1150 *PJ*. 6–9% of primary energy might be saved from refurbishing obsolete, inefficient fuel-fired power plants, with the additional result of reducing CO_2 emission from today's level of 370 gCO_2/kWh to around 200 gCO_2/kWh. Modernization processes in the energy sector should be delivered in a way to facilitate a higher penetration of renewable energy. The national energy mix is still likely to include nuclear power, with respect to the contribution of Paks reactor, where new atomic blocks are going to be installed. This capacity extension will lead to successful decarbonisation in the middle-term (up to 2030). However, the planned closure of the currently operating four blocks of the nuclear plant following 2032–2037, is likely to result in substantial supply shortages, which will have to be provided from alternative low-carbon sources. A possible scenario to compensate for capacity losses is the establishment of new, fossil-based energy utilities, like gas combustion plants or coal-fired thermal power blocks. Due to subsequent environmental effects, this option is only acceptable if supplemented with mature CCS technologies. In an opposite case, that solution would lead to drastic increase in CO_2 emission, making extra CO_2 emission quotes necessary for Hungary.

The decarbonisation of the energy industry is the most crucial driving factor in the European Committee's Energy Roadmap 2050. Due to present knowledge, this objective only seems feasible with a substantially increased share of renewable energy sources and retain of nuclear energy in the overall energy mix, amended with the wide-scale commercialization of CCS technologies. Considering the decarbonisation principle, CCS will play an essential role in coal-based electricity generation and related industrial fields within the Community. The European Parliament and of the Council extended the scope of emission trade regulations to CCS technologies from 2013. Economic viability of applying CCS technologies basically depends on the market pricing of CO_2. Meanwhile, the European Commission, in its Directive 2009/31/EC on the geological storage of carbon dioxide laid down all the principles for regulating carbon capture and storage processes, from site selection to monitoring and environmental control.

In the national scale, the legislative framework has been established by the Hungarian Parliament via 2010 modification of Article No. XLVIII of 1993 (see Article No. XL of 2010). Subsequently, any kind of exploration, fitting-for-purpose operation, maintenance and closing up of underground geological formations applicable for industrial or energy-related CO_2 storage fall under the effect of Mining Law. Paragraph 22/C of the respective Article lays down the rules for exploiting geological structures applicable for storing large volumes of CO_2 from the energy industry, and provides explicate regulations for storing and handling large volumes of CO_2 in such underground formations. Reporting on the capacity assessment of industrial or geological formations in Hungary potentially applicable for underground CO_2 storage were required to be accomplished by responsible governmental authorities by 31 Dec 2011.

CCS-related storage capacity demands are estimated to amount to about 150 million tonnes by 2018 (Kubus, 2009). In theory, available storage capacities in Hungary are assessed to be orders of magnitude larger, about 26 billion tonnes (see data included in the pertinent Parliamentary Order). The bulk of this volume (cca. 25 billion tonnes) would be covered by deep saline aquifers (located min. 1000 *m* below sea level), supposing that proper geological and safety management information will have been obtained by the time actual operations would start. Underground carbon layers/seams are likely to store about 717 million tonnes CO_2, whereas, depleted hydrocarbon fields might retain as much as 469 million tonnes, in theory.

In 2007, Hungarian power plants emitted cca. 18 million tonnes of CO_2. According to MAVIR data, this amount is expected to abate to 14 million tonnes by 2025. Taking the mean average (16 million tonnes) and dividing it with the potential storage capacity demands assessed up till 2018, it becomes clear, that currently explored underground storage formations seem unable to keep up with CCS needs in the long run (more than 9 years).

CONCLUSIONS

The analysis of CO_2 emission trends in Hungary over the past four decades allow a comparison of historical results with proactive governmental measurements and strategy incentives (included in the National Energy Strategy 2030) to achieve emission reduction by 2020–2030. Conclusions can be summarized as follows:

- The performance of Hungary to achieve substantial reduction in CO_2 emission between 1990 and 2010 is remarkable, and it forecasts, with great certainty, a successful accomplishment of the Kyoto target. In the light of the data, reflecting leveled precession over the decades, the Kyoto mandate seems realistic. Hungary's results are promising and mark the road to pursue in the deployment of energy strategy plans up to 2020.
- Reducing CO_2 emission within the power sector is cost-demanding. Investments are not only required to modernize existing power production, but also to optimally integrate renewable energies and resources into electricity generation. No EU-conform emission reduction targets seems realizable without installing new nuclear power blocks. Since fossil fuels are likely to retain their leading role in the diversified energy supply portfolio, the application of new CCS technologies will be an imperative.
- The high renewable energy resources scenario seems insufficient to deliver substantial emission cuts. Assuming that global climate policies prescribe emission reduction up to 90–95% in the power sector, fossil-fired plants will have to be supplemented with mature and reliable CCS technologies. Most of these projects are still in the innovation phase and need further development to become cost-efficient.

- Hungary has promising facilities to implement CCS technologies: with proper eligibility measures taken, assessed storage capacities in depleted hydrocarbon fields will be enough to retain the current rate of annual CO_2 emission from the power sector over a 9 year term. Yet, safety requirements, providing secure and sustainable storage conditions for centuries are still a critical issue.

The two paramount issues for making CCS technologies economically attractive for investors and market participants in Hungary are: competitive carbon-dioxide prices and scientifically proven evidence that deep underground saline aquifers will be applicable to securely store CO_2 for centuries.

ACKNOWLEDGEMENT

This work was carried out as part of the TÁMOP-4.2.1.B-10/2/KONV-2010-0001 project in the framework of the New Hungarian Development Plan. The realization of this project was supported by the European Union and, co-financed by the European Social Fund.

ABBREVIATIONS

CCS: Carbon Capture and Storage
GHG: greenhouse gases
MAVIR: Hungarian Independent Transmission Operator Company Ltd., MAVIR ZRt.
OECD: Organisation for Economic Co-operation and Development

REFERENCES

1. 77/2011. (X. 14.) OGY határozat a Nemzeti Energiastratégiáról (Parliamentary Act on National *Energy Strategy, 77/2011. [X.14.] OGY)*
2. International Energy Agency: *CO_2 emissions from fuel combustion*, Highlights, IEA Statistics, 2011 Edition, ISBN 978-92-64-102835
3. International Energy Agency: *Energy Sector Methane Recovery and Use*, The Importance of Policy; OECD/IEA, 2009.
4. International Energy Agency: *CO_2 Emissions from Fuel Combustion Highlights*, OECD/IEA, 2012
5. Kubus, P.: A CCS-projekt realitása a hazai olajipar szempontjából *(The feasibility of a CCS-project from the perspective of domestic oil industry)*; Magyar Tudomány *(Hungarian Science)*, 2011/4. pp. 459–464.
6. Kubus, P.: *CO_2 storage possibilities in Hungary;* MOL Scientific Magazine, SD & HSE special issue, 2009.
7. Nemzeti Fejlesztési Minisztérium: Magyarország megújuló energia hasznosítási cselekvési terve, 2010–2020, A 2020-ig terjedő megújuló energiahordozó felhasználás alakulásáról (2010. december) *(Ministry of National Development: Hungary's Renewable Energy Action Plan for 2010–2020) (12. 2010)*

Geosciences and Engineering, Vol. 2, No. 3 (2013), pp. 19–24.

THE ESTIMATION OF NATURAL GROUNDWATER RECHARGE ON THE EXAMPLE OF TWO RESEARCH SITES ON THE DANUBE-TISZA INTERFLUVES

LÁSZLÓ KOMPÁR[1]–ENDRE DOBOS[2]–PÉTER SZŰCS[3]
[1, 3] MTA-ME Research Group of Geoengineering,
Department of Hydrogeology and Engineering Geology, University of Miskolc
[2] Department of Geography and Ecology, University of Miskolc

ABSTRACT

The Danube-Tisza Interfluves is one of the largest recharge areas in Europe. We selected two research sites in Hungary to investigate the natural groundwater recharge. These sites are located at Méntelek and Kecskemét. The previous measurements were based on the isotope hydrology and the transport modeling. Generally, the tritium is formed in the upper atmosphere during –β decay. It has a half time, during the tritium decays to ^{3}He, which is 12.4 years in this case. From the 1950s the high-altitude nuclear tests introduced large amounts of tritium into the atmosphere. Because the relatively short half-time of the tritium we can receive some information from the last 50 years happening. MODFLOW is a U.S. Geological Survey modular finite-difference flow model. This computer code can solve the groundwater flow equation. In addition to the numerical simulations, in this paper we show the results our pedological investigations on the test sites to clarify the result of the recharge models.

INTRODUCTION

The importance of the quantity and quality of the drinking water resources for the inhabitants on the Earth is significantly increased. Different quality and quantity of water is necessary for the residential, agricultural and industrial usage of the water. The simulations, lab tests and the field measurements are increasingly important for the hydrogeologist for the hydraulic researches (Szűcs et al. 2009).There were some transport calculations for different test sites near Méntelek and Kecskemét with the Processing MODFLOW Pro software package in the previous researches dealing with groundwater flow systems. The aim of those studies was to clarify the recharge rate on the Danube-Tisza Interfluves. During the isotope hydrogeological researches an average groundwater level was assumed around the tests sites (Kompár et al. 2012).

The task of this paper to obtain confirmation for our axiom; could we calculate a unified groundwater level on the Danube-Tisza Interfluves, or we must to considered some different groundwater levels on the above mentioned areas. The investigation of the natural recharge is a very important task for the groundwater management purposes in hydrogeological researches. The rate of the recharge from the precipitation is basically determined by the amount and intensity of the rainfall. The evapotranspiration is determined by the vegetation of the soil surface, which has also a big effect for the infiltration processes. The physical properties of the soils play a key role under hydraulic conditions; the permeability of the soil show, how fast the infiltrated water can flow in the soil (Szűcs et al. 2011; Szűcs 2012). The average occurrence level of the groundwater can be determined by the depth of gleyic properties occurring in the soil profile. Dobos et al. (2012) developed several GIS and digital terrain model based approaches to define the likehood of the occurrence of these properties in the soils. The results of the previous researches show that nearly vertical movement was assumed for the groundwater. The wells near Méntelek and Kecskemét were installed between the Danube and the Tisza rivers. There is no effect of these rivers for the

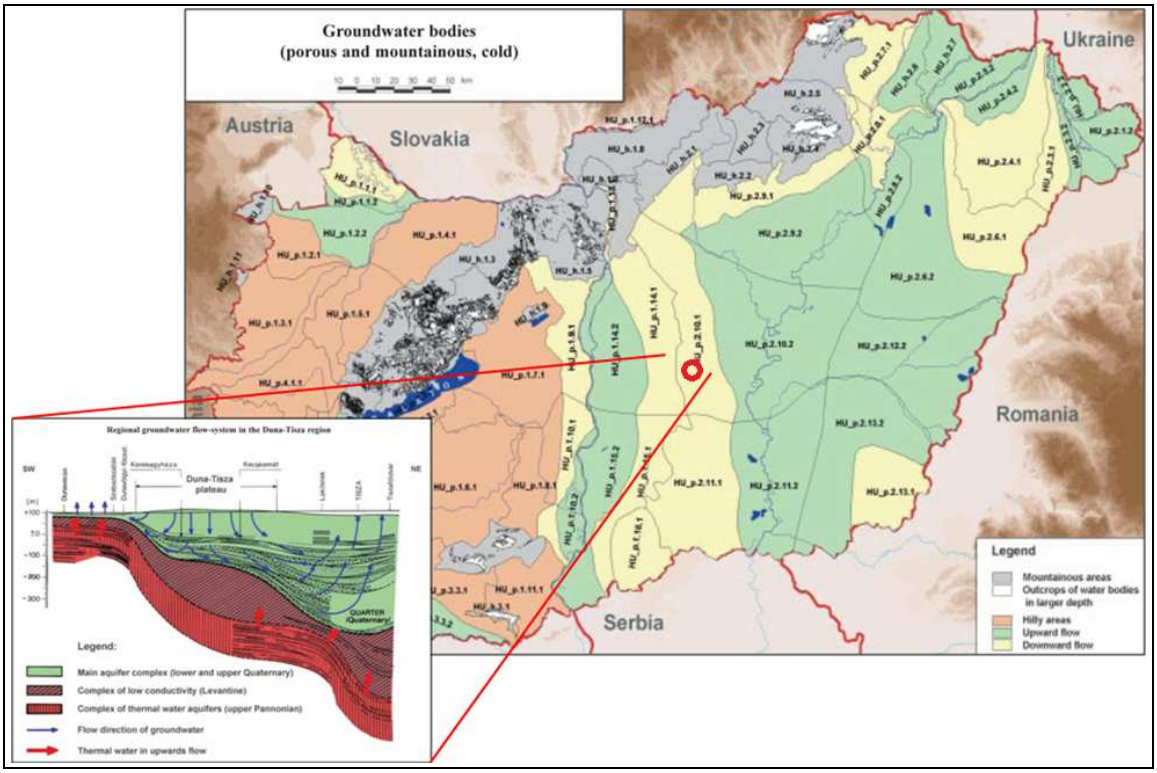

Figure 1. Regional recharge area on the Danube-Tisza Interfluves

groundwater level on the research sites, because of the large distance. The Danube-Tisza Interfluves is one of the largest recharge areas in Hungary, and also in the Carpathian Basin (*Figure 1*). We had to know accurately the geological parameters and the soil properties to understand the flow conditions operated partly by groundwater replenishment.

DESCRIPTION OF THE TEST SITES

The Danube-Tisza Interfluves is a part of the 3rd geochemical landscape of Hungary, which expands from Komárom to Szeged, wherein the cations especially Ca, Mg and Sr; the anions are mainly sulphates and carbonates. The shape of the location of this landscape reliably linked to the manly north-west and north wind. The ridge built up from sand, but the loess is also determinative. There is an important thing that the lime is highly accumulated in the soil in this region.

This lime accumulation has some specialities in this region. The carbonates dissolved from the sediments, which cover the surface. In this region there is a research work, which demonstrates that the carbonates are dissolved from the sediments, but not originates peel of the rock.

The sand is the bedrock in the region, which originates from the alluvium of the Danube. There are some ideas for the presence of the sand. Some researcher note about the differences between the Danube and the Tisza; while some carbonate particle were found in the Danube, these particles are completely missing in case of the Tisza (Várallyai 1967).

We know from some studies, that the carbonate minerals have been transported with the wind from the Transdanubian Mountains mostly mixed with loess. There are two mean reasons of the lime accumulation; firstly originates from the capillary water, on the other hand from the bottom of the lakes. (Ujházi 2003)

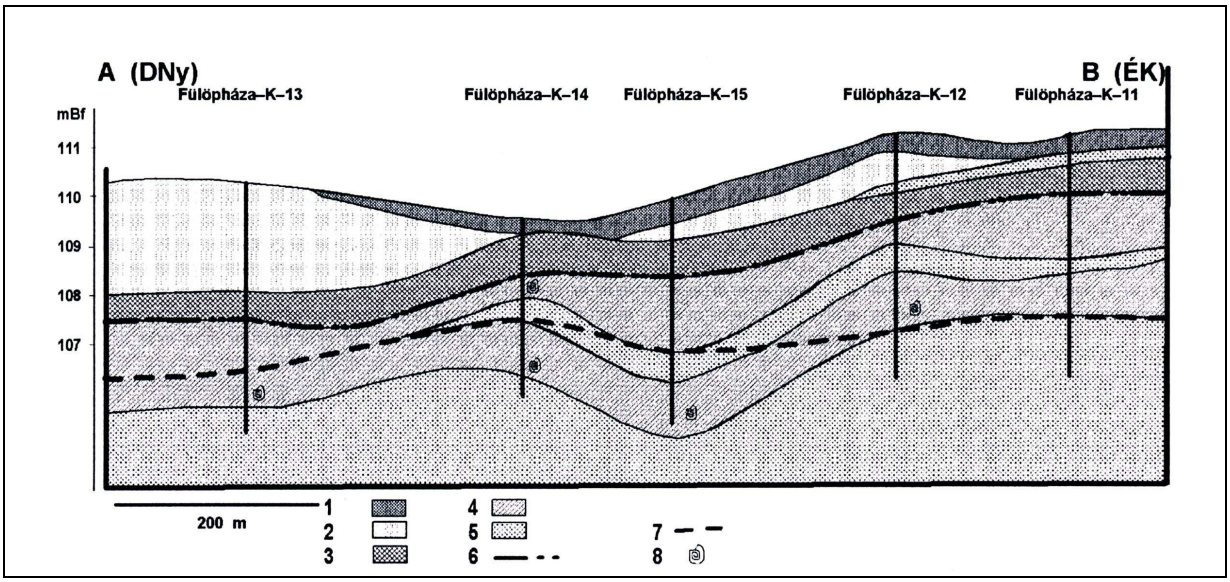

Figure 2. The shallow sediments of the 1st cross-section (Fügedi et al. 2008)
Legend: 1. recent soil sand; 2. sand; 3. paleosol; 4. sandy silt; 5. silty sand;
6. level of the lime accumulation; 7. groundwater level; 8. snail residues

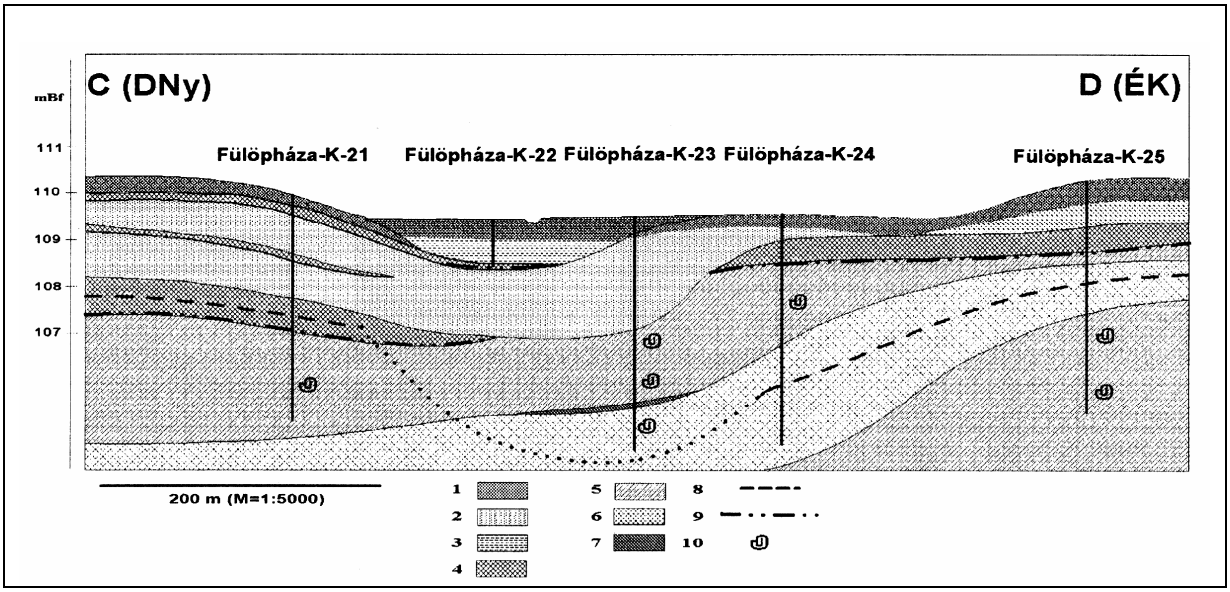

Figure 3. The shallow sediments of the 2nd cross-section (Fügedi et al. 2008)
Legend: 1. recent soil; 2. sand; 3. lime mud; 4. paleosol; 5. sandy silt;
6. silty sand; 7. organic sludge; 8. level of the lime accumulation; 9. groundwater level;
10. snail residues

The abstract CO_2 by the plants may be the first reason of these lime accumulations, and the Ca and Mg ions have high concentration value during the drying of the lakes.

These processes determine the chemical composition of the lime mud. Fügedi et el. (2008) wrote about the geochemical characteristics of the lime accumulation near Fülöpháza in their studies. They explored two cross-sections, which show the geological, hydrogeological parameters and the levels of the lime accumulations. (*Figure 2–3*) It was found that the aeolian sediment flow is one of the reasons of the horizontal differences; furthermore the ionic migrations may also occur. (Fügedi et al. 2008)

RESULTS AND DISCUSSIONS

We explored two soil profiles on the Danube-Tisza Interfluve in December 2012 (*Figure 4–5*). The soil profile by the Figure 3 locates in Méntelek, which place is periodically covered by water. This profile is characterized by calcareous, shallow humous layer and humous sandy layer, according to the Hungarian classification (WRB: Endogleyic CALCISOL

Figure 4.
The profile of the humous sandy soil in Méntelek
(December 2012)

Figure 5.
The profile of the lime coated chernozem soil in Kecskemét
(December 2012)

(Arenic)). *Figure 4* shows the profile of the test site in Kecskemét; this site is loamy sand with medium growing layer, and typical chernozem soil (WRB: Calcic CHERNOZEM (Pachic)).

Our goals with the two profiles were to explore soil parameters, which characterize groundwater and infiltration conditions of the sites. In this aspect the important physical characteristic of the soil is the gleyization and its features, furthermore the lime accumulation levels in the capillary zone. We could not reach the groundwater level at the investigated two sites despite the fact that the profile of Méntelek further we drilled from the bottom of the trench to 4 meters.

The soil profile of Méntelek indicates periodically high water table in the area. This fact comes from the geomorphology position and the recognizable features of the profile. The vegetation contains sandy grassland and the planted pine forest. It is clearly visible the dual-carbonate accumulation level from 0 to 0.33 m and under 0.55 m. Furthermore, the characteristics of the water flow influences show gleyization level in the upper 0.20 m and the thickness from 0.30 m to 0.55 m. There is a significant difference in the genetic parameters between the two lime accumulation levels. The reason of the formation of the whitening level is the CO_2 in the A-horizon. During the lime continuously spread to lower layers the CO_2 concentration is decreasing and the solubility of the lime is also decreasing form the lime accumulation level. These processes indicate that the pore volume of the soil

decreases, so the movement of the water by the infiltration becomes slower. Under 0.50 m the large quantity of the lime originates from the capillary zone. This amount of the lime is blocks the infiltrating processes; the water stagnates and reductive conditions can be created. This state is temporary, which indicates by the reddish trivalent iron, but in the deeper layers these situations become permanent. The gleyizated and lime accumulated layers clearly indicates that the infiltration slow down in two different depths, furthermore the lower lime accumulation level becomes quasi-sealing.

The soil profile is very different in case of Kecskemét. There is loess sand on the surface with higher starting calcium content than the lower sandy layers, furthermore comparable lime accumulations is missing. During the wet spring weather the found lime dissolves and leaches, in summer also accumulates by the evaporation. Permanent and intermittent water exposure could not be identified. This test site located on the top of the ridge, so we could investigate just near vertical flow. This explains the fundamental difference between the two profiles in the lime accumulation. (Fügedy et al. 2008)

CONCLUSIONS

The aim of this study was to characterize the water balance and the groundwater dynamic terms with the help of the pedological investigations. We explored two different sites near Méntelek and Kecskemét on the Danube-Tisza Interfluves. Our conclusions are necessary to calculate the vertical and also the horizontal groundwater flow at the test sites. There is a significant lateral groundwater flow to the deeper level, which is indicated by the lime accumulations. We found that the vertical groundwater flow values are not the same inside one profile. If the lime accumulations levels slope, the groundwater can flow in lateral direction. These facts are very important during the hydrodynamical tests and the groundwater modeling. As a result, the flow and transport models of the investigated sites will be modified based on the described results. It is nearly sure that the calibration parameters of the numerical models will be improved, which can guarantee more accurate recharge estimation.

ACKNOWLEDGMENT

The described work was carried out as part of the TÁMOP -4.2.1.B-10/2/KONV-2010-0008 project in the framework of the New Hungarian Development Plan. The realization of this project is supported by the European Union, co-financed by the European Social Fund.

REFERENCES

1. Dobos, E.–Vadnai, P.–Láng, V.–Fuchs, M.–Micheli, E.–Seres, A.: *"A novel approach for soil mapping of WRB units."* Eurosoil 2012. Bari, Italy. S04-02-P-9. July 2–6, 2012.
2. Dobos E.–Vadnai P.: *„A glejes talajrétegek megjelenésének becslése térinformatikai módszerekkel."* VIII. Kárpát-medencei környezettudományi konferencia, április 18–21., 2012. Veszprém.
3. Dobos E.–Vadnai P.: *„Ideális interpolációs módszer keresése a talajvízszint ingadozás talajfejlődésre gyakorolt hatásának térinformatikai vizsgálatához."* XIV. Bányászati, Kohászati és Földtani Konferencia. Erdélyi Magyar Műszaki Tudományos Társaság. Arad. március 29.–április 1., 2012.
4. Fügedi U.–Pocsai T.–Kuti L.–Horváth I.–Vatai J.: *„A mészfelhalmozódás földtani okai Közép-Magyarország talajaiban."* Agrokémia és talajtan. Budapest, 2008. 57/2. pp. 239–260.
5. Kompár, L.–Szűcs, P.–Palcsu, L.–Deák, J.: *"Determination of natural groundwater recharge with the help of groundwater modeling and tritium field measurements."* Geosciences and engineering: A publication of the University of Miskolc, 1:(1) pp. 2012, 159–165.

6. Szűcs, P.–Madarász, T.–F, Civan.: *"Remediating Over-Produced and Contaminated Aquifers by Artificial Recharge from Surface Waters."* Springer Science, Environ Model Assess, 2009, 14. pp. 511–520.
7. Szűcs P.–Székely F.: *„Kihívások és lehetőségek a hazai ásvány-, gyógy- és hévízkészletek feltárásában és hasznosításában."* A Miskolci Egyetem Közleménye, A sorozat, Bányászat, 81. kötet, VIII. Kárpát-medence Ásvány- és Gyógyvizei Konferencia, „Termálvíz-Borvíz-Egészség", HU ISSN 1417-5398, Miskolci Egyetemi Kiadó, 2011, pp. 51–58.
8. Szűcs P.: *„Hidrogeológia a Kárpát-medencében – hogyan tovább?"* Magyar Tudomány, 2012, 5. HU ISSN 0025 0325, pp. 554–565.
9. Ujházi, K.–Gábris, GY.–Frechen, M.: *"Ages of periods of sand movement in Hungary determined through luminescence measurements."* Quaternary International. 2003, 111. pp. 91–100.
10. Várallyai GY.: *„A dunavölgyi talajok sófelhalmozódási folyamatai."* Agrokémia és Talajtan. 16. 1967, pp. 327–356.

Geosciences and Engineering, Vol. 2, No. 3 (2103), pp. 25–36.

DETAILED DESIGN OF AN ESP INSTALLATION FOR A GEOTHERMAL WELL

GÁBOR TAKÁCS
Petroleum Engineering Department
University of Miskolc
gtakacs@kfgi.uni-miskolc.hu

ABSTRACT

Electrical submersible pump installations are the prime candidates for application in water producing and/or geothermal wells because of the many beneficial features of this artificial lift method long used in the oil field. ESP units are ideally suited to produce large and extremely large volumes of liquids from wells and the very efficient cooling of the ESP motor provided by water flow permits a long operating life.

The paper introduces the basic design of an ESP installation for geothermal water production and details the selection and application of the system's different components. Being the heart of the system, the selection of the submersible pump provides the basis for the design of the total system. Pump type, the necessary number of stages are properly selected and checked for operating conditions. After the required electric motor is selected, the cable selection is one of the important steps which involves not only technical but economic considerations as well. The design procedure detailed in the paper can directly be used in selecting and operating ESP systems utilized for geothermal well production.

1. INTRODUCTION

In case of application in geothermal wells operating conditions are ideal for ESP units because of the following features:

- The well usually produces single-phase liquid, water only.
- The amount of free gas at the pump suction, if any, is very low so that it can be removed easily by a simple reverse-flow gas separator. Therefore, no deterioration of submersible pump performance takes place.
- The viscosity of the produced water is low, so that no correction of the standard pump performance curves is necessary.
- The ESP unit is fed with an AC current with a constant frequency.

Such flow conditions are ideal for the operation of the centrifugal pump and allow the application of a very straightforward design procedure [1–6] the main phases of which are detailed in the following sections.

2. DATA REQUIREMENTS

For a proper design of the ESP installation, the knowledge of many different data is necessary. Perhaps the most important among them is the reliable information on the well's productivity so that the desired liquid rate from the well can be established. The liquid rate is always an input parameter in the design of ESP installations because the selection of the submersible pump (the heart of the system) can only be accomplished in the knowledge of the desired rate. Just remember that different pumps have different recommended application ranges.

Necessary input data can be grouped as given here.

1. **Well Physical Data.**
   - Casing and liner sizes, weights, and setting depths.
   - Tubing size, type, weight, and thread.
   - Total well depth.
   - Depth of perforations or open hole interval.
   - Well inclination data.
2. **Well Performance Data.**
   - Tubinghead pressure at the desired rate.
   - Casinghead pressure.
   - Desired liquid production rate.
   - Static bottomhole pressure or static liquid level.
   - Flowing bottomhole pressure or dynamic liquid level.
   - Productivity data.
   - Producing gas-water ratio.
   - Bottomhole temperature at desired water rate.
3. **Fluid Properties.**
   - Specific gravity of water.
   - Specific gravity of produced gas.
   - Bubble point pressure.
4. **Surface Power Supply Parameters.**
   - Primary voltage available at the wellsite.
   - Frequency of the power supply.
   - Available power supply capacity.
5. **Unusual Operating Conditions.**
   - Production of abrasives, especially sand.
   - Type and severity of corrosion.
   - Extremely high well temperatures.

3. WELL INFLOW CALCULATIONS

The basic requirement for a proper installation design is the exact information on the well's inflow performance because the selection of the ESP pump cannot be made without the knowledge of the liquid rate and the corresponding dynamic liquid level. These parameters are interrelated and can be calculated from the well's Inflow Performance Curve and usually the constant Productivity Index (*PI*) model is applied, depending on whether free gas is present at the perforations or not.

The well's flowing bottomhole pressure (*FBHP*) is easily calculated from the previous data and the next formula has to be used if the constant PI equation describes the well inflow:

$$\boldsymbol{FBHP = SBHP - \frac{q}{PI}} \tag{1}$$

Based on the flowing bottomhole pressure (*FBHP*) at the perforations the pressure at the pump's **suction** (Pump Intake Pressure, *PIP*) is found from the following formula, using the fluid gradient valid in the annulus below the pump setting depth:

$$\boldsymbol{PIP = FBHP - \left(L_{perf} - L_{set}\right) grad_l} \tag{2}$$

Finally, the "in-situ" **liquid volumetric rate** to be handled by the ESP pump is found from the water flow rate:

$$q_l' = q_w \, B_w \tag{3}$$

In addition to these calculations and based on the actual inflow performance data the well's maximum possible flow rate can also be established. This enables one to investigate the possibility of other producing scenarios.

4. TDH CALCULATIONS

In order to determine the required number of pump stages in a later phase of the design procedure, the total head to be overcome by the ESP pump has to be determined. This is called the Total Dynamic Head, *TDH*, and is the sum of the following components, all expressed in length units:

- the wellhead pressure at the given liquid production rate,
- the net hydrostatic pressure acting on the pump, and
- the frictional pressure drop that occurs in the tubing string at the given liquid rate.

The second term equals the true vertical depth (TVD) of the dynamic liquid level, the depth where the water level in the casing annulus stabilizes while producing the desired liquid rate. It is easily found from the value of the pump intake pressure, *PIP*, as given here:

$$L_{dyn} = \frac{L_{set} \; grad_w + CHP - PIP}{grad_w - grad_g} \tag{4}$$

It should be noted here that the pump is usually set below this depth in order to provide the necessary submergence required for proper pump operation. A rule of thumb value is at least 500 ft of fluid over the pump (FOP), the other limit being the depth of the sandface (perforations). The reason is that in conventional installations the motor must be set above the depth of the sandface to ensure the liquid velocity required for proper cooling.

The frictional head loss in the tubing string, Δh_{fr}, can be estimated from charts or the widely used Hazen–Williams formula can be employed.

The total frictional head loss in the tubing string is found as:

$$\Delta H_{fr} = \Delta h_{fr} \, \frac{L_t}{1{,}000} \tag{5}$$

If not done before the start of the installation design, the size of the existing or predicted tubing string should be checked for extensive frictional pressure drop. The generally accepted practice in the ESP industry is to limit the frictional head loss in the tubing string to a value of 100 ft / 1,000 ft. When the head loss found at the desired water production rate is greater than this value, selection of a bigger tubing size is recommended. If this rule is followed, the frictional energy loss in the tubing string consumes less than 10% of the total energy requirement of the ESP system [7, 8], and this ensures an economic installation design.

Now, the *TDH* is calculated in head (ft) units as follows:

$$TDH = \frac{2.31}{\gamma_l} WHP + L_{dyn} + \Delta H_{fr} \tag{6}$$

5. SELECTION OF THE PUMP

The selection of the proper ESP pump for operating in a given well involves:

- the determination of the pump series (outside diameter) to be used,
- the selection of the required pump type,
- the calculation of the required number of stages, as well as
- the checking of the mechanical strength of the selected pump.

5.1. Pump Series

As with all ESP components, the most important selection criteria is that the chosen pump should fit in the casing string of the well. Centrifugal pumps are manufactured in different outside diameters, their series numbers usually represent their outside diameters, e.g. a 338 Series pump's OD is 3.38 in, 400 Series means 4.00 in OD, etc.

When selecting the pump series to be used, economic considerations command the choice of pumps with the largest OD that can be run in the given casing size. This is because ESP components (pumps, motors, etc.) with identical technical parameters but different ODs, due to manufacturing complications, are less expensive if they have a larger OD.

5.2. Pump Type

After the pump series has been determined, the proper type is selected from the available options. Pump types differ in the design of the stages such as the shape and number of vanes, the height, angle, and length of vanes, etc. All these factors have an impact on the liquid flow rate and the head developed by a pump stage.

Pump type selection is based on the comparison of the well's desired water production rate and the recommended liquid capacity ranges of the pump types available. The ESP pump type selected should have

- the required water rate within its optimum capacity range, and
- the rate belonging to its best efficiency point (BEP) to fall close to the desired rate.

If several pump types meet these requirements the final selection may be based on the following considerations.

- Compare the horsepower requirements and choose the pump that needs a smaller motor.
- If the accuracy of the well's inflow parameters is unreliable, choose a pump with a "steep" Q–H (head capacity) curve. Such pumps will produce a water rate near the desired volume even if the actual *TDH* differs from the design rate.

5.3. Number of Stages

The individual stages in a multistage centrifugal pump develop identical heads which are additive so a pump with a given number of stages develops a total head equal to the sum of the heads of all stages. This allows the determination of the necessary number of stages for a given case where the total head represented by the *TDH* is known.

Since at this step of the design process the pump type is already known, one has to use the performance curves of the selected type, made available by the manufacturer. Pump performance curves contain, in the function of the pumping rate, the following measured operational parameters:

- the head developed,
- the efficiency, and
- the power required, all for a given number (usually one) of stages.

In order to determine the required number of stages, one has to read the head developed by one stage at the desired liquid production rate and use the following formula:

$$\textbf{\textit{Stages}} = \frac{\textbf{\textit{TDH}}}{\textbf{head/stage}} \tag{7}$$

Since it would be too costly to fabricate ESP pumps with every possible number of stages, pumps are manufactured in different housings containing discrete numbers of stages. This is the reason why one should select the pump with the next available greater number of stages than the number calculated from **Eq. 7**.

5.4. Checking the Pump's Mechanical Strength

The pump selected by the previous procedure must be checked for mechanical strength of the pump shaft and the pump housing to ensure that the loading on the shaft and/or the housing do not exceed the limits specified by the manufacturer.

The strength of the pump shafts is given by the manufacturer by specifying the maximum allowed power the shaft can transmit at a frequency of 60 Hz. The actual power required by the selected ESP pump is found from the pump performance curves, where the power needed to drive a given number of stages (usually one) is plotted in the function of the pumping rate. After reading at the desired liquid rate the necessary power per stage from the performance curve, one finds the total power needed:

$$\textbf{\textit{BHP}}_{\textbf{\textit{pump}}} = \frac{\textbf{\textit{BHP}}}{\textbf{\textit{stage}}} \ \textbf{\textit{Stages}} \ \gamma_l \tag{8}$$

The total required power, BHP_{pump}, must be less than the maximum allowed power on the pump shaft, BHP_{shaft}, found from the manufacturer's technical specifications.

Manufacturers specify the mechanical strength of pump housings by publishing the allowed internal burst pressure for their pumps. This pressure should be compared to the maximum possible internal pressure which occurs when the pump develops the maximum head. Some manufacturers use the "shut-in" head valid at zero flow rate, others use the highest head found in the recommended rate range. Again, the performance curves of the selected pump have to be used to find the maximum head per stage value, from which the maximum internal pressure is found as follows:

$$p_{\max} = \left(\frac{\textbf{\textit{head}}}{\textbf{\textit{stage}}} \right)_{\max} \textbf{\textit{Stages}} \ \ \textbf{\textit{grad}}_l \tag{9}$$

For safe operation, the calculated maximum pressure must be less than the burst pressure rating of the pump housing.

6. SELECTION OF THE PROTECTOR

The protector or seal section of the ESP unit performs several vital functions for the proper operation of the installation the most important of them being absorbing the axial thrust developed in the pump. This is the reason why protectors are selected primarily on the basis of the calculated thrust load developed by the pump.

In addition to thrust load capacity, several other features have to be considered when selecting the proper protector for a particular application:

- the right size (series) is to be chosen,
- the protector shaft should be capable to transfer the required power, and
- the protector's oil expansion capacity should be sufficient.

The available sizes of protectors are compatible with motor and pump series and the proper outside diameter is selected to match the ODs of the selected motor and the pump.

Most ESP pumps belong to the floating impeller class where all axial forces developing in the stages are absorbed by the thrust washers of the stages. The only thrust occurring in such pumps is the downthrust on the pump shaft due to the shaft being exposed to a large pressure differential. Since this load is directly transferred to the protector, the load on the protector's thrust bearing is found by multiplying the cross sectional area of the pump shaft by the maximum pressure developing inside the pump, found from **Eq. 9**:

$$F_{TB} = 0.785 \; p_{\max} \; d^2 \tag{10}$$

In fixed impeller pumps (a.k.a. compression pumps), in contrast to those with floating impellers, high axial loads develop in the pump stages because the impellers are axially fixed to the shaft. Thrust forces developing on the impellers, therefore, are directly transferred to the protector's thrust bearing. The calculation of these forces, however, requires that measured thrust values for the given stage be available. To increase the safety of installation design for compression pumps, manufacturers usually publish thrust values at shut-in conditions in lb/stage units.

The capacity of the protector's thrust bearing relies on the operating temperature because the viscosity of motor oil decreases at elevated temperatures making the oil film on the bearing surfaces to become thinner. Therefore, performance diagrams have to be used and a protector with a load capacity greater than the load just calculated is selected.

The shafts of different protectors have different mechanical strengths, and manufacturers usually specify the maximum allowed power on their shafts. Therefore, the protector selected on the basis of thrust bearing load must be checked by comparing its shaft rating to the power needed to drive the pump. For proper operation, a protector with a greater shaft rating than the pump power calculated from **Eq. 8** has to be chosen.

In order to increase the protection of motors in hostile environments, to save on pulling costs, or to increase the run time of the ESP system, tandem protectors i.e. two or more sections stacked in series can be used. Such protectors may contain both bag-, and labyrinth-type chambers.

The protector's operation consumes a definite power which should be provided by the ESP motor. Most ESP equipment manufacturers (except Centrilift) include this power in the pump horsepower requirement of their published pump performance curves. For such cases the total horsepower needed to drive the ESP unit equals the pump power calculated from **Eq. 8**.

7. MOTOR SELECTION

When selecting the submersible motor to match the ESP pump already chosen, one has to determine

- the proper motor series (outside diameter),
- the required motor power, and
- the right combination of motor voltage and amperage.

Motor series denotes, just like with the pump, the OD of the motor. Again, the motor series with the largest OD that can be run in the well casing should be preferred. Many

times, motors with outside diameters different from the ESP pump are used, mainly because larger diameter motors are less expensive.

ESP motors are cooled by well fluids flowing past the motor's outside surface and the recommended minimum flow velocity required for proper cooling is 1 ft/s. To prevent the erosion of the housing, however, velocities have to be limited to 12 ft/s for clean fluids, and to 7 ft/s for fluids containing abrasives. The formula given in the following allows the calculation of flow velocities in the annulus formed by the casing string and the ESP pump:

$$v_l = 0.0119 \frac{q_l'}{ID_c^2 - OD_m^2} \tag{11}$$

The criterion for selecting the motor with the proper power capacity is the total power requirement of the ESP system, BHP_{system}, that consists of the powers needed to run (a) the pump, (b) the protector, and (c) the gas separator (if used). If no rotary gas separator is used, like in the design for geothermal wells, and the power to drive the protector is included in the pump horsepower, the ESP system's total power demand equals the pump power, BHP_{pump}, calculated from **Eq. 8**. Since ESP motors in every series are manufactured with several discrete power ratings, one should choose a motor with a nameplate rating just above the required system power, BHP_{system}.

The actual current demand of the motor is calculated from the nameplate data of the selected motor and the system's power requirement as follows:

$$I = I_{np} \frac{BHP_{system}}{HP_{np}} \tag{12}$$

Most ESP motors of a given power rating come in several versions differing from each other by the combination of their required voltage and amperage. Since electric power is defined as the product of voltage and amperage, motors with higher voltage values require less current, and vice versa. This feature gives the designer a great flexibility to achieve an optimum selection of motors for various conditions with the objective of maximizing the economy of fluid lifting.

The prime factor in selecting the motor voltage is the running depth of the ESP unit because it heavily affects the voltage drop in the electric cable. Deeper installations require longer cables and involve higher voltage drops across the cable; this leads to greater amounts of wasted electrical energy and lower system efficiencies. In such conditions, selecting a motor with a higher voltage rating means that a much lower current flows through the cable causing a lower voltage drop; consequently the amount of wasted power is reduced. Also, the use of higher voltages is advantageous in geothermal wells with high downhole temperatures because higher voltage motors need less current to develop the same horsepower, thus the operating temperature of the electric cable is reduced, and cable life is increased.

Based on the considerations just discussed and an analysis of the power flow in the ESP system, Powers [8] concludes that in most situations the motor with the highest voltage requirement is the proper choice. This not only reduces the total power consumption but many times allows the use of a smaller and less expensive power cable.

8. SELECTION OF THE POWER CABLE

The electric power cable is a vital part of the ESP system and its proper selection is not only a technical task but requires, as it will be shown later, economic considerations as well. Cable for the ESP industry is manufactured in a wide variety of types, sizes, etc.

When designing an ESP installation the right cable is selected by determining its required (a) length, (b) type, and (c) size, with proper considerations of all operational conditions.

8.1. Cable Length

The length of the power cable is determined from the running depth of the motor to which a sufficient length needed for the safe connection of surface equipment (about 100 ft) is added. The main cable (usually a round configuration) should reach down to the top of the ESP unit from where a motor lead extension (usually a flat cable section) runs to the pothead of the motor.

8.2. Cable Type

ESP cables are manufactured in a wide variety of types i.e. with different insulating and conductor materials, constructions, and armors. The proper choice primarily depends on well conditions, most importantly on well temperature, and the composition, gas content, and corrosiveness of the well fluid. The main considerations [9, 10] on the proper selection of the individual parts of the cable can be summed up as follows:

- The material of choice for cable conductors is copper, especially in deeper wells since aluminum has a lower conductivity.
- The two most common materials used for the insulation of the individual conductors are polypropylene and EPDM (ethylene propylene diene monomer), their temperature limits are 205 ºF and 400 ºF, respectively. Polypropylene is susceptible to degradation by light hydrocarbons, CO_2, and hydrocarbon gases. EPDM materials have a much wider temperature range and are less sensitive to gases.
- Jackets are made from Nitril or EPDM materials, the latter being used at higher temperatures.
- Braids or tapes provide additional strength and protection to cable components.
- Metal armor provides mechanical protection to the cable during running and pulling and the choices are galvanized or stainless steel and Monel.

8.3. Cable Size

The main considerations for selecting the size of the power cable are: (a) the physical dimensions, and (b) the voltage drop along the cable. The physical size should be chosen so that the cable fits in the annulus between the casing string and the ESP unit. The voltage drop occurring in the cable is a function of the conductor size and the motor current, and is a direct indicator of the energy losses occurring along the cable.

If the effect of conductor size on the operation of the whole ESP system is investigated, it is easy to see that smaller conductors mean greater energy losses and proportionally greater operational costs. But, at the same time, cable investment cost is lower than for a bigger conductor size. Bigger cable sizes, on the other hand, result in lower operating expenses but higher investment costs. Therefore, the selection of the optimum cable size should involve not only technical but economic considerations as well.

Optimization procedures [11, 12] are based on finding the least value of total operating costs over the expected life of the cable. The total operating cost is the sum of the capital and operating expenses and these, as described previously, vary with cable size. Since an increase of the conductor size involves increased capital costs but decreased operating costs, a cable providing the minimum of total costs can surely be found. It is easy to see that, contrary to the rules previously used, the smallest possible

size may not be the best selection. Calculation of the cost items is described in the following.

The monthly payment necessary to pay back the capital outlay for the cable over its expected life, considering the time value of money, is found from the formula used for calculating partial payments of loans. In the following formula the multiplier of the investment cost is the Capital Recovery Factor (CRF) that defines the variation of the capital cost's contribution to the total cost:

$$PB = CI \frac{(1+p)^N}{(1+p)^N - 1} p \tag{13}$$

In the formula, the monthly interest rate, p, is calculated as:

$$p = \frac{P}{1200} \tag{14}$$

The monthly operating expenses are equal to the cost of the electric power wasted along the cable. The calculation model of Vandevier [11] is detailed in the following, who used the next simplifications when calculating this cost item:

- Instead of using an average along the cable length, cable temperature is taken to be equal to the well's bottomhole temperature.
- The cable's inductive reactance is neglected because of its low value for any ESP cable.

First the total resistance of the cable (in Ohms) at well temperature is calculated from:

$$R_T = \frac{L_c\, r}{1{,}000} \left[1 + 0.00214\,(BHT - 77)\right] \tag{15}$$

The power loss in the cable (in kW units) is calculated from the cable resistance and the motor current:

$$\Delta P_c = \frac{3\, I^2\, R_T}{1{,}000} \tag{16}$$

Finally, the monthly cost of this power loss ($/month) is found as:

$$C_{cl} = 720\, \Delta P_c \frac{c_e}{100} \tag{17}$$

When using the calculation model described previously, the steps of the cable size selection are the following:

1. Based on the ampacity chart of the selected cable type the allowed amperage values of each available size are determined at the well's bottomhole temperature.
2. Cable sizes with allowed currents greater than the required motor current are selected for further economic analysis.
3. After performing the calculation of total costs for each candidate, the cable with the minimum of monthly costs is chosen.

8.4. Checking Motor Startup

It should be noted that the cable size selected affects the operating conditions of the motor especially immediately after startup. At system startup ESP motors draw more than five times greater instantaneous currents than their nameplate current. Due to the increased current a high voltage drop develops across the cable and the voltage reaching

the ESP motor may be insufficient to start the motor. Normal starts require about 50% of the motor's nameplate voltage to be available at the motor's terminals.

The following simple formula, although being an estimate only, permits a rapid check on the cooperation of the cable and the motor at startup conditions. The ratio of startup and nameplate voltages is found from:

$$\frac{U_{start}}{U_{np}} = \frac{U_{np} - 4\, I\, R_T}{U_{np}} \tag{18}$$

The selected cable size is satisfactory if this ratio is greater than 0.5, because in those conditions more than 50% of the nameplate voltage reaches the motor's terminals and no startup problems will occur.

9. SWITCHBOARD AND TRANSFORMER SELECTION

When specifying switchboards and transformers, the most important information is the maximum power of the ESP system required at the surface. This can be found from the necessary surface voltage and the motor current. Surface voltage is composed of the motor's required terminal (nameplate) voltage plus the voltage drop across the power cable. Since at this phase of the installation design the nameplate voltage has already been selected, and the cable voltage drop equals the product of cable resistance and the motor current, the installation's surface voltage requirement is found as:

$$U_{surf} = U_{np} + 1.732\, R_T\, I \tag{19}$$

From the available models, a switchboard with a rated voltage above this value is selected. The power rating of the switchboard (in kVA units) is found from the formula used to find three-phase electric power:

$$P_{surf} = \frac{\sqrt{3}\, U_{surf}\, I}{1{,}000} = 0.001732\, U_{surf}\, I \tag{20}$$

The necessary 3-phase step-up or step-down transformer should have the same kVA rating as the switchboard.

10. MISCELLANEOUS EQUIPMENT

At this point of the design procedure, all important parts of the ESP installation are selected and a detailed order can be placed to the manufacturer. The only remaining pieces of equipment can easily be chosen from the manufacturer's catalog and only a listing with the most important considerations is given in the following.

Downhole Equipment

- Motor lead extension is a flat cable section whose length should be about 6 ft longer than the combined length of the gas separator, pump, and protector.
- Flat cable guards should be installed along the ESP unit and the necessary number of 18 in sections is chosen.
- Cable bands on the power cable are spaced every 15 ft along the tubing string; and 2 ft apart along the flat cable.
- Check and drain valves are selected to be compatible with the tubing size.

Surface Equipment

- Up-to-date wellheads use power feed-through connections and are to be chosen to be compatible with the well's casinghead, tubing, and power cable sizes.
- A junction box is needed to provide a connection point for the power and surface cables and is selected from available models.
- Surface cable should have sufficient length to reach from the junction box to the switchboard and must be at least the same size as the power cable.
- Service equipment includes cable reels, reel supports, and cable guide wheels; they should match the selected cable sizes.

11. CONCLUSIONS

The paper introduces the design of ESP installations capable of producing geothermal water wells. Basic design principles and practical recommendations are discussed for the selection of the components of the electrical submersible pumping system. Conclusions related to system design can be summarized as follows.

- ESP installations are ideally suited for producing water from geothermal wells.
- Design of the installation is based on the proper selection of the submersible pump.
- The proper selection of the electrical cable involves an economic study to find the cable size that provides the least amount of total cost over the life of the equipment.

ACKNOWLEDGEMENT

This work was carried out as part of the TÁMOP-4.2.1.B-10/2/KONV-2010-0001 project in the framework of the New Hungarian Development Plan. The realization of this project is supported by the European Union, co-financed by the European Social Fund.

LIST OF SYMBOLS

B_w	water volume factor at pump suction pressure	bbl/STB
BHP/stage	the power needed to drive one pump stage	HP/stage
BHP_{system}	power requirement of the ESP system	HP
BHT	bottomhole temperature	ºF
c_e	cost of electric power	c/kWh
CHP	casinghead pressure	psi
CI	capital investment for cable	$
d	pump shaft diameter	in
$grad_l$	fluid gradient in the annulus	psi/ft
$grad_w$, $grad_g$	water and gas gradients in the annulus	psi/ft
HP_{np}	nameplate power of the motor	HP
head/stage	head developed by one stage of the selected pump	ft
$(head/stage)_{max}$	shut-in head developed by one pump stage	ft
I	required motor current	Amps
I_{np}	nameplate current of the motor	Amps
ID_c	inside diameter of the casing string	in
L_c	cable length	ft
L_{dyn}	TVD of the dynamic liquid level	ft
L_{perf}	TVD of perforations	ft
L_{set}	TVD of pump setting	ft
L_t	measured tubing length to the pump setting depth	ft

N	expected life of the cable	months
OD_m	outside diameter of the motor	in
p_{max}	maximum internal pressure in the pump	psi
P	prime interest rate	%/year
PI	productivity index	STB/d/psi
PIP	pump intake pressure	psi
q	liquid rate	STB/d
q_l',	"in-situ" water flow rate	bpd
q_w	water volumetric rate	STB/d
r	resistance of conductor at 77ºF	Ohm/1,000 ft
R_T	cable resistance	Ohms
$Stages$	the selected number of pump stages	-
$SBHP$	static bottomhole pressure	psi
U_{np}	motor nameplate voltage	Volts
U_{surf}	required surface voltage	Volts
WHP	producing wellhead pressure	psi
ΔH_{fr}	frictional head loss in the tubing string	ft
γ_l	specific gravity of the produced liquid	-

REFERENCES

1. *"Recommended Practice for Sizing and Selection of Electric Submersible Pump Installations."* API RP 11S4, 3rd Ed., American Petroleum Institute, 2002.
2. *The 9 Step*. Baker-Hughes Centrilift, Claremore, Oklahoma, 2001.
3. *Submersible Pump Handbook*. 6th Ed. Centrilift-Hughes, Inc. Claremore, Oklahoma, 1997.
4. *Quality Submergible Pumps for the Petroleum Industry. Reda, A Camco* Company, 1996.
5. Legg, L. V.: *"Simple Plan for High-WOR Wells Improves Efficiency."* OGJ July 9, 1979, 127–31.
6. Legg, L. V.: *"Correct Electrical Components Boost Production from High-WOR Wells."* OGJ July 23, 1979, 60–3.
7. Nolen, K. B.–Gibbs, S. G.: *"How to Match Submersible Pumps to Well Performance."* WO February 1, 1985. 41–5.
8. Powers, M. L.: *"Economic Considerations for Sizing Tubing and Power Cable for Electric Submersible Pumps."* Paper SPE 15423 presented at the 61st Annual Technical Conference and Exhibition held in New Orleans, October 5–8, 1986.
9. Tijunelis, D. – Wargin, R.: *"Cable Selection Process for Submersible Oil Well Pumps."* Proc. 24th Southwestern Petroleum Short Course. Lubbock, April 21–2, 1977, 181–5.
10. *"Recommended Practice for Application of Electric Submersible Cable Systems."* API RP 11S5, 1st Ed., American Petroleum Institute, 1993.
11. Vandevier, J. E.: *"Optimum Power Cable Sizing for Electric Submersible Pumps."* Paper SPE 16195 presented at the Production Operations Symposium held in Oklahoma City, March 8–10, 1987.
12. French, S. W.: *"Optimum Cable Selection of Electrical Submersible Pumps."* Paper SPE 21693 presented at the Production Operations Symposium held in Oklahoma City, April 7–9, 1991.

Geosciences and Engineering, Vol. 2, No. 3 (2013), pp. 37–43.

DEVELOPMENT OF AUTOMATIC CONTROL OF MULTI-STAGE TRIAXIAL TESTS AT THE UNIVERSITY OF MISKOLC

BALÁZS CSUHANICS–ÁKOS DEBRECZENI
Institute of Mining and Geotechnical Engineering
University of Miskolc
H-3515 Miskolc-Egyetemváros, Hungary
bgtda@uni-miskolc.hu

ABSTRACT

During rock mechanical examinations (either in case of the measurements of slope stability or planning of underground cavities and boreholes) one of the most important tasks is to determine the failure curves of rocks. For determining a generalized hyperbolic envelope minimum three parameters are necessary: tensile strength, uniaxial compressive strength and the triaxial compressive strengths with different confining pressure. With the application of the latest measurement system installed in rock mechanical laboratory of University of Miskolc, where multi-stage triaxial tests can be carried out besides conventional triaxial tests to measure triaxial compressive strength.

A series of multi-stage triaxial compression tests were conducted to examine which measurement setup and control mode could most precisely determine the failure points separating the single load stages during the tests because the precise recognition of these is a critical point of the measurement. It was found that brittleness played an important role in choosing the adequate measuring mode (manual or automatic) and control signal (inductive transducer, strain gauge).

1. INTRODUCTION

Three different test types are suggested by ISRM (International Society for Rock Mechanics) for the determination of failure envelope such as individual or single-stage triaxial test, multiple failure state or multi-stage triaxial test (MFS) and continuous failure state (CFS) test. Three single-stage triaxial tests are required to generate a complete failure envelope; consequently three specimens are required at least, while one multi-stage triaxial test may give the complete failure envelope using only one specimen.

The primarily advantage of the multi-stage triaxial test method manifests itself whenever availability is limited and therefore the specimens are expensive. This could be a crucial issue primarily for the rock specimens obtained from deep drilling. Two different methods may be adopted to perform the common multi-stage triaxial test in the practice: the conventional ISRM suggested method [3], and its slightly modified version [1].

1.1. Multi-stage triaxial test according to the recommendation of ISRM

The ISRM recommended testing procedure could be divided into sub- stages as shown below. As a starting step, the axial load and the confining pressure should be increased until both of them reach the value of the confining pressure (p_0 represents this confining pressure value) of the first stage, bringing the specimen into hydrostatic condition.

In the next phase of the test the axial load is then increased keeping confining pressure p_0 constant until the corresponding failure point is observed in the axial stress – axial strain curve (Point A in *Figure 1*). The axial load is being increased while the strain rate is kept constant (displacement controlled test). Failure is defined as the point in the stress–axial strain curve where the curve declines in a given degree from the curve fitted on previously measured $\sigma - \varepsilon$ points, namely when the residual deformation exceeds a threshold value we have preliminary adjusted.

The confining pressure is then increased to the next level in one step, namely from A to A' in Figure 1. This step is followed by an axial load increase using the procedure described above. Repeatedly increasing the axial load – confining pressure steps we get to the point in the measuring process when the required highest confining pressure is reached (B' in *Figure 1*). The confining pressure will then be kept constant, while the axial loading is continued till the failure of the specimen (Point C in *Figure 1*). After the failure the axial load will fall back to its residual value (Point D, *Figure 1*). The confining pressure is progressively reduced until the specimen is completely unloaded. During the unloading phase the axial stress as a function of confining pressure curve will follow the residual strength envelope. [3]

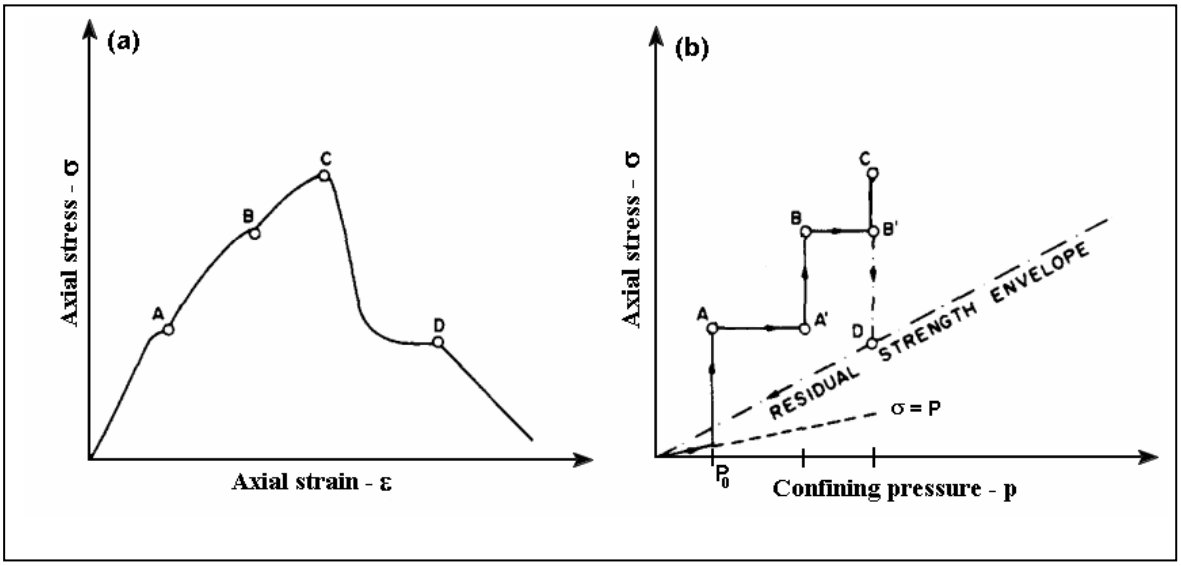

Figure 1.
Multi-stage triaxial test: (a) axial stress – axial strain curve (b) axial stress – confining pressure curve [3]

The authors [3] described the configuration of the testing equipment which is contained by the ISRM recommendation, as well.

1.2. Modified multi-stage triaxial testing method

The modified multi-stage triaxial testing, which is also widely used in practice, is a slight modification of the testing method suggested by the ISRM [2]. The difference between the two methods arises from the fact that after reaching the first imminent failure point, the vertical load is released to the level of the actual confining pressure, developing a hydrostatical state. (*Figure 2*) After this stage, the next desired confining pressure level will be reached while continuously keeping up the hydrostatical state, and then the vertical load is increased till the next failure point. This loading cycle has to repeat starting it from a higher and an even higher hydrostatic phase. According to the developers of the modified testing method, the comparison of the modified multi-stage triaxial method and the single stage triaxial testing results indicates that the modified method is suitable to determine the triaxial strength envelope for brittle rocks. [1]

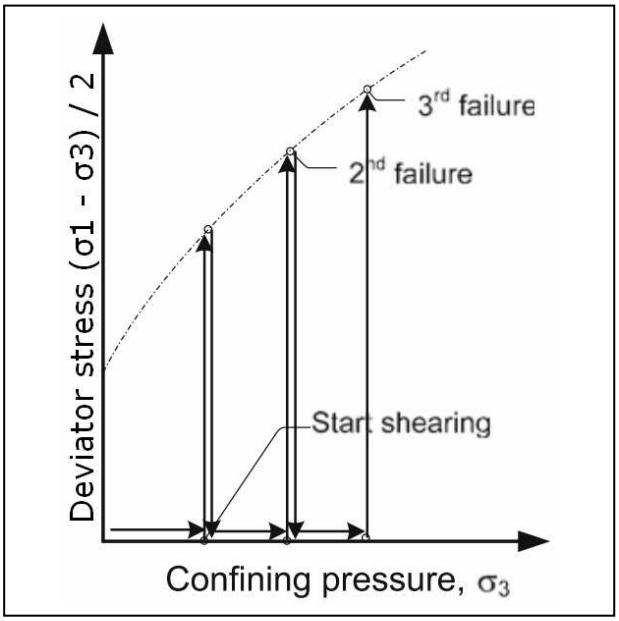

Figure 2.
Stress paths of modified multi-stage triaxial test [2]

According to the literature [1], multi-stage triaxial test has been proven to yield a strong correlation to single stage triaxial test results. The authors highlight that the selection of failure point significantly relies on the experimenter's judgment, since the experimenter should define them during the experiments. The control modes based on real time data processing are suitable for replacing the subjective, individual judgment.

2. MATERIALS AND METHODS

Different rock materials were used in order to gain experiences about the best possible adjustments and set up of the measuring system while testing brittle and ductile rock specimens. Specimens were cut away from andesite, rhyolite and sandstone blocks. Andesite specimens represented the brittle rock type, whereas rhyolite and sandstone specimens represented the transition between brittle and ductile rocks. Two sample groups were defined for the tests.

Table 1

Rock materials used for the tests

Rock type	Quantity [pieces]	Slender ratio	Average uniaxial compressive strength [MPa]
Andesite	3	1.9	170
Rhyolite	4	1.9	73
Sandstone	1	1.9	66

The axial deformations of andesite, rhyolite and sandstone specimens of the first group are measured by inductive transducers in order to control the load. The andesite and rhyolite specimens of the second group are equipped with strain gauges with perpendicular position to the axis of the cylindrical specimens, therefore in this group the load control based on the gauge measuring relative deformation. Relevant reference of the ISRM contains the regulation of sample preparation [1], therefore they are not detailed here.

2.1. Testing equipment

During the tests Hoek triaxial cells were used in which the confining pressure is produced by oil pressure, the axial load is prepared by a high capacity test frame. The Italian Controls testing apparatus were used to make up of the following parts: a 3000 kN loading capacity loading machine is connected to an Advantest 9 servo hydraulic testing unit furthermore a 700 bar confining pressure capacity triaxial unit linked with a Sercomp 7 automatic control console.

The advanced pressure controller capacitates the testing apparatus to perform multi-stage triaxial tests during which the applied load can be regularly reducible or increasable. The whole measurement process can be controlled by the TriaxRocks software developed for multi-stage triaxial tests. To meet our requirements the measuring system had to be able to perform multi-stage tests. The test frame is principally designed for concrete tests, therefore we had to elaborate numerous adjusting modifications for rock materials before the tests.

The manufacturer took into consideration our remarks when programming the TriaxRocks software. It was designed in compliance with our requirements to control specifically multi-stage triaxial tests. We personally took part in the beta test of the software in Milan.

2.2. Applied control methods during the test stages

The test progress forms two stages in terms of controlling. During the first stage load transducer controls the initial confining pressure and the axial loading until confining pressure reaches the value of the first step. The second examination stage starts right after reaching the value of the initial confining pressure. At this stage the experimenter could choose to use the signal of inductive displacement transducers measuring the axial deformation or to use strain gauges sticking on axial as well as perpendicular position to the axis of the cylindrical specimens for controlling the loading stages.

The real-time data processing of the measuring system allows the user to switch in any phase of the test from the subjective manual activation of the pressure step to the automatic recognition of the failure (or residual strength). The pressure step is then, in any case, performed automatically. The system in automatic mode tries to detect the approach of a failure of the sample by monitoring the instantaneous elastic modulus variation. This instantaneous elastic modulus is calculated as a ratio between the load change and deformation change on a time interval, where the time interval is user settable. If this ratio exceeds a settable threshold (different threshold is also to be defined for the residual phase) the software will start a next pressure step in three phases:

- The vertical load is reduced by a given amount, and the control of the test frame switches from displacement/strain control to load control;
- The cell pressure increases (if the test is in the increasing load phase) or decreases (if the test is in the residual – decreasing load – phase);
- The vertical control is switched again to displacement/strain and the test goes on.

3. RESULTS

We concluded that the multi-stage triaxial tests of rhyolite, which represents transition between tough and brittle rocks could be accomplished both in automatic and manual modes. (*Figure 3*)

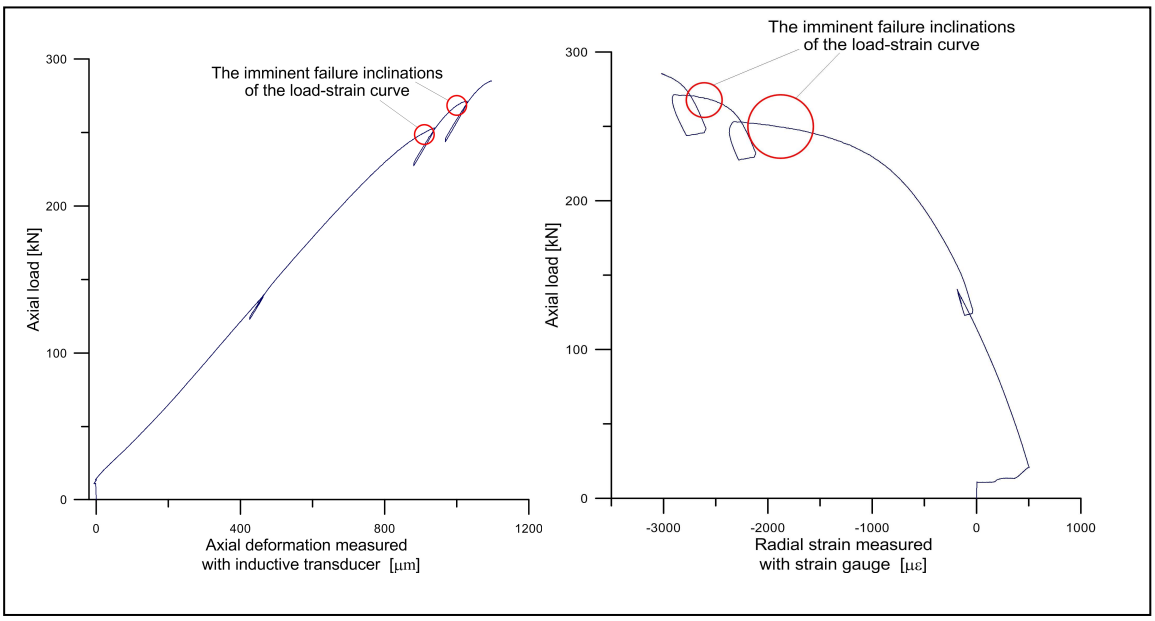

Figure 3. a), b)
a) axial load – axial strain curve of rhyolite sample during the load increasing phases
b) axial load – radial strain of rhyolite sample during the load increasing phases

It was found that the failure points could be recognized more precisely based on the radial deformation measurements performed by strain gauges in horizontal position to the cylindrical specimen's axis than using inductive displacement transducers measuring the axial deformation in case of andesite specimens, which represented the brittle rocks (*Figure 4*). The plastic limit and breaking limit lie close to each other; therefore the possibility of an accidental failure is less in automatic mode, using a proper threshold.

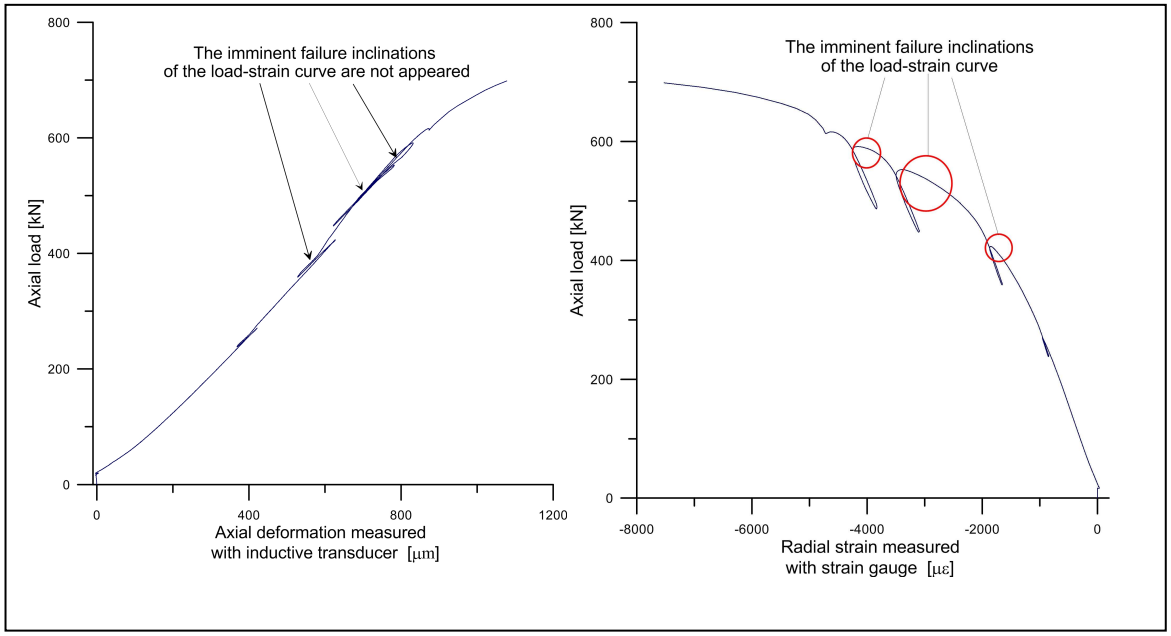

Figure 4. a) b)
a) axial load – axial strain curve of andesite sample during the load increasing phases
b) axial load – radial strain of andesite sample during the load increasing phases

The sandstone specimen was not appropriate for the strain gauge measuring through the discontinuous mantle of the sample, which does not allow the sticking on the strain gauge, therefore its axial strain was measured with inductive transducers. When we test tough rocks, the measurement could be accomplished both in automatic and manual modes because the failure points are uniquely determined by the transducers, as well.

4. CONCLUSIONS

To sum up, we conducted a series of multi-stage triaxial tests using different rock types to define the best adjustments, control method and measuring mode. We concluded that the automatic measuring mode of the multi-stage triaxial tests supported by real-time data processing is suitable for replacing the subjective, individual judgment of the experimenter.

It was found that both the signal of inductive transducers and strain gauges are possible for the experimenter to choose to control the load of the specimen but our experience showed that during the tests of brittle samples an unpredictable failure may damage the strain gauge, making further measurements of that specimen impossible. The adequate selection of the measuring mode (manual or automatic) and control signal (inductive transducer, strain gauge) should depend on the brittleness, homogeneity and mantle property of the specimen.

ACKNOWLEDGEMENT

This work was carried out as part of the TÁMOP-4.2.1.B-10/2/KONV-2010-0001 project in the framework of the New Hungarian Development Plan. The realization of this project was supported by the European Union and, co-financed by the European Social Fund.

REFERENCES

1. Crawford, A. M.–Wylie, D. A.: *"Modified multiple failure state triaxial testing method."* Proceedings 28th US Symposium on Rock Mechanics, Tucson, June 29–July 1, 1987, pp. 133–140.
2. Youn, H.–Tonon, F.: *"Multi-stage triaxial test on brittle rock."* International Journal of Rock Mechanics & Mining Sciences 47. 2010, pp. 678–684.
3. Kovári, K.–Tisa, A.–Einstein, H. H.–Franklin, J. A.: *"Suggested methods for determining the strength of rock materials in triaxial compression: revised version."* ISRM – Commission on Testing Methods, International Journal of Rock Mechanics and Mining Sciences Vol. 20, No. 6 1983, pp. 285–290.

Geosciences and Engineering Vol 2, No. 3 (2013), pp. 45–50.

INVESTIGATION OF HEAVY METALS EXTRACTION FROM SURFACE SAMPLES OF A WASTE DUMP OF RUDABÁNYA

MÁRTON TÓTH[1]–FERENC MÓRICZ[2]–BALÁZS KOVÁCS[3]
[1, 3]Department of Hydrogeology and Engineering Geology
[2]Department of Mineralogy and Petrography
University of Miskolc

ABSTRACT

The muriatic and aqueous extractions of surface samples from waste dumps of Rudabánya have been investigated to determine the amount of mobile heavy metals at different pH values. The minerals of heavy metals were found immobile using distilled water at pH 7 but 0.1 M HCl solution could solve several mineral compounds. The highest measured concentrations after muriatic extraction for Zn, Pb, Hg were 1.97 mg/kg, 0.27 mg/kg, 0.022 mg/kg respectively on the selected waste dump. Due to the fact that the process in real-world takes place at weak acidic conditions the data of muriatic extractions are overestimated meanwhile those of aqueous extraction are underestimated. To model the real situation more accurately multi-step extraction is to be performed in the future.

INTRODUCTION

Generally, the waste dumps of abandoned multi-ore mines have huge heavy metal content which influences significantly the quality of surface and subsurface water. There are some dangerous ones which have high toxicity. To know the migration processes of these metals is important because their ecological and health risks are notable. Our research site is the abandoned ore mine site of Rudabánya where mainly the migrations of mercury, lead, copper, and zinc are investigated.

Rudabánya is one of the old multi-ore mines of North Hungary but the exploitation of mine was finished in 1985. The genesis of ores at Rudabánya was hydrothermal by metasomatism in the Jurassic period. The geology of site in this geological age was favorable for metasomatism, because the dolomite (Gutenstein Formation), and the limestone (Jósvafő Limestone) which are the main host rocks of ores, were broken up and the metasomatism could come off on the higher surface of the rocks [1]. During metasomatism the calcium and magnesium ions of dolomite ($CaMg[CO_3]_2$) were changed to iron. Firstly the siderite ($FeCO_3$) (iron spar) and limonite ($Fe_2O_3 \times nH_2O$) (brown iron-ore) ore deposits were generated. Later these iron ore bed were impregnated by another hydrothermal solution which generated the ores of special elements on the site [2]. These elements are copper, lead, mercury and zinc. The main ore in the case of copper is chalcopyrite ($CuFeS_2$) (copper pyrite), in the case of lead it is galena (PbS) (lead sulfide), and in the case of zinc it is sphalerite ([Zn, Fe]S) (zinc-blende).

Heavy metals in the residues from mining and metallurgical operations are often dispersed by water after their disposal [3]. In Rudabánya a lot of waste dumps were created during hundred years long mining activities which still have significant heavy metal content.

The contamination of water by dissolved metals in mining areas has mainly been associated with the oxidation of sulfide-bearing minerals. By help of precipitation liquids of result acidic pH is formed which can mobilize the heavy metals and cause a high level of dissolved metals in the groundwater, such as copper and zinc, and anions, such as sulfates and carbonates [4, 5].

The extent and degree of heavy metal contamination around mines depends on geochemical characteristics and degree of mineralization of the tailings [6]. Rudabánya mine

has a special geochemistry among multi-ore mines because carbonate ores have domination on the site.

Sequential extraction is a method to evaluate secondary mineralogy as a product of sulfide oxidation, and sorption of hazardous heavy metals which based on the chemical composition of gradual stronger leach solution starting with distilled water and ending with strong acids for total digestion [7, 8].

In the literature several sequential extraction methods are known like as Tessier's [10] 5 steps method, BCR [11] 3 steps method, MSZ-21470-50:2006 [12] 4 steps method and Dold's [9] 7 steps method. The eye-catching differences between methods are the steps of extractions. The most refined method is the Dold's sequential extraction because in the long stepwise digestion the separations of different minerals are more accurate (*Table 1*).

Table 1

Steps of Dold extraction [9]

Step	Leaching	Preferentially dissolved minerals
1	Water-soluble fraction *(1.0 g sample into 50 ml deionizied H_2O shake for 1 h)*	secondary sulfates, e.g., bonattite /$CuSO_4 \cdot 3(H_2O)$/, chalcanthite /$CuSO_4 \cdot 5(H_2O)$/, gypsum /$CaSO_4 \cdot 2(H_2O)$/, pickeringite /$MgAl_2(SO_4)_4 \cdot 22(H_2O)$/
2	Exchangeable fraction *(1 M ammonium-acetate pH 4.5 shake for 2 h)*	calcite /$CaCO_3$/, vermiculite-type mixed layer, adsorbed and exchangeable ions
3	Fe^{III} oxyhydroxides *(0.2 M ammonium-oxalate pH 3.0 shake for 1 h in darkness)*	schwertmannite /$Fe^{III}_{16}O_{16}(OH)_{12}(SO_4)_2$/, two-line ferrihydrite, secondary jarosite /$KFe^{III}_3(SO_4)_2(OH)_6$/, pyrolusite /$MnO_2$/
4	Fe^{III} oxides *(0.2 M ammonium-oxalate pH 3.0 heat in water bath 80 °C for 2 h)*	goethite /$Fe^{III}O(OH)$/, jarosite /$KFe^{III}_3(SO_4)_2(OH)_6$/, Na-jarosite /$NaFe^{III}_3(SO_4)_2(OH)_6$/, hematite /$Fe_2O_3$/, manganite /MnO(OH
5	Organics and secondary Cu sulfides *(35% H_2O_2 heat in water bath for 1 h)*	organics , covellite /CuS/, chalcocite – digenite (chalcocite /Cu_2S/, djurleite /$Cu_{31}S_{16}$/ and digenite /Cu_9S_5/)
6	Primary sulfides *(combination of $KClO_3$ and HCl, followed by 4 M HNO_3 boiling)*	pyrite /FeS_2/, chalcopyrite /$CuFeS_2$/, bornite /Cu_5FeS_4/, sphalerite /(Zn,Fe)S/, galena /PbS/, molybdenite /MoS_2/, cinnabar /HgS/, orpiment /As_2S_3/,
7	Residual *(HNO_3, HF, $HClO_4$, HCl digestion)*	silicates, residual

In our paper the aqueous and muriatic extractions will be investigated which are generally the start and the end or before end steps of sequential extractions.

MATERIALS AND METHODS

Several waste dumps are located on the mine site of Rudabánya. The investigated one is shown on *Figure 1*. Eight sampling points were denoted, seven were on the top of waste dump and one was at the foot of dump (signed by L.A.). Two cross-sections were formed by the seven points, the first cross-section (signed by points 1/1, 1/2, 1/3, 1/4, 1/5) was in north-south direction and the second cross-section (signed by points 2/1, 2/2) was in east-west direction (Figure 1).

The soil samples were prepared in pestle and after sieving the fractions down to 0.2 mm diameters were utilized in extraction investigation also in determination of aqueous and potassium chloride pHs.

In pH determination the ratio of soil and liquid was 1:2.5 and the investigation was performed after 12 hours' rest by potentiometer.

At aqueous extraction 5 g sample was extracted at room temperature for 2 hours with 100 cm^3 distilled water with continuous agitation. After extraction the solutions were filtered twice by GE Laboratory membrane filters (GE FILT. SA710F 11CM), the second was after

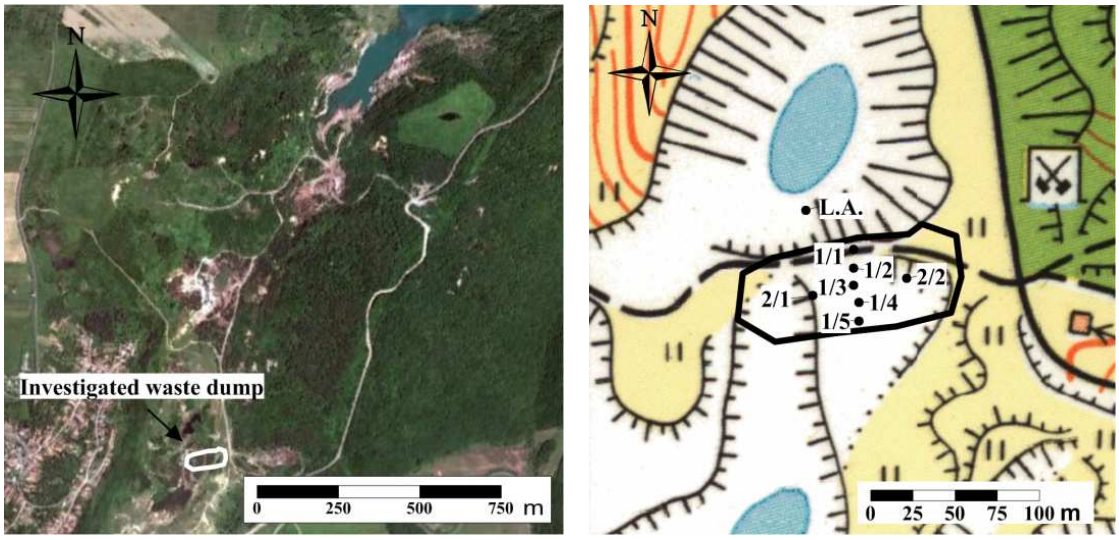

Figure 1.
The location of investigated waste dump on the mine site of Rudabánya and location of sampling points

boiling of filtrate to improve the effect of filtering. The prepared filtrates were analysed in a UniCam 929 atomic absorption spectrophotometer (AAS).

At muriatic extraction 5 g sample was extracted at room temperature for 2 hours with 100 cm^3 hydrochloric solution (0.1 M HCl) with continuous agitation. After extraction the solutions were filtered. The prepared filtrates were also analysed in AAS.

Ca, Mg, Hg, Pb, Zn, Fe elements were analysed in the AAS while sodium and potassium were also analysed in the UniCam 929 but with atomic emission spectrometer (AES) function of equipment.

RESULTS

The pH of samples shows that the environment has alkaline reaction which was caused by carbonates (*Table 2*).

Table 2

Reaction of samples

Sample	Aqueous pH	Potassium chloride pH
1/1	7.82	8
1/2	8.08	8.14
1/3	8.15	8.13
1/4	7.99	8.07
1/5	7.96	8.08
2/1	7.95	7.95
2/2	7.85	7.82
L.A.	7.88	7.81

To compare the applied extraction methods with Dold's sequential extraction the distilled water extraction is the first step, the muriatic extraction is the reduced sixth step of Dold extraction. During aqueous extraction the secondary sulfates were dissolved but the muriatic extraction was a huge jump after distilled water which skipped across 4 steps (Table 1) so this extract included the absorbed and exchangeable ions, residue of dissolution of Fe^{III} oxyhydroxides, Fe^{III} oxides, organics and secondary Cu sulfides and maybe the primary sulfides as well. After extraction the changes in the pH were not detected but probably they changed due to the high carbonate content of samples. This buffer capacity of soil samples could inhibit the dissolution of primary sulfides.

After aqueous extraction lead and zinc were detected in case of some sample points (*Table 3*). In the case of zinc it means that samples included zinc sulfates which could be solved in water easily. In the case of lead there were three samples where lead was observed but it must be a mineral different from secondary sulfates because the lead sulfate is insoluble not only in water but also in weak acid. The calcium and magnesium content of samples was higher than sodium and potassium content. The presence of calcium and magnesium in aqueous extract proves its calcium and magnesium sulfate content.

Table 3

Results of aqueous extraction

Sample	Ca mg/g	Mg mg/g	Na mg/g	K mg/g	Fe mg/g	Hg mg/g	Pb mg/g	Zn mg/g
1/1	0.226	0.143	0.051	0.034	udl	udl	udl	udl
1/2	0.205	0.193	0.036	0.041	udl	udl	0.006	udl
1/3	0.176	0.083	0.039	0.035	udl	udl	udl	0.001
1/4	0.172	0.081	0.032	0.026	udl	udl	udl	0.001
1/5	0.193	0.080	0.041	0.033	udl	udl	udl	0.001
2/1	0.187	0.105	0.077	0.066	udl	udl	0.001	0.001
2/2	0.202	0.095	0.056	0.071	udl	udl	0.003	0.001
L.A.	0.101	0.045	0.063	0.106	udl	udl	udl	0.003

udl – under detectable limit (< 0.001)

After muriatic extraction the concentration of investigated elements increased significantly. The calcium and magnesium content of samples was high due to the presence of carbonates which could be easily solved by hydrochloric acid. The host rock of mineralization was limestone ($CaCO_3$) and dolomite ($CaMg[CO_3]_2$) that originates the high concentration of calcium and magnesium. Also the high carbonate content has correlation with alkalinity of soil samples (*Table 4*).

Table 4

Results of muriatic extraction

Sample	Ca mg/g	Mg mg/g	Na mg/g	K mg/g	Fe mg/g	Hg mg/g	Pb mg/g	Zn mg/g
1/1	18.07	8.70	0.04	0.05	0.69	udl	0.06	0.59
1/2	18.15	9.12	0.04	0.07	3.35	0.001	0.27	0.95
1/3	18.43	9.02	0.04	0.05	2.31	0.001	0.12	0.31
1/4	18.14	9.12	0.05	0.04	2.66	udl	0.08	1.97
1/5	18.37	9.17	0.04	0.04	1.47	udl	0.06	0.66
2/1	21.54	6.62	0.05	0.05	0.03	0.021	udl	0.33
2/2	24.78	5.14	0.04	0.06	udl	0.022	udl	udl
L.A.	19.02	10.01	0.05	0.08	1.03	0.009	0.03	0.32

udl – under detectable limit (< 0.001)

To compare the aqueous and muriatic extraction the concentration of sodium and potassium were not changed. It means there are no other minerals on higher dissolution steps on the site which have sodium and potassium content.

The iron content of extracts was changed significantly in muriatic extraction. This additional iron content could be originated from iron carbonates because sideritic ore was also exploited on the site or from Fe^{III} oxyhydroxides and Fe^{III} oxides or from primary sulfides.

The heavy metal content of the muriatic extracts was also higher compared to aqueous ones. It was caused by dissolution of sulfides like sphalerite, galena and cinnabar or mobilization of metals from surface of inorganic, organic colloids, like fulvates and humic acid. The highest mercury content were detected at the sampling points 2/1 and 2/2, in the case of lead point 1/2, in the case of zinc point 1/4 was found to be the most concentrated.

CONCLUSIONS

The extraction test can provide information about the mobilization of heavy metal content of waste dumps of Rudabánya. This information is integrant to model the correct migration process of heavy metals.

The dissolution of minerals largely depends on aggressivity of solvent. In our experiments extractions of distilled water and 0.1 M HCl solution were investigated on samples of the waste dump. In aqueous extraction on neutral pH the heavy metals (mercury, lead, zinc) could not be dissolved or the dissolved volume was negligible (Table 3). But during muriatic extraction the mobilization of heavy metals became significant (Table 4). This extreme acidic environment is not typical on the mine site of Rudabánya so the amount of mobile heavy metals in muriatic extraction is over-estimated. Generally, the reaction of rainfall is not neutral because of dissolution of CO_2, SO_2 etc. so the dissolved amount of heavy metals in aqueous extraction is under-estimated. By the application of Dold's extraction method the amounts of heavy metals are determined which could also be mobilized by effect of weak acid.

The results of sequential extractions will be more useful to model the natural conditions at the site.

ACKNOWLEDGEMENT

This work was carried out as part of the TÁMOP-4.2.1.B-10/2/KONV-2010-0001 project in the framework of the New Hungarian Development Plan. The realization of this project was supported by the European Union and, co-financed by the European Social Fund.

REFERENCES

1. Szentpétery I.–Less Gy.: *„Az Aggtelek-Rudabányai-hegység földtana."* Magyar Állami Földtani Intézet, Budapest (2006), 92. p.
2. Hartai É.: *„Teleptani alapismeretek."* Egyetemi jegyzet. Miskolci Egyetem, Műszaki Földtudományi Kar, Miskolc (2005), 62. p.
3. Johnson, M.S.–Cooke, J. A.–Stevenson, J. K. W.: *"Revegetation of metalliferous wastes and land after metal mining."* In: Hester, R. E., Harrison, R. M. (Eds.), Mining and Its Environmental Impact. Royal Society of Chemistry. (1994), 164. p.
4. Pentreath, R. J.: *"The discharge of waters from active and abandoned mines"*. In: Hester, R. E., Harrison, R. M. (Eds.), Mining and Its Environmental Impact. Royal Society of Chemistry. (1994), 164. p.
5. Salomons, W.: *"Environmental impact of metals derived from mining activities: processes, predictions, prevention"*. Journal of Geochemical Exploration, Vol. 52 (1995), 5–23. pp.
6. Johnson, R. H.–Blowes, D. W.–Robertson, W. D.–Jambor, J. L.: *"The hydrogeochemistry of the nickel rim mine tailings impoundment"*. Sudbury, Ontario. Journal of Contaminant Hydrology, Vol. 41 (2000), 49–80. pp.
7. SARB Consulting: *"Geochemistry and hydrology of tailings and waste rocks."* (Short course). Draft, Chapter 6. (2000).
8. Móricz, F.: *"Kinetic testing and mineralogical characterization of sulfide mine wastes from the Oruro deposit (Bolivia)."* Diploma thesis (2009).
9. Dold, B.–Fontboté, L.: *"A mineralogical and geochemical study of element mobility in sulfide mine tailings of Fe oxide Cu-Au deposits from the Punta del Cobre belt, northern Chile."* Chemical Geology, Vol. 189, (2002), 135–163. pp.
10. Tessier, A.–Campbell, P. G. C.–Bisson, M.: *"Sequential extraction procedure for the speciation of particular trace metals."* Anal. Chem., Vol. 51 (1979), 844–851. pp.
11. Ure, A. M.–Quevauviller, Ph.–Muntau, H.–Griepink, B.: *B. EUR report.* CEC Brussels, 14763, 1992:85. (1992).
12. MSZ 21470-50:2006 *Környezetvédelmi talajvizsgálatok*. Az összes és az oldható toxikuselem-, a nehézfém- és a króm(VI)tartalom meghatározása

Geosciences and Engineering, Vol. 2, No. 3 (2013), pp. 51–62.

BASES OF FD MODELLING FOR EM UNDERGROUND TRANSILLUMINATION WITH VERTICAL ELECTRIC DIPOLES IN 2D ANISOTROPIC CONDUCTIVITY STRUCTURES

GÁBOR PETHŐ
Department of Geophysics
University of Miskolc

ABSTRACT

The fundamental relationships are derived for frequency domain 2.5D situation when the transmitter is an underground vertical electric dipole source and its electromagnetic fields are observed in another borehole or in a gallery. Derivations are provided for both the isotropic and the anisotropic case. From the Fourier transforms of the Maxwell's equations coupled partial differential equations are derived, in which – besides the spatial strike directional wavenumber, the frequency and the electromagnetic rock properties – only the strike direction electromagnetic (EM) field components and their partial derivatives in the wavenumber (k_x) domain can be found. On the basis of comparison between the differential equations for the isotropic and anisotropic case it can be experienced that in contrast with the isotropic situation second order mixed partial derivatives of strike directional Fourier EM field component are in the anisotropic case. In the differential equations for the anisotropic case except the coefficient of the strike directional Fourier magnetic field component all coefficients reflect the effect of anisotropy. The equations for the spatial solutions of EM field components can be given by inverse Fourier transformation. The numerical experience gained for isotropic 2.5D TE and TM mode can be taken into account in the course of grid and spatial wavenumber domain planning in the anisotropic situation.

Keywords: anisotropy, elongated structure, frequency domain electromagnetic method, FD procedure, wavenumber domain, inverse Fourier transformation.

1. INTRODUCTION

In the course of hydrocarbon and geothermal exploration the geophysical EM methods are among the most important ones after seismic reflection survey, and the simultaneous application of the two geophysical methods is very effective. The ground-based geophysical EM methods use either natural or artificial sources [1, 2]. The attenuation of the EM fields can be described in the function of EM parameters including electrical conductivity, dielectric permittivity, magnetic permeability and frequency in general [3]. The borehole EM methods always apply transmitter(s) sending EM waves at different frequencies and receiver(s) measuring the transit time but at least wave-amplitude attenuation of the emitted EM waves [4]. The transmitters and the receivers are on the same tool body. In this paper emphasis is put on the lower frequency range where the attenuation of EM fields in homogeneous space can be characterized by the induction number which is the ratio of the transmitter-receiver separation and the skin depth [5]. In the situation presented here the source field is a vertical electric dipole source and the investigated conductivity structure is elongated. For this reason the problem to be solved is a 3D one. In order to handle the original problem more easily the EM source is considered mathematically as a point source. This situation is called a 2.5D forward problem. In the course of EM investigation on elongated conductivity structures exited by electric dipole distinction is made between TE mode, when the electric source field is parallel to the structural strike, and TM mode, when the electric source field is perpendicular to it. In contrast with MT 2D these modes are not separate from each other they are coupled. In the case of vertical electric dipole source the

derivation is very similar to those of horizontal electric dipole sources [6]. The investigation of some effects for elongated isotropic conductivity inhomogeneities exited by horizontal electric dipole source was presented by [7–12]. These papers dealt with the determination of EM responses over 2D isotropic conductivity structures excited by horizontal electric dipole sources and the computed EM field components were horizontal electric and magnetic field components and the impedance derived from them. In this paper emphasis is put on the EM fields determination due to vertical electric dipole source placed in 2D surroundings which can be isotropic or anisotropic as well. The effect of anisotropy is investigated by many authors and one of the best summaries is given by [13].

2. 2.5D FEM PROBLEM FOR ISOTROPIC CASE WITH VERTICAL ELECTRIC DIPOLE SOURCE

In the frequency domain electromagnetic (FEM) methods $e^{j\omega t}$ time dependent source field is assumed and let x be parallel to the structural strike direction. The basic relationships governing the electromagnetic phenomenon are the Maxwell's equations. One of them expresses that electric fields are the results from the time-varying magnetic induction:

$$rot\vec{E} = -\partial\vec{B}/\partial t \tag{1}$$

$\vec{i}_s = Id\vec{s}\,\delta(\vec{r})$ describes a point source approximation which can be involved into the other Maxwell's equation:

$$rot\vec{H} = \vec{i} + \vec{i}_s \tag{2}$$

(2) Represents the fact that the magnetic fields are caused by conduction and source currents. In our situation conduction currents dominate over displacement currents due to the EM fields of low frequencies applied. For this reason the effect of displacement currents in (2) was not taken into account.

In the case of magnetic source [14] recommended that the solution of the original 3D problem could be replaced by the series of solutions of 2D problem in the k_x wavenumber domain. This procedure assumes that the Maxwell's equations (1) and (2) are Fourier-transformed. This transformation can be defined as:

$$\hat{F}(k_x, y, z) = \int_{-\infty}^{\infty} F(x, y, z)e^{-jk_x x}dx \tag{3}$$

In the course of the transformation the Fourier transform of the partial derivative of the EM field components with respect x is also required. It can be proved that the partial derivative of any EM field components with respect x is proportional to the Fourier transform of the component itself (see e.g. [6]).

Taking into account the harmonic time dependence of EM fields, we can rewrite the Fourier transforms of (1) Maxwell's equation in the following form:

$$\frac{\partial\hat{E}_z}{\partial y} - \frac{\partial\hat{E}_y}{\partial z} = -j\omega\mu\hat{H}_x \tag{4}$$

$$\frac{\partial\hat{E}_x}{\partial z} - jk_x\hat{E}_z = -j\omega\mu\hat{H}_y \tag{5}$$

$$jk_x\hat{E}_y - \frac{\partial\hat{E}_x}{\partial y} = -j\omega\mu\hat{H}_z \tag{6}$$

If we assume that only vertical electric dipole source is applied, the Fourier transforms of (2) can be written as:

$$\frac{\partial \hat{H}_z}{\partial y} - \frac{\partial \hat{H}_y}{\partial z} = \sigma\, \hat{E}_x \tag{7}$$

$$\frac{\partial \hat{H}_x}{\partial z} - jk_x \hat{H}_z = \sigma\, \hat{E}_y \tag{8}$$

$$jk_x \hat{H}_y - \frac{\partial \hat{H}_x}{\partial y} = \sigma\, \hat{E}_z + \hat{i}_{sz} \tag{9}$$

The goal of the next part is to provide partial differential equation systems with equations containing only strike direction EM field components in the spatial wavenumber (k_x) domain. The first equation (the pure one) belonging to the TM mode is (4). From equations (5) and (9) $\hat{H}_y$ can be determined and taking them to be equal we receive:

$$\sigma(1 - k_x^2/k^2)\hat{E}_z = -\frac{\partial \hat{H}_x}{\partial y} - \frac{k_x}{\omega\mu}\frac{\partial \hat{E}_x}{\partial z} - \hat{i}_{sz} \tag{10}$$

Where k denotes the complex wavenumber and $k^2 = -j\omega\mu\sigma$

From equations (6) and (8) $\hat{H}_z$ can be determined and taking them to be equal we obtain:

$$-\sigma(1 - k_x^2/k^2)\hat{E}_y = -\frac{\partial \hat{H}_x}{\partial z} + \frac{k_x}{\omega\mu}\frac{\partial \hat{E}_x}{\partial y} \tag{11}$$

The other group of equations represents the TE mode. Following the 2D MT analogy one equation belonging to this mode is (7).

The non-strike directional magnetic field components in the wavenumber domain can be determined similarly as the non-strike directional electric field components were done for the TM mode. From equations (6) and (8) $\hat{E}_y$ can be expressed and taking them to be equal we have:

$$-j\omega\mu(1 - k_x^2/k^2)\hat{H}_z = -\frac{\partial \hat{E}_x}{\partial y} + \frac{jk_x}{\sigma}\frac{\partial \hat{H}_x}{\partial z} \tag{12}$$

From equations (5) and (9) $\hat{E}_z$ can be expressed and taking them to be equal we get:

$$j\omega\mu(1 - k_x^2/k^2)\hat{H}_y = -\frac{\partial \hat{E}_x}{\partial z} - \frac{jk_x}{\sigma}\frac{\partial \hat{H}_x}{\partial y} - \frac{jk_x}{\sigma}\hat{i}_{sz} \tag{13}$$

Let us introduce $\zeta^E = i\omega\mu\,(1 - \frac{k_x^2}{k^2})$; $\xi = \left(k_x^2 - k^2\right)^{-1}$; $\upsilon^E = \sigma$, and substitute the value of $\hat{H}_y$ and $\hat{H}_z$ – from (13) and (12), respectively – into (7):

$$-\frac{\partial}{\partial y}\left(\frac{1}{\zeta^E}\frac{\partial \hat{E}_x}{\partial y}\right) - \frac{\partial}{\partial z}\left(\frac{1}{\zeta^E}\frac{\partial \hat{E}_x}{\partial z}\right) + jk_x\frac{\partial \xi}{\partial y}\frac{\partial \hat{H}_x}{\partial z} - jk_x\frac{\partial \xi}{\partial z}\frac{\partial \hat{H}_x}{\partial y} + \upsilon^E \hat{E}_x = jk_x\frac{\partial}{\partial z}\left(\xi\,\hat{i}_{sz}\right) \tag{14}$$

Let us introduce $\zeta^M = \sigma\,(1-\frac{k_x^2}{k^2})$; $\upsilon^M = i\omega\mu$, and substitute the value of $\hat{E}_y$ and $\hat{E}_z$ – from (11) and (10), respectively – into (4):

$$-\frac{\partial}{\partial y}\left(\frac{1}{\zeta^M}\frac{\partial \hat{H}_x}{\partial y}\right)-\frac{\partial}{\partial z}\left(\frac{1}{\zeta^M}\frac{\partial \hat{H}_x}{\partial z}\right)-jk_x\frac{\partial \xi}{\partial y}\frac{\partial \hat{E}_x}{\partial z}+jk_x\frac{\partial \xi}{\partial z}\frac{\partial \hat{E}_x}{\partial y}+\upsilon^M\hat{H}_x=\frac{\partial}{\partial y}\left(\frac{\hat{i}_{sz}}{\zeta^M}\right) \tag{15}$$

In contrast with 2D MT, the TE and TM mode cannot be treated separately, and the partial differential equation system consisting of (14) and (15) has to be solved. In the isotropic situation -governed by (14) and (15) - second order mixed partial derivatives of the strike directional Fourier EM field components cannot be found. Independent of the type of source there is no pure TM and TE mode, because the two polarizations are coupled for each source type (direction) case. Still this statement in the course of 2.5D modeling the case of electric dipole source of structural strike direction is called TE mode, and when the source term is perpendicular to the structural strike it is referred as TM mode [6–7]. The reason of this nomination is the following: in the case of electric dipole source parallel to the structural strike the current flow is mainly parallel to the strike, and for the situation when the source term is perpendicular to the structural strike there is a horizontal magnetic field component which coincides with the structural strike just like in 2D MT TM mode. There is a similarity between differential equations for 2.5D TM mode and the ones involving vertical dipole source in a 2D conductivity surrounding: in both cases the inhomogeneous terms of the equations are the partial derivatives of the applied current source with respect *y* or *z*, but in a changed order.

3. 2.5D FEM PROBLEM FOR ANISOTROPIC CASE WITH VERTICAL ELECTRIC DIPOLE SOURCE

The conductivity determining the relationship between the current density vector and the electric field vector is a scalar quantity only for an isotropic situation, in general case it is a tensor. The conductivity tensor has a simple form if two of the orthogonal coordinate directions are assumed to lie in the direction of maximum conductivity and the third one into the minimum conductivity value. In the case of layering the greatest resistivity can be observed perpendicularly to the layering. The same σ_t conductivity can be usually proposed in the *x* and *y* direction and σ_n value denotes the conductivity value in the *z* direction. The presence of anisotropy does not influence the Fourier transforms of (1) Maxwell's equation, these component equations (4)–(6) remain unchanged. Taking into account the anisotropy in the Fourier transforms of (2) instead of (7)–(9) we can write:

$$\frac{\partial \hat{H}_z}{\partial y}-\frac{\partial \hat{H}_y}{\partial z}=\sigma_t\hat{E}_x \tag{16}$$

$$\frac{\partial \hat{H}_x}{\partial z}-jk_x\hat{H}_z=\sigma_t\hat{E}_y \tag{17}$$

$$jk_x\hat{H}_y-\frac{\partial \hat{H}_x}{\partial y}=\sigma_n\hat{E}_z+\hat{i}_{sz} \tag{18}$$

The aim of the next derivation is the same as it was in isotropic case: to yield a partial differential equation system containing only strike direction EM field components and their partial derivatives with respect space in the wavenumber (k_x) domain besides distributed parameters and frequency. From equations (5) and (18) $\hat{H}_y$ can be determined and taking them to be equal we get:

$$\sigma_n(1-k_x^2/k_n^2)\hat{E}_z = -\frac{\partial \hat{H}_x}{\partial y} - \frac{k_x}{\omega\mu}\frac{\partial \hat{E}_x}{\partial z} - \hat{i}_{sz} \tag{19}$$

If we introduce

$$q_n = 1/(1-k_x^2/k_n^2) \tag{20}$$

and we use the resistivity instead of conductivity in (19)

$$\hat{E}_z = -\rho_n q_n \frac{\partial \hat{H}_x}{\partial y} - \frac{k_x \rho_n q_n}{\omega\mu}\frac{\partial \hat{E}_x}{\partial z} - \rho_n q_n \hat{i}_{sz} \tag{21}$$

From equations (6) and (17) $\hat{H}_z$ can be determined and taking them to be equal we get:

$$-\sigma_t(1-k_x^2/k_t^2)\hat{E}_y = -\frac{\partial \hat{H}_x}{\partial z} + \frac{k_x}{\omega\mu}\frac{\partial \hat{E}_x}{\partial y} \tag{22}$$

Introducing

$$q_t = 1/(1-k_x^2/k_t^2) \tag{23}$$

and using the resistivity instead of conductivity from (22)

$$\hat{E}_y = \rho_t q_t \frac{\partial \hat{H}_x}{\partial z} - \frac{k_x \rho_t q_t}{\omega\mu}\frac{\partial \hat{E}_x}{\partial y} \tag{24}$$

The vertical magnetic field components in the wavenumber domain can be determined similarly. From equations (6) and (17) $\hat{E}_y$ can be expressed and taking them to be equal we get:

$$-j\omega\mu(1-k_x^2/k_t^2)\hat{H}_z = -\frac{\partial \hat{E}_x}{\partial y} + \frac{jk_x}{\sigma_t}\frac{\partial \hat{H}_x}{\partial z} \tag{25}$$

From this equation $\hat{H}_z$ can be expressed as:

$$\hat{H}_z = -\frac{jq_t}{\omega\mu}\frac{\partial \hat{E}_x}{\partial y} - \frac{k_x \rho_t q_t}{\omega\mu}\frac{\partial \hat{H}_x}{\partial z} \tag{26}$$

The horizontal magnetic field component perpendicular to the strike can be determined in the following way: from equations (5) and (18) $\hat{E}_z$ can be expressed and taking them to be equal we obtain:

$$j\omega\mu(1-k_x^2/k_n^2)\hat{H}_y = -\frac{\partial \hat{E}_x}{\partial z} - \frac{jk_x}{\sigma_n}\frac{\partial \hat{H}_x}{\partial y} - \frac{jk_x}{\sigma_n}\hat{i}_{sz} \tag{27}$$

From this equation $\hat{H}_y$ can be expressed as:

$$\hat{H}_y = \frac{jq_n}{\omega\mu}\frac{\partial \hat{E}_x}{\partial z} - \frac{k_x \rho_n q_n}{\omega\mu}\frac{\partial \hat{H}_x}{\partial y} - \frac{k_x \rho_n q_n}{\omega\mu}\hat{i}_{sz} \tag{28}$$

In the knowledge of the non-strike directional EM field components in the wavenumber domain we can substitute them into the "pure" TE and TM components equations: substituting (26) and (28) into (16) we receive (29). The other equation will be (30) which can be derived by the substitution of (21) and (24) into (6):

$$\frac{j}{\omega\mu}\frac{\partial}{\partial y}\left(q_t \frac{\partial \hat{E}_x}{\partial y}\right) + \frac{k_x}{\omega\mu}\frac{\partial}{\partial y}\left(\rho_t q_t \frac{\partial \hat{H}_x}{\partial z}\right) + \frac{j}{\omega\mu}\frac{\partial}{\partial z}\left(q_n \frac{\partial \hat{E}_x}{\partial z}\right) - \frac{k_x}{\omega\mu}\frac{\partial}{\partial z}\left(\rho_n q_n \frac{\partial \hat{H}_x}{\partial y}\right) + \sigma_t \hat{E}_x = \frac{k_x}{\omega\mu}\frac{\partial}{\partial z}\left(\rho_n q_n \hat{i}_{sz}\right) \tag{29}$$

$$\frac{\partial}{\partial y}\left(\rho_n q_n \frac{\partial \hat{H}_x}{\partial y}\right) + \frac{k_x}{\omega\mu}\frac{\partial}{\partial y}\left(\rho_n q_n \frac{\partial \hat{E}_x}{\partial z}\right) + \frac{\partial}{\partial z}\left(\rho_t q_t \frac{\partial \hat{H}_x}{\partial z}\right) - \frac{k_x}{\omega\mu}\frac{\partial}{\partial z}\left(\rho_t q_t \frac{\partial \hat{E}_x}{\partial y}\right) - j\omega\mu\hat{H}_x = -\frac{\partial}{\partial y}\left(\rho_n q_n \hat{i}_{sz}\right) \tag{30}$$

Except the coefficient of the strike directional Fourier magnetic field component in (30) all coefficients reflect the effect of anisotropy, even the inhomogeneous terms do in equations of (29) and (30). In contrast with the isotropic situation second order mixed partial derivatives of the strike directional Fourier EM field components are in the anisotropic case. In order to obtain the finite difference form of (29) and (30) additional transformations are suggested. Instead of the term for the first mixed second order partial derivative of the strike directional Fourier magnetic field components in (29) it can be written as:

$$\frac{k_x}{\omega\mu}\frac{\partial}{\partial y}\left(\rho_t q_t \frac{\partial \hat{H}_x}{\partial z}\right) = \frac{k_x}{\omega\mu}\frac{\partial(\rho_t q_t)}{\partial y}\frac{\partial \hat{H}_x}{\partial z} + \frac{k_x \rho_t q_t}{\omega\mu}\frac{\partial^2 \hat{H}_x}{\partial y \partial z} \tag{31}$$

Similarly, for the second mixed second order partial derivative of the strike directional Fourier magnetic field components in (29):

$$\frac{k_x}{\omega\mu}\frac{\partial}{\partial z}\left(\rho_n q_n \frac{\partial \hat{H}_x}{\partial y}\right) = \frac{k_x}{\omega\mu}\frac{\partial(\rho_n q_n)}{\partial z}\frac{\partial \hat{H}_x}{\partial y} + \frac{k_x \rho_n q_n}{\omega\mu}\frac{\partial^2 \hat{H}_x}{\partial z \partial y} \tag{32}$$

Finally, instead of the mixed second order partial derivatives of the strike directional Fourier electric field component in (30):

$$\frac{k_x}{\omega\mu}\frac{\partial}{\partial y}\left(\rho_n q_n \frac{\partial \hat{E}_x}{\partial z}\right) = \frac{k_x}{\omega\mu}\frac{\partial(\rho_n q_n)}{\partial y}\frac{\partial \hat{E}_x}{\partial z} + \frac{k_x \rho_n q_n}{\omega\mu}\frac{\partial^2 \hat{E}_x}{\partial y \partial z} \tag{33}$$

$$\frac{k_x}{\omega\mu}\frac{\partial}{\partial z}\left(\rho_t q_t \frac{\partial \hat{E}_x}{\partial y}\right) = \frac{k_x}{\omega\mu}\frac{\partial(\rho_t q_t)}{\partial z}\frac{\partial \hat{E}_x}{\partial y} + \frac{k_x \rho_t q_t}{\omega\mu}\frac{\partial^2 \hat{E}_x}{\partial z \partial y} \tag{34}$$

4. FINITE DIFFERENCE FORMULATION

In order to forward model the EM response due to a 2D structure with finite difference (FD) method, the conductivity inhomogeneities and the homogeneous host have to be covered by a finite rectangular grid. The grid geometry has to be also fit to the conductivity boundaries, the positions of the source and the receivers. The physical parameters of (29)–(30) equations are constant within each rectangular grid element and these parameters are considered as distributed parameters. For the isotropic case there must be two input conductivity maps, one for the tangential, and the other one for the normal conductivity distribution. With the use of the transmission sheet analogy any part of the grid section with distributed parameters can be replaced by a grid section built up lumped circuit elements [14]. The coupled partial differential equations (29)–(30) are very similar to the equations of two coupled transmission sheets and this analogy makes it possible to fulfill the interior boundary conditions, because each grid point can be regarded as a branch point of circuit. In this way a five-point difference scheme could be applied for the FD forward modeling to the isotropic 2.5-D problem due to a dipole source. The second order partial derivatives with respect to *y* or *z* can be finite differenced similarly as in the case of isotropic situation [6] and [8]. However, for the anisotropic 2.5D problem – due to the mixed partial derivatives of strike directional Fourier EM field components in the partial differential equations of (29)–(30) – a nine point finite difference scheme can be suggested.

The linear variation of resistivity values between the centers of grid element is supposed. The derivatives of the EM Fourier components are approximated by their corresponding finite differences. In this way both terms of the right hand side of (31)–(34) can be finite differenced. The term of the second order mixed partial derivative can be approximated by finite differences if we take into account the field values in eight grid points surrounding the central node. All terms of the right hand side in (29)–(30) are the average values of the area being lumped. The vertical electric source is treated as a Heaviside function of space in the $x = 0$ plane. This source term is smeared within a rectangular grid element, like the horizontal electric dipole source perpendicular to the strike [6], which makes it possible to take its derivative with respect *y* and *z*. The derivatives of the source terms are taken across element boundaries and can be expressed in the terms of weighted delta functions. These derivatives are lumped over the line segment connecting the centre of the neighboring grid elements and these average values are referred to the two neighboring nodes on the element boundary. Because of this source treatment there are four grid points with non-zero source term. Instead of (29)–(30) the substituting resultant finite difference equations for the grid point containing the vertical dipole source term can be expressed in the following form:

$$\sum_{i=1}^{8}\left(\frac{\hat{E}_{ix}-\hat{E}_{0x}}{-A_i^E}+\frac{\hat{H}_{ix}-\hat{H}_{0x}}{B_i^E}\right)+C_0^E\hat{E}_{0x}=\hat{S}_{0z}^E \tag{35}$$

$$\sum_{i=1}^{8}\left(\frac{\hat{H}_{ix}-\hat{H}_{0x}}{-A_i^M}+\frac{\hat{E}_{ix}-\hat{E}_{0x}}{B_i^M}\right)+C_0^M\hat{H}_{0x}=\hat{S}_{0z}^M \tag{36}$$

here *0* stands for the central grid point and *i* denotes the surrounding eight grid points in the vicinity of the central node. A_i, B_i, C_0 stand for the coefficients derived from the nine point finite difference scheme and $\hat{S}_{0x}$ denote the finite difference source terms for the vertical dipole source in the wavenumber domain. Along the edge of the grid either plane wave or terminal impedance type boundary condition can be used. In the course of our isotropic modeling the terminal impedance type boundary condition was preferred.

The way of the solution to the linear equation system is one of the most important questions in the course of FD method. The block tridiagonal LU decomposition suggested by [14] and [15] for the solution of the linear equation system can be used only for the isotropic situation. This procedure takes into account the properties of coefficient matrix. In isotropic case only the two co-diagonal and the main diagonal blocks are non-zero matrices (with *4m*4m* real elements). For this reason instead of the inversion of the coefficient matrix (with *4mn*4mn* real elements, where *m* denotes the number of rows and *n* stands for the number of columns of the grid) the *n* times inversion of block matrices was done. In the anisotropic case there are non-zero matrix coefficients outside the three central blocks next to each other. It means that the block tridiagonal LU decomposition cannot be applied. At the same time LU decomposition of band matrix seems to be one of the promising solutions [16]. For the solution of banded great linear system parallel processing can be suggested.

5. INVERSE FOURIER TRANSFORMS TO OBTAIN SPATIAL SOLUTIONS

The general relationship resulting in space-domain solution from the wavenumber can be given as:

$$F(x,y,z)=\frac{1}{2\pi}\int_{-\infty}^{\infty}\hat{F}(k_x,y,z)e^{jk_x x}dk_x \tag{37}$$

For the plain containing the source and the vertical borehole (or any underground observation point) this relationship – where y_R denotes the y co-ordinate of the receiver – can be written as:

$$F(0,y_R,z)=\frac{1}{2\pi}\int_{-\infty}^{\infty}\hat{F}(k_x,y_R,z)dk_x \tag{38}$$

This equation can be directly applied to the spatial determination of strike-directional magnetic field component, because in the spatial wavenumber domain this component was given for any node of the grid as the solution of the linear equation system:

$$H_x(0,y_R,z)=\frac{1}{\pi}\int_{0}^{\infty}\hat{H}_x(k_x,y_R,z)\,dk_x \tag{39}$$

In the plane containing the source and perpendicular to the strike E_y and E_z can be measured, too. These components can be expressed from the component Maxwell's equations (4)–(9) with the assumption of no source term. As it can be seen the equation for the strike-directional magnetic field component does not contain conductivity anisotropy dependence as opposed to the non strike-directional electric field components. For the isotropic case let us introduce $q_R=1/(1-k_x^2/k_R^2)$, here R refers to the actual receiver position and taking into account (11):

$$E_y(0,y_R,z)=\frac{1}{\pi}\int_{0}^{\infty}\left[\ \rho_R q_R\frac{\partial\hat{H}_x}{\partial z}-\frac{k_x\rho_R q_R}{\omega\mu}\frac{\partial\hat{E}_x}{\partial y}\ \right]dk_x \tag{40}$$

In a vertical borehole if there is no conductivity anisotropy in the receiver site (R), then the vertical electric field can be expressed from (10):

$$E_z(0,y_R,z)=-\frac{1}{\pi}\int_{0}^{\infty}\left[\ \rho_R q_R\frac{\partial\hat{H}_x}{\partial y}+\frac{k_x\rho_R q_R}{\omega\mu}\frac{\partial\hat{E}_x}{\partial z}\ \right]dk_x \tag{41}$$

Similar equations can be derived for these two EM components if the receiver site can be characterized by conductivity anisotropy. These EM components can be expressed from the component Maxwell's equations (4)–(6) and (16)–(18) with the assumption of no inhomogeneous term in (18):

$$E_y(0, y_R, z) = \frac{1}{\pi}\int_0^{\infty}\left[\ \rho_{tR} q_{tR} \frac{\partial \hat{H}_x}{\partial z} - \frac{k_x \rho_{tR} q_{tR}}{\omega\mu} \frac{\partial \hat{E}_x}{\partial y}\ \right] dk_x \tag{42}$$

and that of the source term free version of (21):

$$E_z(0, y_R, z) = -\frac{1}{\pi}\int_0^{\infty}\left[\ \rho_{nR} q_{nR} \frac{\partial \hat{H}_x}{\partial y} + \frac{k_x \rho_{nR} q_{nR}}{\omega\mu} \frac{\partial \hat{E}_x}{\partial z}\ \right] dk_x \tag{43}$$

It can be seen that besides the partial derivatives of the strike-directional EM field components in spatial wavenumber domain, the electric field component perpendicular to the strike depends on the lateral, while the vertical electric field component depends on the normal conductivity value.

6. SOME ASPECTS OF GRID GEOMETRY AND SPATIAL WAVENUMBER PLANNING

Depending on the problem to be solved different conductivity distribution, transmitter-receiver arrays and measuring frequencies are assumed. The grid geometry with the conductivity distribution has to reflect the 2D conductivity structure to be investigated, and in the case of anisotropic case two conductivity maps will have to be provided for the same grid geometry within the input data set. The problems solved by TE and TM mode FEM soundings resulted in some experience [6]–[12], which is worth taking into account in anisotropic situation as well [17]. The computation of frequency sounding curves requires changing grid geometry in the course of FD modeling. For grid geometry planning 1D forward modeling results were considered as references.

Due to the stronger attenuation of high frequency EM fields grid with finer meshes covering smaller area of the investigated 2D structure can be applied. Because the attenuation depends on the conductivity as well, for this reason besides the highest frequency it is the greatest tangential conductivity of the section which determines the element of the finest grid geometry. It cannot be greater than *p/10*, where *p* denotes the skin depth for this region. The greatest grid area (with courser grid elements) can be planned by the value of the greatest EM wavelength. The distance between the inhomogeneity and the edge of the grid both in horizontal and vertical sense (downward) has to be at least 2–3 times greater than the skin depth. In the case of ground EM measurements (or shallow depth EM transillumination) the vertical grid extension for air has to exceed 1.5 times the transmitter-receiver distance. At least in the vicinity of the source and the receiver the use of equidistance grid sizes are suggested, and if it possible this grid geometry can be recommended between the whole transmitter-receiver separation as well. Outside from the inhomogeneity gradual increase of grid elements with a factor of 1,5 can be accepted. The 1D reference comparison can be also used to guess the frequency at which we change the grid to compute frequency sounding curves. It is obvious that the 2.5D EM responses determined at this frequency with the two grids must be the same within accuracy better than that of the measurement.

It follows from the essence of the procedure that the range and the distribution of the along-strike wavenumbers have to be planned, too. Instead of the upper limit of the integrals

of (39)–(43) it is sufficient to compute till a k_{xmax} value. We experienced that this maximum value depends on the minimal transmitter-receiver range, the highest frequency and the greatest conductivity in the region to be investigated. After $k_x = 0$ value – which corresponds to the EM plane wave case – logarithmically equidistant sampling can be suggested in the wavenumber domain. The number of along-strike wavenumbers for which the linear equation system has to be solved has to exceed 21. The inverse Fourier transforms are made numerically: the EM field components and their partial derivatives in (39)–(43) are approximated by second-order polynomial functions for each section of k_x (where one section is determined by three discrete k_x values, and the third k_x value of each section is the first k_x value of the next section).

7. CONCLUSIONS

It is well known that the effect of anisotropy has to be taken into account in the course of the geoelectric and electromagnetic exploration. In this paper the basic formalism was derived for 2D isotropic and anisotropic conductivity structures exited by vertical electric dipole source treated as a point source. The partial differential equations were derived for both cases in the wavenumber domain and a comparison was also made between the partial differential equation systems. For the solution of the resulting FD banded linear equation system LU decomposition of band matrix is suggested, because in contrast with isotropic case 9 point FD scheme is required in the anisotropic situation. The experience gained for isotropic 2.5D TE and TM mode can be taken into account in the course of the grid and the spatial wavenumber domain planning for the anisotropic case. To obtain the spatial solutions of EM field components the inverse Fourier equations were also presented. Some recommendations for their numerical evaluation of inverse Fourier transforms, for the planning of spatial wavenumber sampling and some aspects of grid geometry planning were also provided.

ACKNOWLEDGEMENT

This work was carried out as part of the TÁMOP-4.2.1.B-10/2/KONV-2010-0001 project in the framework of the New Hungarian Development Plan. The realization of this project was supported by the European Union and, co-financed by the European Social Fund.

NOMENCLATURE

A_i, B_i, C_0 coefficient matrix elements derived from the nine point FD scheme
$\vec{B}$ magnetic flux density (Wb/m^2)
$d\vec{s}$ elementary dipole length (m)
$\vec{E}$ electric field vector (V/m)
F EM component (V/m, or A/m)
$\hat{F}$ Fourier-transform of the F EM component (V/m, or A/m)
$\vec{H}$ magnetic field vector (A/m)
I transmitter current (A)
$\vec{i}$ current density vector (A/m^2)
$\vec{i}_s$ applied current source (A/m^2)
j $\sqrt{-1}$
k complex wavenumber (1/m)
k_x wavenumber in the strike direction (1/m)
p skin depth (m)

q_n derived dimensionless parameters (subscript *n* refers to normal)
q_t derived dimensionless parameters (subscript *t* refers to tangential)
r transmitter-receiver separation, distance (m)
t time (s)
$\delta(r)$ Dirac-delta function
ε dielectric constant (F/m)
ζ^E TE impedance ($Hm^{-1}s^{-1}$)
ζ^M TM impedance (S/m)
μ magnetic permeability (H/m)
υ^E TE admittance (S/m)
υ^M TM admittance ($Hm^{-1}s^{-1}$)
ξ derived parameter (m^2)
ρ resistivity (ohmm)
σ conductivity (mho/m or S/m)
ω angular frequency of the EM field (Hz)

REFERENCES

1. Takács, E.: *Geophysics, Geoelectrical exploration methods I., II.* (in Hungarian), Budapest, Tankönyvkiadó, 1981.
2. Nabighien, M. N.: "Electromagnetic methods in applied geophysics." Vol. 2, Application, Parts A and B, Tulsa, SEG, 1992.
3. Wait, J. R.: Geo-Electromagnetism. Academic Press, Inc., 1982.
4. Serra, O.–Serra, L.: *Well logging data acquisition and applications*. Serralog, 2004.
5. Takács, E.: "In-mine frequency sounding with a buried grounded dipole source." Geophysical Transactions,Vol. 34., No. 4., 1988, 343–359.
6. Pethő, G.: *FEM numerical modeling of 2D structures exited by electrical dipole source*. (in Hungarian, thesis for Candidate of Science degree), Miskolc, 1993.
7. Pethő, G.: "CSAMT Numerical Modelling for 2D Thermal EOR Monitoring." EAPG-6th Conference and Technical Exhibition Extended Abstracts of Papers, P547, Vienna, 1994.
8. Pethő, G.–Kaikkonen, P.–Vanyan, L., L.: "Numerical modelling for the effect of a 2-D seafloor trench on sea-bottom EM measurements using horizontal electric dipole sources." Geophysica, Vol. 31., 1995, 1–21.
9. Pethő, G.–Kaikkonen, P.–Vanyan, L., L.: "Frequency domain electromagnetic source polarization investigation in case of a 2-D seafloor trench." Aarhus, 3rd European Environmental and Engineering Geophysics Conference, Section New Developments, 1997, 323–326.
10. Pethő, G.–Ficsór, L.: "Distortion effect of elongated surface conductivity-inhomogeneities on CSAMT measurements." 14th Workshop on EM induction in the Earth, Book of Abstract, p. 100, Sinaia, 1998.
11. Pethő, G.–Ficsór, L.: "Source polarization effect in case of elongated surface inhomogeneities covering transition zone." Amsterdam, EAGE 63rd Conference & Technical exhibition, Abstract II, P050, 2001.
12. Pethő, G.: "FEM source effect investigation with 2.5D numerical modeling." 15th European Meeting of Environmental and Engineering Geophysics, Dublin, Near Surface Proceedings &Exhibitors'Cataloge, P59, 2009.

13. Negi, J.–G., Saraf, P., D.: "Anisotropy in geoelectromagnetism." Methods in geochemistry and geophysics, 28., Elsevier, 1989.
14. Stoyer, C.–H., Greenfield, R., J.: "Numerical solutions of the response of a two-dimensional earth to an oscillating magnetic dipole source." Geophysics, 41, 1976, 519–530.
15. Schechter, S.: "Quasi-tridiagonal matrices and type-insensitive difference equations." Quart. Appl. Math., 18, 3, 1960, 286–293.
16. Press, W., H.: "Numerical Recipes in Fortran 90." Cambridge University Press, 1996.
17. Pethő, G.: "Differential equations of FEM using electric dipole source for elongated structures with conductivity anisotropy." Kutatás és Innováció a Magyar Geotermiában, Miskolc, 2012, 70–86.

Geoscineces and Engineering, Vol. 2, No. 3 (2013), pp. 63–71.

EXPLANATION OF PRESSURE DEPENDENCE OF ACOUSTIC VELOCITY BASED ON THE CHANGE OF PORE VOLUME

JUDIT SOMOGYI MOLNÁR–MIHÁLY DOBRÓKA–TAMÁS BODOKY
Department of Geophysics
University of Miskolc

ABSTRACT

Pressure strongly influences the mechanical and transport properties of rocks, such as acoustic velocity, porosity, permeability and resistivity. Seismic and borehole logging techniques measure these rock properties in order to infer subsurface information. To relate changes in seismic attributes to reservoir conditions, a thorough understanding of pressure effects on rock properties is essential. Therefore it is important to develop a petrophysical model based on simple physical assumptions which describes the relationship between acoustic velocity and pressure. The suggested model is based on the idea that the pore volume of a rock is decreasing with increasing pressure. The model was applied to acoustic P wave velocity data sets including measurement data published in literature by Xu et al. and Toksöz et al. The model parameters were determined by inversion method. The inversion results proved that the proposed petrophysical model performs well in practice.

INTRODUCTION

Propagation characteristics of acoustic wave carry information of important mechanical properties of rocks hence the determination of velocity is a common task in studying rock parameters both in laboratory and in-situ. The velocity of acoustic waves propagating in different rocks under various confining pressure values [8], [12], [16] and also under different pore pressures [4], [6], [10], [18] were investigated by many researchers. The phenomenon that the observable wave velocity is increasing because of increasing pressure is well-known and was explained on various rock mechanical studies [3], [11], [18]. One of the most frequently used mechanisms for explaining the phenomenon is based on the change of pore volume under pressure [3].

General observation is that the velocity of acoustic wave propagating in rocks is in non-linear connection with the effective pressure [2], [18]. The pressure-acoustic velocity connection can be characterized best by exponential function [11], [14–15]. Several empirical models exist to describe the pressure dependence of longitudinal acoustic wave, but these models usually provide the determination of the parameters of a suitably chosen formula based on mathematical regression method remaining the physical meaning unexplained [7], [15]. To reasonably interpret laboratory measurements, a quantitative model – which provides the physical explanation – of the mechanism of pressure dependence is required which includes as few parameters as possible. In the paper a petrophysical model for the description of the pressure dependence of propagation velocity is presented.

MEASUREMENT OF ACOUSTIC WAVE VELOCITY

The pulse transmission technique was used for P wave velocity measurements [13]. The measurements required special measuring equipment (Figure 1) which was compiled at the Department of Geophysics (University of Miskolc). The pulse generator emitted a pulse to the piezoelectric transmitter crystal which started an acoustic wave in the sample. The receiver crystal transformed the acoustic sign to electric pulse which was amplified. Another

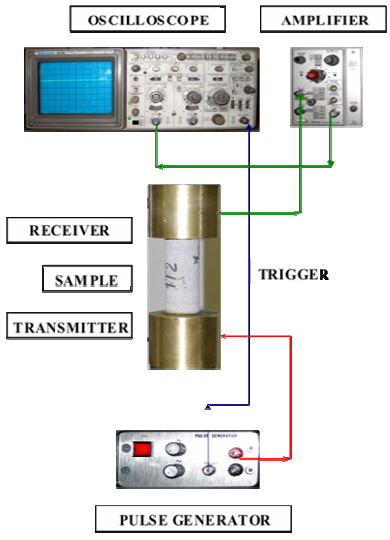

Figure 1. Measurement layout

pulse – the trigger – was emitted also by the pulse generator which synchronized the measurement system and the high-frequency digital oscilloscope which detected the arrival time of waves. In this way we can measure the propagation time of waves. Propagation velocity of acoustic waves can be determined by means of that of travel times and length of sample.

The Department performed wave velocity measurements on several sandstone samples originated from oil drilling wells. Two typical test results (fine-grained sandstones) are presented in the paper: Samples A and B. Rock samples subjected to uniaxial stress were analyzed by an electromechanical pressing device and wave velocities – as a function of pressure – were measured at adjoining pressures (up to ~15 MPa). The measured longitudinal velocity versus uniaxial pressure of the previously mentioned samples is shown in *Figure 2*. Measurement data indicate that the velocity increases first strongly nonlinearly with increasing pressure (because the quantity of pores are relatively high in this region) then in the higher pressure domain the increase in velocity (with increasing pressure) is moderate which can be attributed to the decrease of pore volume of rock sample, i.e. the pores are closing with pressure.

To confirm the reliability of the model independent data sets chosen from literature were processed as well. Xu et al. [17] and Toksöz et al. [13] also applied the pulse transmission

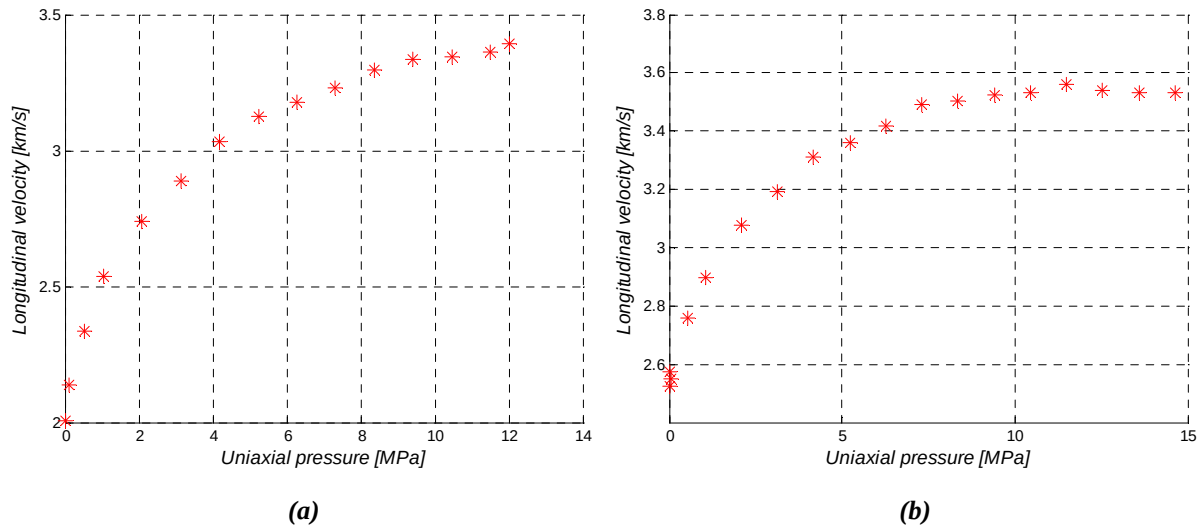

Figure 2.
Longitudinal velocity vs. uniaxial pressure of Sample A (a) and Sample B (b)

technique for velocity measurements. Each measurement was carried out at various pressures up to 70/35 MPa. The sample used by Xu et al. was low-porosity Lyons sandstone, a Permian aeolian deposit composed of mostly well-sorted quartz grains (90%) with less than 3% of clay. The Lyons sandstone is composed of rounded grains with a grain size of about 0.2 mm

and is well cemented. Toksöz et al. analyzed a Berea medium-grained sandstone sample which was composed of angular grains showing microcracks and the grain contacts were somewhat jagged and were weakly cemented. It had an average porosity of 16%, permeability of 75 mD, and a bulk density of 2,61 g/cm^3.

THE PRESSURE DEPENDENT VELOCITY MODEL

The response of rock to stress depends on its microstructure, constituent minerals and porosity, which is manifested in pressure dependence of velocity of elastic waves. Following Birch's [3] qualitative considerations we assume that the main factor determining the pressure dependence of propagation velocity is the closure of pores, i.e. decreasing of pore volume. Due to increasing pressure – from the unloaded state –, first the large pores are closed in the rock sample then after the slower compression process of smaller pores, all pores are closed. Therefore we introduce the parameter V as the pore volume (per unit volume) of a rock. The model is restricted only for uniaxial stress state and longitudinal acoustic waves.

If a stress increase $d\sigma$ is created in a rock let us assume - because of the closure of pores - that the change of pore volume dV is directly proportional to the applied stress increase $d\sigma$ and also the pore volume V. One can describe the two assumptions with the following differential equation

$$\mathrm{d}V = -\lambda_V V \, \mathrm{d}\sigma \ , \tag{1}$$

where λ_V is new (positive) material quality dependent petrophysical constant. The negative sign represents that with increasing stress the pore volume decreases.
The solution of Eq. (1) is

$$V = V_0 \exp\left(-\lambda_V \sigma\right) \ , \tag{2}$$

where V_0 is the pore volume at stress-free state ($\sigma = 0$). We assume also a linear relationship between the infinitesimal change of the propagation velocity dv – due to stress increase – and dV

$$\mathrm{d}v = -\alpha_V \, \mathrm{d}V \ , \tag{3}$$

where α_V is a proportionality factor. The negative sign represents that the velocity is increasing with decreasing pore volume. Combining this assumption with Eqs. (1–2) one can obtain

$$\mathrm{d}v = \alpha_V \lambda_V V_0 \exp(-\lambda_V \sigma) \, \mathrm{d}\sigma \tag{4}$$

and after integration

$$v = K - \alpha_V V_0 \exp(-\lambda_V \sigma) \ . \tag{5}$$

At stress-free state ($\sigma = 0$) the propagation velocity v_0 can be measured which is computed from Eq. (5) as $v_0 = K - \alpha_V V_0$. With this result and introducing the notation $\Delta v_0 = \alpha_V V_0$ Eq. (5) can be rewritten in the following form

$$v = v_0 + \Delta v_0 \left(1 - \exp(-\lambda_V \sigma)\right) \ . \tag{6}$$

Eq. (6) provides a theoretical connection between the propagation velocity and rock pressure. In the framework of the model, the velocity of acoustic wave increases from v_0 (at zero pressure) to $v_{max} = v_0 + \Delta v_0$ (at high pressure, when all the pores are closed). So, Δv_0 can be considered the velocity-drop caused by the presence of pores at zero pressure [7]. Note that in the range of high pressures, reaching a critical pressure [1] the reversible range is exceeded and destruction of the sample may occur and decreasing velocity can be observed.

This effect is outside of the author's present investigations. Therefore this model is valid only in the reversible range.

As it was mentioned λ_V is a new petrophysical constant, of which physical meaning is necessary to be given [5]. Introducing the notation $\Delta v = v_{max} - v$, (the velocity-drop caused by the presence of pores at pressure σ) Eq. (6) can be written in the form

$$\Delta v = \Delta v_0 \exp\left(-\lambda_V \sigma\right) . \tag{7}$$

Experiences denote that rocks show different velocity response to the same change in the rock pressure or in other words the velocity shows different sensitivity to pressure. It is interesting to see what amount of (relative) velocity change can be measured as a consequence of a certain (for example unit) change in the stress. For similar purpose, the sensitivity functions are extensively used in the seismic, geoelectric, electromagnetic and well-logging literature. Hence the author introduces the (logarithmic) stress sensitivity of the velocity-drop $\Delta v = v_{max} - v$ as

$$S(\sigma) = -\frac{1}{\Delta v}\frac{d\Delta v}{d\sigma} = -\frac{d\ln(\Delta v)}{d\sigma}. \tag{8}$$

Using Eq. (7) it can be seen that

$$\lambda_V = -\frac{d\ln(\Delta v)}{d\sigma} = S, \tag{9}$$

which shows that the petrophysical characteristic λ_V is the logarithmic stress sensitivity of the velocity-drop.

CASE STUDY

In order to prove the validity and practical applicability of the introduced petrophysical model, it was tested on longitudinal wave velocity data sets. The petrophysical constants (v_0, Δv_0, λ_V) appearing in the model equation (Eq. [6]) can be determined by processing measurement data based on the method of geophysical inversion. Linearized inversion method was used (principle of least squares method [9]). The inversion results for each sample can be seen in *Table 1*. The estimation errors – which are in parenthesis after each parameter – of the model parameters were calculated using the method given by Menke [9]. According to the method the elements of the main diagonal of covariance matrix in parameter space ($cov(m)$) provide the variances (σ_m) of model parameters, that means

$$\sigma_{m_i} = \sqrt{\mathrm{cov}(\mathbf{m})_{ii}} \tag{10}$$

gives the estimated error of the i-th model parameter (i = 1,2,3 in the given problem).

Table 1

Model parameters estimated by linearized inversion

Sample	v_0 (km/s)	Δv_0 (km/s)	λ_V (1/MPa)
A	2,09 (±0,0141)	1,29 (±0,0163)	0,3229 (±0,0146)
B	2,56 (±0,0072)	0,99 (±0,0086)	0,3467 (±0,0093)
Lyons (Xu et al. 2006)	3,75 (±0,0108)	1,03 (±0,0119)	0,0611 (±0,0031)
Berea (Toksöz et al. 1979)	3,32 (±0,0098)	0,82 (±0,0108)	0,1330 (±0,0068)

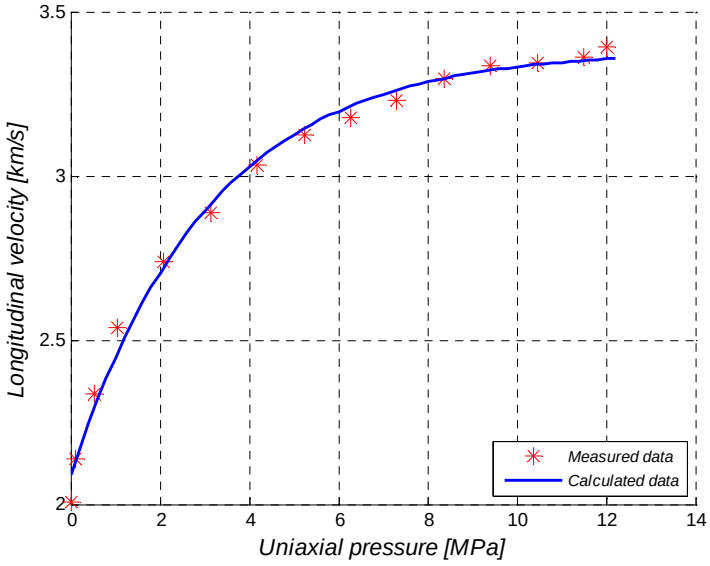

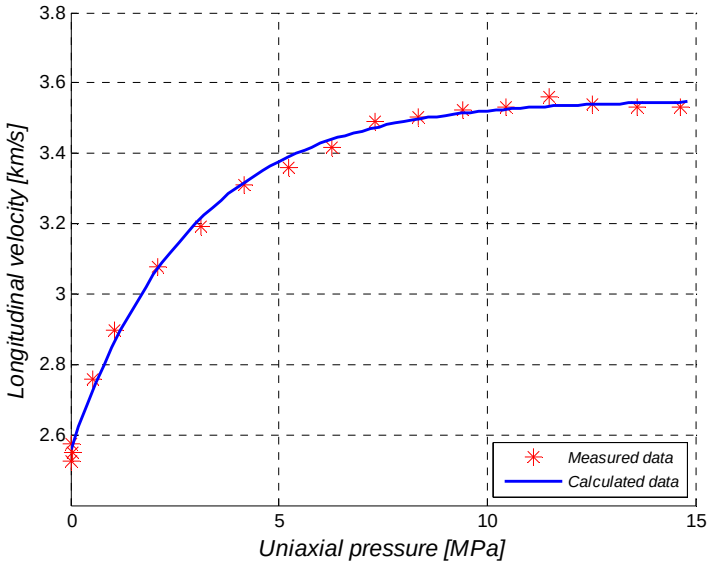

Figure 3.
Velocity-pressure function of sample A and B

With the estimated parameters, the velocities can be calculated at any pressure by substituting them into the model equation (Eq. [6]). The results are shown in *Figure 3–4*. The solid line shows the calculated velocity-pressure function while asterisk symbols represent the measured data. The figures show that the calculated curves are in good accordance with the measured data which proves that the petrophysical model applies well in practice. For the characterization of the accuracy of inversion estimates the author calculated the RMS (Root Mean Square) value according to the following formula [9]

$$D = \sqrt{\frac{1}{N}\sum_{k=1}^{N}\left(d_k^{(m)} - d_k^{(c)}\right)^2} \cdot 100\,[\%], \tag{11}$$

where $d_k^{(m)}$ is the measured velocity at the k-th pressure and $d_k^{(c)}$ is the k-th calculated velocity data which can be computed by Eq. (6). To characterize the reliability of the suggested petrophysical model the mean spread was also calculated by [9]

$$S = \sqrt{\frac{1}{M(M-1)} \sum_{i=1}^{M} \sum_{j=1}^{M} \left(\mathrm{corr}(\mathbf{m})_{ij} - \delta_{ij} \right)^2}, \tag{12}$$

where δ is a Kronecker-delta symbol (which equals 1 if i = j, otherwise 0), M is the number of model parameters and *corr(m)* is the correlation matrix. Table 2 contains the calculated RMS and mean spread values for each sample in the last iteration step.

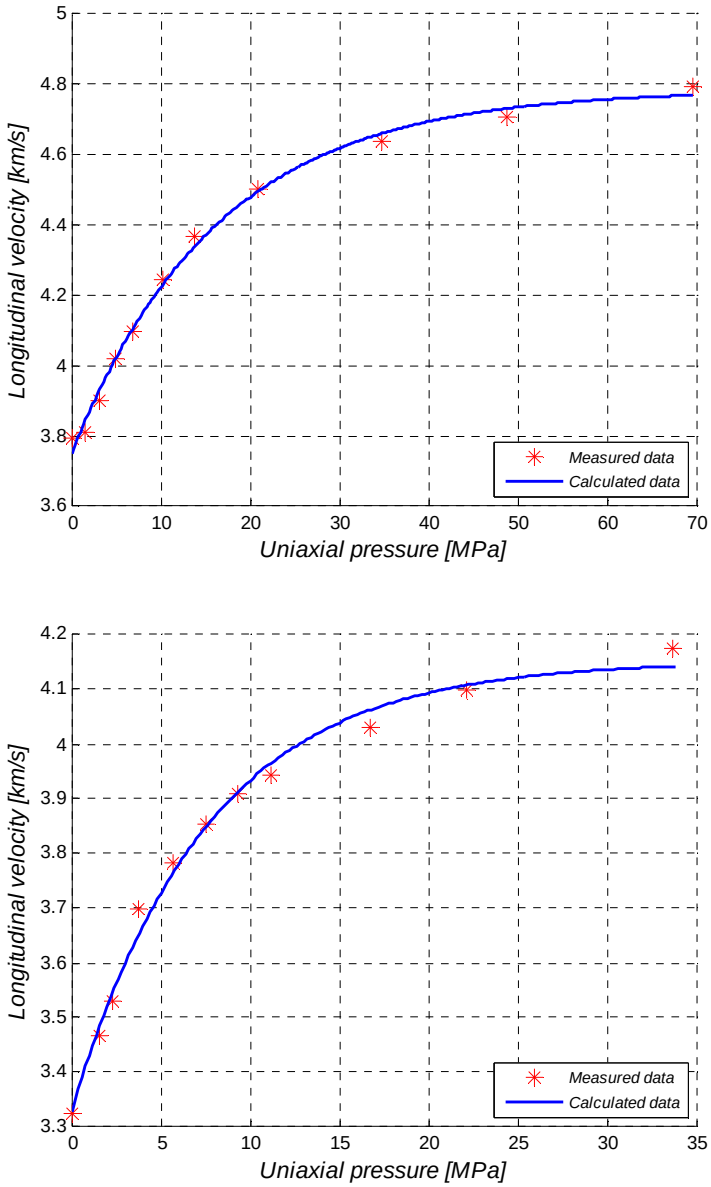

Figure 4.
Velocity-pressure function of Lyons and Berea sandstone samples

Table 2

Estimated RMS and mean spread values

Sample	D (%)	S
A	0,0369	0,4143
B	0,0209	0,4160
Lyons (Xu et al. 2006)	0,0247	0,4293
Berea (Toksöz et al. 1979)	0,0231	0,4433

It can be seen that the data misfits (RMS) were small (less than 1%), and the mean spread values indicate that the parameters are in moderate correlation, but the inversion results are still reliable. These results confirm the accuracy of the inversion estimates and the feasibility of the developed petrophysical model.

CONCLUSIONS

A new petrophysical model for describing the connection between the propagation velocity of acoustic wave and rock pressure was presented. The author found that the pressure dependence of acoustic velocity can be well described by a three-parameter exponential equation which gives also the physical explanation of pressure dependence: $v = v_0 + \Delta v_0 (1-\exp(-\lambda_V \sigma))$, where v_0 is the velocity at zero pressure, Δv_0 is the velocity drop caused by the presence of pores and λ_V is a new petrophysical parameter. The physical explanation of each parameter is clarified in the paper.

Acoustic velocity measurement data of four different rock samples (two of them were chosen from the literature) were used to confirm the reliability of the model. By means of inversion-based processing the model parameters were determined from measurement data, thus calculated data could be produced by using the petrophysical model. The calculated data matched accurately with measured data proving that the petrophysical model performs well in practice. Inversion results confirmed the accuracy and feasibility of the petrophysical model. The model was also applied on several sandstone samples (fine-, medium-, coarse-grained, pebbly, tuffy etc.) with success during the research.

ACKNOWLEDGEMENT

The described work was carried out as part of the TÁMOP-4.2.2/B-10/1-2010-0008 project in the framework of the New Hungary Development Plan. The realization of this project is supported by the European Union, co-financed by the European Social Fund.

LIST OF SYMBOLS

Symbol	Description	Unit
cov(m)	covariance matrix in parameter space	-
D	Root Mean Square (RMS)	%
$d_k^{(c)}$	calculated velocity at the k-th pressure value	km/s
$d_k^{(m)}$	measured velocity at the k-th pressure value	km/s
dv	change of propagation velocity	km/s
dV	change of pore volume (per unit volume)	-
dσ	stress increase	MPa
K	integration constant	-
M	number of model parameters	-

N	number of data	-
S	mean spread	-
$S(\sigma)$	stress sensitivity of velocity-drop	-
v	propagation velocity	km/s
V	pore volume (per unit volume)	-
v_0	propagation velocity at stress-free state	km/s
V_0	pore volume at stress-free state (per unit volume)	-
v_{max}	propagation velocity at maximum pressure	km/s
α_V	proportionality factor	-
δ	Kronecker-delta symbol	-
Δv	velocity-drop at pressure σ	km/s
Δv_0	velocity-drop	km/s
λ_V	new material quality dependent petrophysical constant	1/MPa
σ	stress	MPa
σ_{m_i}	estimated error of the i-th model parameter	-

REFERENCES

1. Anselmetti, F. S.–Eberli, G. P.: "Sonic velocity in carbonate sediments and rock." In: Palaz, I.–Marfurt, K. J. (Eds.): Carbonate Seismology: SEG Geophysical Developments Series, 1997, 6, 53–74.
2. Best, A. I.: "The effect of pressure on ultrasonic velocity and attenuation in near-surface sedimentary rocks." Geophysical Prospecting, 1997, 45, 345–364.
3. Birch, F.: "The velocity of compression waves in rocks to 10 kilobars, Part 1." Journal of Geophysics Research, 1960, 65, 1083–1102.
4. Darot, M.–Reuschlé, T.: "Acoustic wave velocity and permeability evolution during pressure cycles on a thermally cracked granite." International Journal of Rock Mechanics and Mining Sciences, 2000, 37, 1019–1026.
5. Dobróka, M.–Somogyi Molnár, J.: "New petrophysical model describing the pressure dependence of seismic velocity." Acta Geophysica, 2012, 60(2), 371–383.
6. He, T.–Schmitt, D. R.: "Velocity measurements of conglomerates and pressure sensitivity analysis of AVA response." Proceedings of the 76th SEG International Exposition and Annual Meeting, New Orleans, USA, 2006, 1–6 Oct.
7. Ji, S.–Wang, Q.–Marcotte, D.–Salisbury, M. H.–Xu, Z.: "P wave velocities, anisotropy and hysteresis in ultrahigh-pressure metamorphic rocks as a function of confining pressure." Journal of Geophysical Research, 2007, 112, B09204.
8. King, M. S.: "Recent developments in seismic rock physics." International Journal of Rock Mechanics and Mining Sciences, 2009, 46, 1341–1348.
9. Menke, W.: *Geophysical data analysis – Discrete inverse theory.* Academic Press, Inc. London Ltd., 1984.
10. Nur, A.–Simmons, G.: "The effect of saturation on velocity in low porosity rocks." Earth and Planetary Science Letters, 1969, 7, 183–193.
11. Singh, R.–Rai, C.–Sondergeld, C.: "Pressure dependence of elastic wave velocities in sandstones." Proceedings of the 76th International Exposition and Annual Meeting, SEG, 2006, 1883–1887.
12. Stacey, T. R.: "Seismic assessment of rock masses." Symp. on Exploration for Rock Engineering, Johannesburg, 1976, 2, 113–117.
13. Toksöz, M. N.–Johnston, D. H.–Timur, A.: "Attenuation of seismic waves in dry and saturated rocks, I. Laboratory measurements." Geophysics, 1979, 44(4), 681–690.
14. Wang, Q.–Ji, S. C.–Salisbury, M. H.–Xia, M. B.–Pan, B.–Xu, Z. Q.: "Shear wave properties and Poisson's ratios of ultrahigh-pressure metamorphic rocks from the Dabie-Sulu orogenic belt: Implications for the crustal composition." Journal of Geophysical Research, 2005, 110, B08208.

15. Wepfer, W. W.–Christensen, N. I.: "A seismic velocity-confining pressure relation, with applications." International Journal of Rock Mechanics and Mining Science, 1991, 28, 451–456.
16. Wyllie, M. R. J.–Gregory, A. R.–Gardner, G. H. F.: "An experimental investigation of factors affecting elastic wave velocities in porous media." Geophysics, 1958, 23(3), 459–493.
17. Xu, X.–Hofmann, R.–Batzle, M.–Tshering, T.: "Influence of pore pressure on velocity in low-porosity sandstone: Implications for time-lapse feasibility and pore-pressure study." Geophysical Prospecting, 2006, 54, 565–573.
18. Yu, G.–Vozoff, K.–Durney, D. W.: "The influence of confining pressure and water saturation on dynamic elastic properties of some Permian coals." Geophysics, 1993, 58(1), 30–38.

Geosciences and Engineering, Vol. 2, No. 3 (2013), pp. 73–81.

NEW INVERSION TECHNIQUES FOR THE ELIMINATION OF TRIGGER ERRORS IN SEISMIC REFRACTION DATA

ANIKÓ NOÉMI PARIPÁS–TAMÁS ORMOS
Department of Geophysics
University of Miskolc

ABSTRACT

At the interpretation of near surface seismic refraction measurements trigger time errors may cause serious difficulties. The paper investigates the trigger problem on synthetic datasets by two newly developed inversion methods. We solve the problem by using traveltime differences in the inversions instead of normal traveltime datasets. The results of the inversions are presented and compared to each other and also to that of the general traveltime refraction inversion. The comparison reveals the advantages and usability of the new methods in the evaluation of datasets containing trigger or random errors.

1. INTRODUCTION

In a seismic field measurement the measured data are the traveltime data of the artificially generated propagating waves [1]. Measuring with a seismic data acquisition system in which the exact position of the wave source and the geophones are known, the parameters of the studied geological structure can be determined – from the surface.

Though even with the most attentive preparation work, it is very hard to determine precisely the exact time of the wave generation, i.e. the trigger time. Various source types can be applied during a surface refraction measurement (and various ways can be used to measure the trigger time, however only with some errors). Using an explosion for wave generation an approximately 1–4 ms trigger error can occur due to the error of the geophysical blasting cap. Generating the waves with weight dropping or hammer strike, a piezoelectric ceramic or a geophone serves the trigger signal – cycle skipping can occur.

If we interpret a dataset with trigger errors, it can cause problems in the estimation of parameters. Trigger error can be considered as a case where the exact wave generation time is unknown. In this consideration the same problem has to be solved in seismic as in seismology; however the methods are different [2]. The inaccurate trigger time mainly causes problems in shallow exploration of geological structures (seismic refraction methods) as the accuracy of the trigger time has greater importance there than at the deeper explorations. The shorter the traveltime the greater the relative trigger error is. The same problem was examined earlier in terms of VSP measurements in a coal mine and the trigger error was eliminated by using three-component VSP devices measuring traveltime differences between the upper and lower geophone-triplets [3].

One method was described and its field application was also proved for eliminating trigger errors in the inversion of refracted first breaks by Ormos and Paripás [4]. In that method the idea of double-trace data was applied for refraction traveltime data. The concept had been developed by Dobróka et al. [5] for tomographic (conjugate gradient and SIRT) interpretation. In this paper two new inversion methods are suggested, examined and compared to each other using synthetic data, and the differences between them are presented.

2. THE SEISMIC REFRACTION FORWARD PROBLEM

The refraction forward problem means the calculation of the traveltime of first breaks above a geological structure with known physical parameters [6]. We can do it by knowing the measured traveltime curves and their theoretical description. In a media homogenous layer by layer, the traveltime curves are composed of the same number of curve slices as the number of layers found in the studied structure. In the followings the geological structure is assumed to be one-dimensional – meaning that the layers are homogenous and isotropic (the propagation velocities are constant inside one layer).

Solving the forward problem it is assumed that the near surface structure is composed of layers and the propagation velocities sharply change on layer boundaries. The traveltime curve detected by one geophone consists of the traveltime of the direct wave (Eq. 1) and the traveltime of the refracted wave. The latter one depends on the number of layers in the structure; the equation is drawn for two-layered (Eq. 2) and n-layered (Eq. 3) cases.

$$t^{(direct)} = \frac{x}{v_1} \tag{1}$$

$$t^{(refracted,2)} = \frac{2h_1 \cos i_{1,2}}{v_1} + \frac{x}{v_2} \tag{2}$$

$$t^{(refracted,n)} = \sum_{j=1}^{n-1} \frac{2h_j \cos i_{j,n}}{v_j} + \frac{x}{v_n} \tag{3}$$

In the equations x means the distance of the source and the geophone along the section, v_j means the propagation velocity of the wave in the j-th layer, h_j means the layer thickness of the j-th layer and $i_{1,2}$ means the critical angle of incidence (Eq. 4). If the wave reaches the layer boundary in this angle, refracted waves are generated and propagate along the layer boundary [6].

$$i_{1,2} = \arcsin \frac{v_1}{v_2} \tag{4}$$

The solution of the forward problem lies in the solution of Eq. 1–3. In a synthetic case the geological model and its physical parameters are known, therefore traveltime data can be calculated for each geophone.

Generally geophysical problems cannot be solved as forward problems because the parameters of the examined geological model are unknown and are to be determined. Therefore a so-called inverse problem has to be solved in which the problem is managed as an already solved problem – parameters are calculated on an initial model and these calculated parameters are compared to the measured ones in an optimizing or inversion procedure.

3. IMPLEMENTATION OF TRAVELTIME DIFFERENCES INTO THE INVERSE THEORY

At the evaluation of a dataset with trigger errors, interpretation problems may occur. In *Figure 1* traveltime curves are presented “measured” above the same geological structure – exact dataset without trigger error and a dataset with trigger errors. The inversion results of simple traveltime inversion and traveltime difference inversion are also shown.

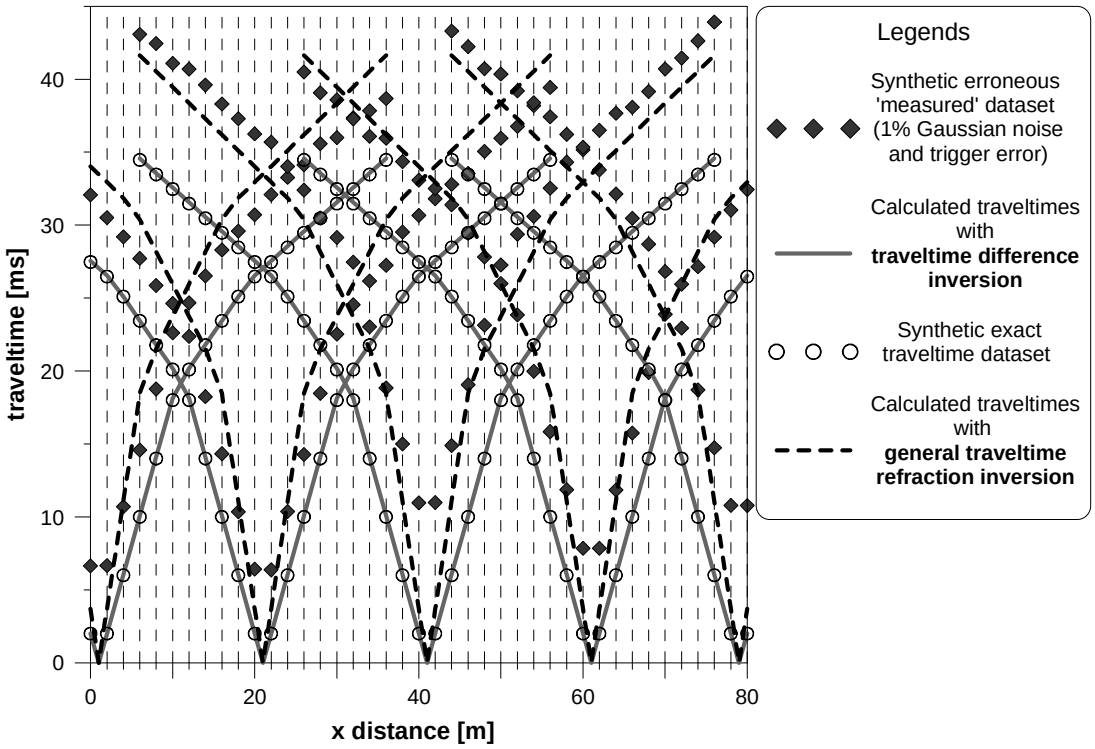

Figure 1.
The representation of the evaluation problem of a traveltime dataset contaminated with trigger errors for a 3-layered 1D structure

In case of trigger errors all traveltime data related to the same source point have the same amount of trigger error – therefore a certain value of time shift can be noticed on the traveltime curves. In this paper, for the elimination of trigger errors the "double-trace data" idea of Dobróka et al [5] is applied, according to which traveltime differences are used in the inversion process instead of the general traveltime dataset. For that a certain receiver is chosen as a reference and from all the other traveltime data related to the same source point traveltime differences ($\Delta t_{k,s}^{(meas)}$) are calculated (Eq. 5).

$$\Delta t_{k,s}^{(meas)} = t_{k,s}^{(meas)} - t_{r,s}^{(meas)} \tag{5}$$

In Eq. 5 $t_{k,s}^{(meas)}$ means the measured traveltime data of the elastic wave generated in the s-th source point and received by the k-th receiver; $t_{r,s}^{(meas)}$ means the measured traveltime data detected by the reference geophone. Traveltime difference dataset is generated from the measured dataset and in the evaluation procedure the inverse problem can be solved in several ways. The solution of the inverse problem is based on the solution of the forward problem and on the type of the inversion technique.

3.1. General traveltime refraction inversion

In this paper the damped least squares (DLSQ) inversion method is used where the complex problem is reduced to a linear equation system that has to be solved. Firstly the general seismic refraction inversion is presented that applies simple traveltime data in the inversion procedure. In case of a seismic refraction problem the linearized algorithm can be described with Eq.6, where t_k means the registered traveltime datum on the k-th geophone and G_{ki} means the Jacobi's matrix consisting of the partial derivatives of traveltime data.

$$t_k = \sum_{i=1}^{M} G_{ki} m_i \tag{6}$$

The e_k difference vector of the measured and calculated dataset has to be determined, and for the solution of the inverse problem the goal is its minimization (Eq. 7):

$$e_k = t_k^{(meas)} - t_k^{(calc)} = t_k^{(meas)} - \sum_{i=1}^{M} G_{ki} m_i \,. \tag{7}$$

As the inverse problem is solved with the DLSQ, the solution is given with the minimization of e_k vector-square – as seen in Eq. 8 –, where **m** means the model vector, $\mathbf{t}^{(meas)}$ means the measured traveltime data, **G** means the Jacobi's matrix of the partial derivatives of the traveltime data and **I** is an identity matrix multiplied by the scalar damping factor ε^2.

$$\mathbf{m} = \left(\mathbf{G}^T\mathbf{G} + \varepsilon^2\mathbf{I}\right)^{-1}\mathbf{G}^T\mathbf{t}^{(meas)} \tag{8}$$

3.2. Exact traveltime difference algorithm

After defining the general refraction inversion method, the mathematically exact traveltime difference method, named as the "exact traveltime difference algorithm" is presented [4]. In this case the traveltime registered by the so-called "reference geophone" can be given as seen in Eq. 9, where t_r means the traveltime detected by the reference geophone and G_{ri} means the associated Jacobi's matrix elements.

$$t_r = \sum G_{ri} m_i \,, \tag{9}$$

The calculated traveltime difference can be defined as the difference of Eq. 6 and 9 (Eq. 10).

$$\Delta t_k^{(calc)} = t_k - t_r = \sum_{i=1}^{M} \left(G_{ki} - G_{ri}\right) m_i \tag{10}$$

In this algorithm the vector to be minimized is determined in Eq. 11 applying traveltime difference data:

$$e_k = \Delta t_k^{(meas)} - \Delta t_k^{(calc)} = \Delta t_k^{(meas)} - \sum_{i=1}^{M} \left(G_{ki} - G_{ri}\right) m_i \tag{11}$$

Solving the inverse problem the substitution of $J_{ki} = G_{ki} - G_{ri}$ is necessary and then the solution can be given as in Eq. 12, where $\Delta\mathbf{t}^{(meas)}$ indicates the measured traveltime difference data, **J** means the difference Jacobi's matrix of the partial derivatives of general traveltime data.

$$\mathbf{m} = \left(\mathbf{J}^T\mathbf{J} + \varepsilon^2\mathbf{I}\right)^{-1}\mathbf{J}^T\Delta\mathbf{t}^{(meas)} \tag{12}$$

3.3. Iterative traveltime difference algorithm

The third inversion method presented is the so-called "iterative traveltime difference algorithm" for which traveltime difference dataset has to be determined from the measured dataset using the traveltime data of the reference geophones. In the second step reference traveltime data have to be calculated on the initial model and thirdly a new approximate measured dataset is created adding together the measured traveltime difference dataset and the initial reference data. In the followings the approximate measured traveltime dataset is used in the inversion procedure and the calculated travetime dataset is compared to that in an

inside inversion cycle. After a number of inside iterations a new "approximate measured" dataset is calculated using the new model and the next outside iteration follows.

The advantage of this method is that there is no necessity to write a new code as the method works with general traveltime dataset in the inversion phase. The solution of the inverse problem comes as Eq. 8. In this case the measured dataset changes from iteration to iteration, therefore the relative data distance has less meaning as it is calculated from the "approximate measured" dataset.

4. COMPARISON OF THE THREE REFRACTION INVERSION METHODS

For the evaluation of the results the well-known measure of the relative distance in data space (Eq. 13) was applied; but as the "measured" data are highly erroneous, this value is slightly reliable and can be also misleading. Instead of that in this case the quality of the inversion results can be described by the relative distance in model space (Eq. 14), where S means the number of sources, M means the number of model parameters, m_i means the i-th model parameter. This value is more usable for evaluating the results compared to the data distance in this type of theoretical examinations.

$$Dd = \sqrt{\frac{1}{N}\sum_{k=1}^{N}\left(\frac{t_k^{(meas)} - t_k^{(calc)}}{t_k^{(calc)}}\right)^2} \tag{13}$$

$$dm = \sqrt{\frac{1}{S}\frac{1}{(2M-1)}\sum_{s=1}^{S}\sum_{i=1}^{2M-1}\left(\frac{m_i(x_s)^{(exact)} - m_i(x_s)^{(estim)}}{m_i(x_s)^{(exact)}}\right)^2} \tag{14}$$

It has to be mentioned that as the iterative refraction inversion method calculates with approximate measured data, the measure of data distance is even more misleading than in the case of the other two methods.

4.1. The impact of trigger time on the inversion results

For the investigation of the impact of trigger time value, three datasets were created on which the inversion procedures were tested. To all synthetic datasets 1% error of Gaussian distribution and trigger errors were added; however the measure of the error in trigger time differs in each dataset. Dataset A1 contains no trigger error, dataset B1 contains 0.5–2 ms of trigger error and dataset C1 contains 3–8 ms of trigger error. The initial model has a model distance of 32% and the exact model was chosen to be the same for all the inversion procedures (3-layered 1D model). All three datasets were evaluated with all three inversion methods, the results can be seen in *Table 1.* Values of *Ddi* mean the data distance of the initial dataset from the dataset calculated on the exact model.

Table 1

Inversion results studying the impact of trigger error on different refraction inversion methods

1% error of Gaussian distribution	General traveltime inversion	Exact traveltime difference inversion	Iterative traveltime difference inversion
Dataset A1	Dd = 0.9%	Dd = 1.0%	Dd = 2.6%
Ddi = 0.9%	**Dm = 0.8%**	**Dm = 1.0%**	**Dm = 0.8%**
Dataset B1	Dd = 14.0%	Dd = 20.0%	Dd = 2.6%
Ddi = 20.5%	**Dm = 6.0%**	**Dm = 1.0%**	**Dm = 0.8%**
Dataset C1	Dd = 40.1%	Dd = 102.1%	Dd = 2.6%
Ddi = 103.1%	**Dm = 28.5%**	**Dm = 1.0%**	**Dm = 0.8%**

Examining the results several conclusions can be drawn. The most important one is that if you want to evaluate a measured traveltime dataset that contains trigger error with a general traveltime inversion method the result will be a model different from the exact one. A 3-8 ms of trigger error and an approximately 1% error of Gaussian distribution can cause a data distance of 100% as initial and even in a 3-layered 1D case as a result Dd = 40% data distance and more importantly dm = 28% model distance was reached. But if the inversion procedure was fulfilled with traveltime differences, the model distance was around 1% – using any of the two traveltime difference applying methods. (Another conclusion is that it can be misleading in evaluating field datasets to rely on the value of data distance, because if the dataset contains trigger errors, the application of traveltime difference inversion is proposed instead of the general method.)

4.2. The impact of random errors on the inversion results

Besides the impact of trigger error, the impact of random error is also studied in this paper to define the stability and reliability of the new traveltime difference methods. In this case – similarly to the previous one – three datasets were created but here the measure of trigger error was the same (0.5–2 ms) and the value of random error of Gaussian distribution was different. Dataset B1 contains 1%, B2 contains 2% and B5 contains 5% random error of Gaussian distribution. The other conditions of the inversion procedures were set the same in all cases.

According to the inversion results of *Table 2* it can be stated that the iterative traveltime difference inversion method is the less sensitive to random errors, although the results show a relatively high model distance. If the value of random error is at least 2%, the model distance of the results will be higher than that. The results of the exact traveltime difference inversion method show that it is a stable and fast method but sensitive to incidental noise in the dataset and in these cases the iterative, relatively slower method gives more precise and more reliable results.

The above presented methods were also tested on field dataset besides synthetic ones. The results can be seen in [4] and [7].

Table 2

Inversion results studying the impact of random error of Gaussian distribution on different refraction inversion methods

0.5-2 ms trigger error	**General traveltime inversion**	**Exact traveltime difference inversion**	**Iterative traveltime difference inversion**
Dataset B1	Dd = 14.0%	Dd = 20.0%	Dd = 2.6%
Ddi = 20.5%	**Dm = 6.0%**	**Dm = 1.0%**	**Dm = 0.8%**
Dataset B2	Dd = 13.8%	Dd = 20.4%	Dd = 7.5%
Ddi = 21.0%	**Dm = 6.9%**	**Dm = 3.8%**	**Dm = 4.4%**
Dataset B5	Dd = 14.2%	Dd = 28.4%	Dd = 21.5%
Ddi = 21.3%	**Dm = 27.1%**	**Dm = 44.9%**	**Dm = 27.7%**

5. CONCLUSIONS

In this paper the theoretical backgrounds were presented for the fact that trigger time definition has a great importance in shallow seismic refraction measurements and interpretation. Numerous inversion methods were developed for solving the trigger problem, however their usability and reliability differ from each other. The above described "exact traveltime difference refraction inversion" is a relatively fast algorithm that is highly usable for datasets with trigger error and small random error. But if the value of random error is higher, its stability reduces. The so-called "iterative traveltime difference method" was proved to be more effective for datasets with higher random error, although its convergence is slower due to its inside and outside iteration cycles. Both traveltime difference refraction inversion methods gave us better results compared to the general traveltime refraction inversion. The reliability of their results was significantly better than that of the measured data and even better than the results of the general traveltime inversion. Assuming 0.5–2 ms – or even 3–8 ms – of trigger error in the synthetic case the effects of the inaccurate source time disappeared. The results prove the usability of the new inversion method even in case of in-line offset sources.

According to our studies the iterative method was proved to be useable for the evaluation of datasets that contain trigger error. As this algorithm differs only slightly from the general solution, it can be implemented into the series expansion based refraction inversion method developed in the Department of Geophysics (University of Miskolc) [1], [8–9]. With this combined algorithm, 2D laterally changing geological structures would be evaluated easily even on datasets containing trigger error.

ACKNOWLEDGEMENTS

The described work was carried out as part of two TÁMOP projects in the framework of the New Hungary Development Plan. Paripás is grateful for the support of the TÁMOP-4.2.2/B–10/1–2010–0008 project and Ormos is thankful for the support of the TÁMOP-4.2.2.A–11/1/KONV–2012–0005 project. The realization of these projects is supported by the European Union, co-financed by the European Social Fund. The authors also would like to thank professor Dobróka for the topic and the theoretical background.

LIST OF SYMBOLS

Dd	relative distance in data space	(-)
Ddi	data distance of the initial dataset from the dataset calculated on the exact model	(-)
dm	relative distance in model space	(-)
$\mathbf{e}_k$	difference vector of the measured and calculated datasets	(s)
ε	scalar damping factor	(-)
G_{ki}	Jacobi's matrix elements of partial derivatives of k-th traveltime and i-th model parameter	(1/m, s/m)
G_{ri}	Jacobi's matrix elements of partial derivatives of traveltime detected on the reference geophone and i-th model parameter	(1/m, s/m)
$\mathbf{G}$, $\mathbf{G}^T$	Jacobi's matrix, and transposed Jacobi's matrix	(1/m, s/m)
h_1, h_j	thicknesses of the layers	(m)
$\mathbf{I}$	identity matrix	(-)
$i_{1,2}$, $i_{j,n}$	critical angel of incidence	(rad)
J_{ki}	difference Jacobi's matrix	(1/m, s/m)
$\mathbf{J}$, $\mathbf{J}^T$	difference Jacobi's matrix, and transposed difference Jacobi's matrix	(1/m, s/m)
M	number of model parameters	(-)
m_i	i-th model parameter	(m/s, m)
$\mathbf{m}$	vector of model parameters	(m/s, m)
N	number of measured data	(-)
S	number of sources along the profile	(-)
$t^{(direct)}$	travel time of direct wave	(s)
$t^{(refracted,2)}$	travel time on the 2nd layer refracted wave	(s)
$t^{(refracted,n)}$	travel time on the n-th layer refracted wave	(s)
$t_{k,s}$	traveltime of waves generated in the s-th source and received by the k-th receiver	(s)
$\Delta t_{k,s}$	traveltime difference of waves generated in the s-th source and received by the k-th and by the reference receivers	(s)
Δt_k	traveltime difference of waves received by the k-th and by the reference geophones	(s)
$\Delta t_k^{(meas)}$, $\Delta t_k^{(calc)}$	measured and calculated traveltime difference of waves received by the k-th and by the reference geophones	(s)
t_k	travel time of waves received by the k-th receiver	(s)
$t_k^{(meas)}$, $t_k^{(calc)}$	measured and calculated travel times of waves received by the k-th receiver	(s)
t_r	traveltime of waves received by the reference geophone	(s)
$t_{r,s}$	traveltime of waves generated in the s-th source and received by the reference geophone	(s)
x	distance of geophones along the section	(m)
x_s	distance of sources along the section	(m)
v_1, v_2, v_j, v_n	propagation velocities of waves in the layers	(m/s)

REFERENCES

1. Paripás, A. N.–Ormos, T.: "Resolution and ambiguity studies for a series expansion based multilayer refraction inversion method." Acta Geodaetica et Geophysica Hungarica, 47(2), 2012, 197–209.
2. Martino, S.–Scarascia Mugnozza, G.: "The role of the seismic trigger in the Calitri landslide (Italy): historical reconstruction and dynamic analysis." Soil Dynamics and Earthquake Engineering, 25, 2005, 933–950.
3. Breitzke, M.–Dresen, L.–Csókás, J.–Gyulai, Á.–Ormos, T.: "Parameter estimation and fault detection by three-component seismic and geoelectrical surveys in a coal mine." Geophysical Prospecting, 35, 1987, 832–863.
4. Ormos, T.–Paripás, A. N.: "Traveltime differences in seismic refraction inversion." Geosciences and Engineering, 1(2), 2012, 123–128.
5. Dobróka, M.–Dresen, L.–Gelbke, C.–Rüter, H.: "Tomographic inversion of normalized data: double-trace tomography algorithms." Geophysical Prospecting, 40, 1992, 1–14.
6. Ormos, T.: *The solution of the refraction inverse problem.* (In Hungarian) Departmental Manual. University of Miskolc, Department of Geophysics, 2011, 52. p.
7. Paripás, A. N.–Somogyi Molnár, J.–Ormos, T.–Pethő, G.: "Inversion of refracted first breaks using traveltime differences." Near Surface Geoscience, Extended Abstracts, P50, 2012, 1–5.
8. Dobróka, M.: *On the absorption-dispersion of Love waves propagating in inhomogeneous seismic waveguide of varying thickness; the inversion of absorption-dispersion properties.* (in Hungarian) Doctor of Science Thesis (Hungarian Academy of Science), Miskolc, Hungary, 1994.
9. Ormos, T.: "Inversion of refracted travel-times for near-surface investigation." EAGE 64th Conference and Exhibition, Extended Abstract, D025, 2002, 1–5.

Geosciences and Engineering, Vol. 2, No. 3 (2013), pp. 83–90.

NEW INVERSION ALGORITHM FOR THE COMPUTATION OF FOURIER TRANSFORM – EXAMINATION ON A SYNTHETIC DATA SET

HAJNALKA SZEGEDI–MIHÁLY DOBRÓKA–TAMÁS BODOKY
Department of Geophysics
University of Miskolc

ABSTRACT

In order to make Fourier transform more robust and noise resistant, the tools of geophysical inverse problem theory are used. Assuming that the Fourier spectrum is given in the form of series expansion and the expansion coefficients can be determined by solving an over-determined inverse problem. The Iteratively Reweighted Least Squares (IRLS) method was used during the inversion process. Using it the geophysical inversion methods show robustness. The behavior of the new inversion-based Fourier transform method is very effective against noises.

INTRODUCTION

With a view to changing over from time domain to frequency domain, the Fourier transform is applied most frequently. The Discrete Fourier Transform (DFT) algorithm is applicable to determine the discrete frequency spectrum, if we have a discrete time domain data set. As the measured data set always contains noise, which is also projected into the frequency domain, the calculated frequency spectrum will be noisy, too. In order to decrease the influence of noise, either the number of input data must be increased. If we have more input data than inversion parameters, the inverse problem is called over-determined. P. Vass in [1] treats the Fourier transformation as an over-determined inverse problem, where the influence of noise on the spectrum can be effectively reduced by solving it. This paper presents a new robust inversion method for performing one-dimensional Fourier transform. The new method is based on series expansion of the spectrum, where scaled Hermite functions are used as basis functions. Using the special feature of the basic Hermite functions (they are the eigen-functions of the Fourier transform) the Jacobian matrix can be determined easily. It means that the element of the Jacobian matrix can be calculated without integration. The new inversion method was numerically tested on a noisy synthetic data set. The inversion results show appropriate accuracy and high noise suppression capability of the inversion-based Fourier transform algorithm.

THE THEORETICAL BACKGROUND OF THE METHOD

The Fourier transform plays a very important role in geophysical data processing. Using it we can generate the frequency spectrum of the time domain signal

$$U(\omega)=\frac{1}{\sqrt{2\pi}}\int_{-\infty}^{\infty}u(t)\cdot e^{-j\omega t}dt\,, \tag{1}$$

where $u(t)$ denotes the time dependent function and $U(\omega)$ is the complex frequency spectrum.

By means of the inverse Fourier transform we can return from the frequency domain to the time domain

$$u(t)=\frac{1}{\sqrt{2\pi}}\int_{-\infty}^{\infty}U(\omega)\cdot e^{j\omega t}d\omega\,. \tag{2}$$

In inverse problem theory various methods have been developed to extract information from noisy data sets. This can give the idea to use the method of inverse problem theory in the field of Fourier transform or in other word treatment of the Fourier transform as an over-determined inverse problem. In formulating the inverse problem the first step is the discretization. Assuming that the Fourier spectrum is given in the form of series expansion

$$U(\omega)=\sum_{n=1}^{M} B_n \cdot \Psi_n(\omega), \tag{3}$$

where B_n represents the complex expansion coefficients, $\Psi_n(\omega)$ is the n-th known basis function and M is the number of unknown series expansion coefficients. Using the terminology of discrete inverse problem theory, the theoretical values of time domain data (forward modeling) can be given by the inverse Fourier transform

$$u^{(theor)}(t_k)=\frac{1}{\sqrt{2\pi}}\int_{-\infty}^{\infty}\left(\sum_{n=1}^{M} B_n \cdot \Psi_n(\omega)\right)\cdot e^{j\omega t_k}\,d\omega=\sum_{n=1}^{M} B_n \frac{1}{\sqrt{2\pi}}\int_{-\infty}^{\infty}\Psi_n(\omega)\cdot e^{j\omega t_k}\,d\omega, \tag{4}$$

where t_k is the k-th sampled time. Thus, we have obtained a very simple direct problem.
Let us introduce the Jacobian matrix

$$G_{k,n}=\frac{1}{\sqrt{2\pi}}\int_{-\infty}^{\infty}\Psi_n(\omega)\cdot e^{j\omega t_k}\,d\omega=\mathrm{F}^{-1}\{\Psi_n(\omega)\}, \tag{5}$$

which is the inverse Fourier transform of the basis function system $\Psi_n(\omega)$. We can see that the direct problem make a relationship between the model parameters and the theoretically approximated measurement data. Then the theoretical data can be written in a linear form as

$$u^{(theor)}(t_k)=\sum_{n=1}^{M} B_n \cdot G_{k,n}, \tag{6}$$

where the unknown model parameters B_n are estimated by an inversion method.

CHOOSING BASIS FUNCTION SYSTEM - THE HERMITE FUNCTIONS

The basic Hermite functions have been chosen as basis functions because in case of inverse problems it is advised to use complete, orthogonal and normal function systems in order to reduce the number of unknown parameters and to improve the stability of the inversion procedure. The description of the basic Hermite functions can be found in [2–3]. The Hermite functions require proper scaling, because in geophysical applications the measurement of frequency covers a wide range. The scaled Hermite polynomials can be calculated by using the Rodriguez formula

$$h_n(\omega,\alpha)=(-1)^n e^{\alpha\omega^2}\left(\frac{d}{d\omega}\right)^n e^{-\alpha\omega^2} \tag{7}$$

and can be determined by the recursive formula

$$h_{n+1}(\omega,\alpha)=2\omega\alpha\, h_n(\omega,\alpha)-2n\alpha\, h_{n-1}(\omega,\alpha), \tag{8}$$

where α is a scaling factor. The first and the second Hermite polynomials are shown below [4]:

$$h_0(\omega,\alpha)=1, \tag{9}$$

$$h_1(\omega,\alpha)=2\alpha\omega. \tag{10}$$

The scaled Hermite polynomials fulfill the condition of orthogonality

$$\int_{-\infty}^{\infty} e^{-\alpha\omega^2} \cdot h_n(\omega,\alpha) \cdot h_m(\omega,\alpha)\, d\omega = \sqrt{\frac{\pi}{\alpha}} (2\alpha)^n n!\, \delta_{nm}, \quad \delta_{nm} = \begin{cases} 0, n \neq m \\ 1, n = m \end{cases}. \tag{11}$$

In the formula δ_{nm} denotes the Kronecker-delta symbol. The scaled Hermite function can be defined as

$$H_n(\omega,\alpha) = \frac{e^{-\frac{\alpha\omega^2}{2}} \cdot h_n(\omega,\alpha)}{\sqrt{\sqrt{\frac{\pi}{\alpha}}\, n!\, (2\alpha)^n}}, \tag{12}$$

where $h_n(\omega,\alpha)$ denotes the scaled Hermite polynomials. Thus the introduced Hermite functions are orthonormal

$$\int_{-\infty}^{\infty} H_n(\omega,\alpha) \cdot H_m(\omega,\alpha)\, d\omega = \delta_{nm}. \tag{13}$$

In order to get a fast and simple formula for the calculation of the Jacobian matrix a special feature of the Hermite functions was used. As we can see earlier, the $G_{k,n}$ is the inverse Fourier transformation of the basis function. This is the main reason of selected the Hermite functions, because their the non-scaled version are eigen-functions of the Fourier transform [5]

$$\mathsf{F}\left\{H_n^{(0)}(t)\right\} = (-j)^n H_n^{(0)}(\omega) \tag{14}$$

and can be written for the inverse Fourier transform

$$\mathsf{F}^{-1}\left\{H_n^{0}(\omega)\right\} = (j)^n H_n^{(0)}(t). \tag{15}$$

Based on Eq. (5) and by the scaled Hermite functions $H_n(\omega,\alpha)$ can be written for the Jacobian matrix

$$G_{k,n} = \frac{1}{\sqrt{2\pi}} \int_{-\infty}^{\infty} H_n(\omega,\alpha) \cdot e^{j\omega t_k}\, d\omega = \frac{1}{\sqrt{2\pi}} \int_{-\infty}^{\infty} \sqrt[4]{\alpha}\, H_n^{(0)}(\omega') \cdot e^{j\omega t_k}\, d\omega. \tag{16}$$

Introducing the following notations

$$\omega t = \omega' t', \omega' = \sqrt{\alpha}\omega, \; t' = \frac{t}{\sqrt{\alpha}} \tag{17}$$

it can be computed easily

$$G_{k,n} = \frac{1}{\sqrt[4]{\alpha}} \frac{1}{\sqrt{2\pi}} \int_{-\infty}^{\infty} H_n^{(0)}(\omega') \cdot e^{j\omega' t_k'}\, d\omega' = \frac{1}{\sqrt[4]{\alpha}}\, \mathsf{F}^{-1}\left\{H_n^{(0)}(\omega')\right\}. \tag{18}$$

The Jacobian matrix can be written again based on Eq. (15)

$$G_{k,n} = \frac{1}{\sqrt[4]{\alpha}} (j)^n H_n^{(0)}(t') = \frac{1}{\sqrt[4]{\alpha}} (j)^n H_n^{(0)}\left(\frac{t}{\sqrt{\alpha}}\right). \tag{19}$$

This is a very important result, because the Jacobian matrix can be derived quickly without integration.

The discretized form of the spectrum can be written according to Eq. (3) using the scaled Hermite function system, where the expansion coefficients B_n are defined (including the expression of the Jacobian matrix, Eq. (19)) in the frame of the over-determined inverse

problem. This inverse problem is highly over-determined, because the number of measurement data is much more than that of the parameters *(N>M)*. In case of Least Squares method (LSQ) the L_2 norm of the deviation vector is minimized

$$E_2 = \sum_{k=1}^{N} e_k^2 = \sum_{k=1}^{N} (u_k^{(measured)} - u_k^{(theor)})^2 = \sum_{k=1}^{N} (u_k^{(measured)} - \sum_{n=0}^{M} B_n \cdot G_{k,n})^2 = min. \tag{20}$$

The well-known normal equation can be derived from the above condition in the following form

$$\underline{\underline{G}}^T \underline{\underline{G}} \vec{B} = \underline{\underline{G}}^T \vec{u}^{measured} . \tag{21}$$

After this we can estimate the complex series expansion coefficients

$$\vec{B} = \left(\underline{\underline{G}}^T \underline{\underline{G}} \right)^{-1} \underline{\underline{G}}^T \vec{u}^{measured} \tag{22}$$

and by means of it, the real and imaginary part of the Fourier spectrum can be calculated at any frequency by using Eq. (3) [1]. The LSQ method gives optimal results in case of Gaussian distributed data set.

In order to make the Fourier transform more robust an Iteratively Reweighted Least Squares (IRLS [6]) method using Cauchy-weights was implemented. To achieve the optimal values of the unknown parameters (B_n) the following weighted norm is minimized

$$E_w = \sum_{k=1}^{N} w_k e_k^2 , \tag{23}$$

where the weighting matrix (which is a diagonal matrix) defined as

$$w_k = \frac{\varepsilon^2}{\varepsilon^2 + e_k^2} , \tag{24}$$

and the *k*-th element of the deviation vector is

$$e_k = u_k^{measured} - u_k^{theor} . \tag{25}$$

The scale parameter ε of the Cauchy distribution is not a priori given because the data residuals change from iteration to iteration. The lower bound of the scale parameter is given by [7]. The weighted norm gives reliable results for inverse problems even if the measured data set contains outliers. The *j*-th iteration step of the normal equation is

$$G^T W^{(j-1)} G B^{(j)} = G^T W^{(j-1)} u^{measured} . \tag{26}$$

This iteration is repeated until a proper stop criterion is met. Finally, the Fourier spectrum can be calculated at any frequency by using Eq. (3).

TESTING THE METHOD

In order to test the new inversion method a synthetic time domain data set was generated. The noiseless time function of the tested data was chosen in this form

$$u(t) = \begin{cases} K t^{\eta} e^{-\lambda t} \sin(\omega t + \varphi), t \geq 0 \\ 0, t < 0 \end{cases}, \tag{27}$$

where the Greek letters represents the parameters of the signal and these values were fixed during the procedure: $\kappa \approx 738.91$, $\eta = 2$, $\lambda = 20$, $\omega = 2*20\pi$, $\varphi = \pi/4$.

The noiseless time function is shown in *Figure 1*, where the time variable was sampled equidistantly to 256 points over the interval [0, 1].

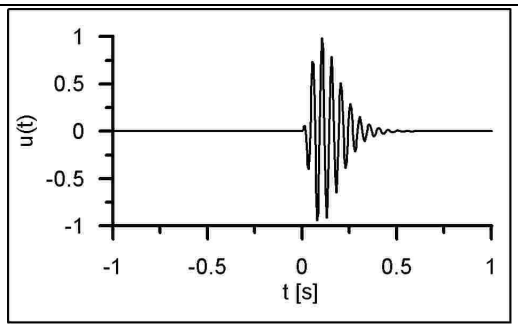

Figure 1.
The noiseless signal in the time domain

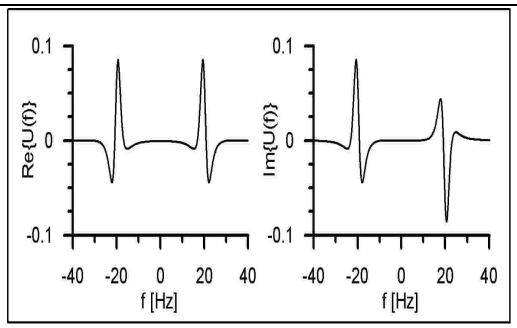

Figure 2.
The frequency spectrum of the noiseless signal

The DFT of this time domain signal was computed. The real and imaginary part of the ideal spectrum can be seen in *Figure 2*.

In order to test the noise sensitivity of DFT a Cauchy distributed noisy signal was generated with the location parameter *0* and the scale parameter *0.04*. The noisy signal is shown in *Figure 3* and the DFT of the noisy signal is represented in *Figure 4*.

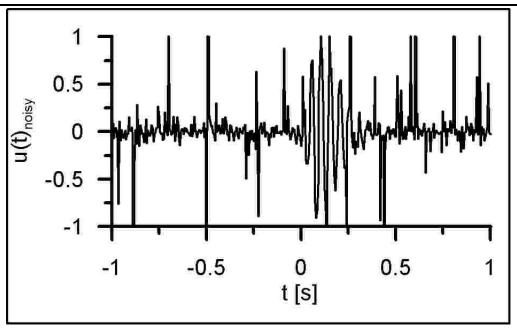

Figure 3.
The signal contaminated by Cauchy noise in the time domain

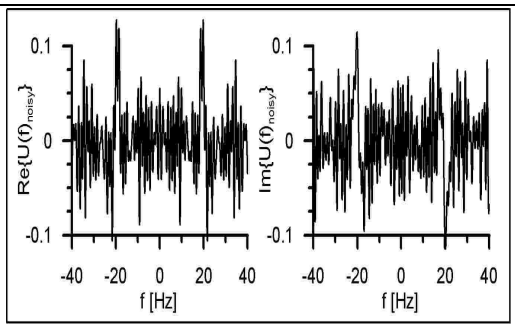

Figure 4.
The spectra of the Cauchy distributed noisy signal in the frequency domain (by DFT)

As we can see the real and imaginary part of the frequency spectra are very noisy compared to the noiseless data set (see *Figure 2*), and it is hard to recognize the ideal spectrum from *Figure 4*.

The new inversion-based Fourier transform method was numerically tested using the signal contaminated with non-Gaussian noise (*Figure 3*). The inversion results are illustrated in *Figures 5–6*.

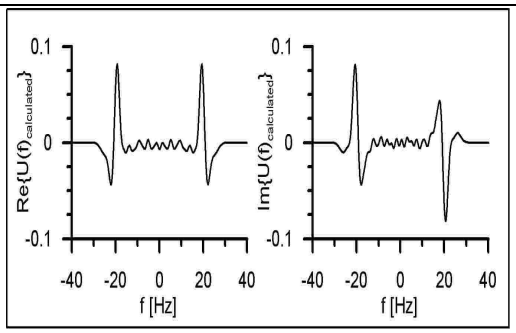

Figure 5
Frequency domain spectrum calculated by inversion

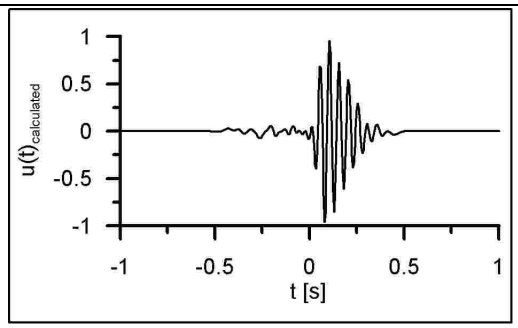

Figure 6
Time domain signal calculated by inversion

These figures show that the IRLS method provides much better estimates in both the time (*Figure 6*) and frequency domains (*Figure 5*).

In order to characterize the accuracy of the inversion results the distance between the measured and calculated data was computed

$$d_{RMS} = \sqrt{\frac{1}{N}\sum_{k=1}^{N}(u_k^{measured} - u_k^{calculated})^2}. \tag{28}$$

In the frequency domain for characterizing the deviations the root mean square of the errors (RMS) can be written in the form below

$$D_{RMS} = \left[\frac{1}{N_f}\sum_{k=1}^{N_f}\left(Re\left[U^{calculated}(\omega_i)\right] - Re\left[U^{measured}(\omega_i)\right]\right)^2 + \frac{1}{N_f}\sum_{k=1}^{N_f}\left(Im\left[U^{calculated}(\omega_i)\right] - Im\left[U^{measured}(\omega_i)\right]\right)^2\right]^{\frac{1}{2}} \tag{29}$$

where U is the Fourier spectrum, N_f implies the number of compared data pairs in the frequency domain.

Table 1 summarizes the values of RMS for both domains. If we compare the values of the two columns, a significant difference can be noticed. The higher values in the first column show that the noise caused a great deviation from the noiseless signal. The IRLS algorithm could reduce the effect of noise which is mirrored by the smaller values of RMS in both domains.

Table 1

The Root Mean Square values

	deviation between noisy and noiseless data	deviation between inverted and noiseless data
d_{RMS} (time domain)	0.103	0.035
D_{RMS} (frequency domain)	0.0107	0.0055

CONCLUSIONS

A new inversion algorithm for the one-dimensional Fourier transformation was presented. Series expansion was used for the discretization of the continuous functions of the spectrum where the scaled Hermite functions were chosen as the set of basis functions. The unknown parameters are defined in an over-determined inverse problem. Using the special property of the basic Hermite functions (they are the eigen-functions of the Fourier transform) the Jacobian matrix can be determined easily.

The IRLS algorithm provided the best accuracy of the estimation in case of outliers which can be seen in *Figure 5–6*. The proposed new inversion method has reduced the noise sensitivity of Fourier transformation even in case of having outliers.

ACKNOWLEDGEMENTS

The described work was carried out as part of the TÁMOP-4.2.2/B-10/1-2010-0008 project in the framework of the New Hungary Development Plan. The realization of this project is supported by the European Union, co-financed by the European Social Fund.

The author is also grateful for the support of the research team of the Department of Geophysics, University of Miskolc.

LIST OF SYMBOLS

B	series expansion coefficients
B_n	complex expansion coefficients
D_{RMS}	deviations the root mean square of the errors in the frequency domain
E_2	objective function
E_w	weighted norm
G	Jacobian matrix
$G_{k,n}$	Jacobian matrix
G^T	transposed matrix of the Jacobian matrix
$(G^TG)^{-1}$	inverse matrix
$H_n(\omega,\alpha)$	scaled Hermite function
M	number of unknown series expansion coefficients
N	number of measured data
N_f	number of compared data pairs in the frequency domain
RMS	root mean square
U	Fourier spectrum
$U(\omega)$	complex frequency spectrum
$W^{(j-1)}$	j-th iteration step of the weight
d_{RMS}	distance between the measured and calculated data
e_k	k-th element of the deviation vector
$h_n(\omega,\alpha)$	scaled Hermite polynomial
j	imaginary unit
t_k	k-th sampled time
$u(t)$	time dependent function
u_k^{theor}	calculated data
$u_k^{measured}$	measured (original) data
w_k	weighting matrix
$\Psi_n(\omega)$	n-th known basis function

α	scaling factor
δ_{nm}	Kronecker-delta symbol
ε	scale parameter
η	constant
φ	constant
κ	constant
λ	constant
ω	frequency domain

REFERENCES

1. Vass, P.: *Fourier transformation using inversion tools*. PhD thesis. Miskolc. 2010. (in Hungarian)
2. Dobróka, M.–Szegedi, H.–Vass, P.: "Fourier transformation as inverse problem – an improved algorithm." Acta Geodaetica et Geophysica Hungarica 47(2), 2012, 185–196, *DOI: 10.1556/AGeod.47.2012.2.7*
3. G. A., Korn–T. M., Korn: *Mathematical Handbook for Scientists and Engineers: definitions, theorems, and formulas for reference and review*. 2nd edn. McGraw-Hill, New York, 1968.
4. I. W., Gröbner–N., Hoffreiter: *Integraltafel*. Zweiter Teil. Bestimmte Integrale. Springer-Verlag, Wien und Innsbruck, 1958.
5. J. Duoandikoetxea Zuazo: "Fourier Analysis." Graduate studies in Mathematics, Vol. 29. American Mathematical Society, Providence, Rhode Island, 1995.
6. Scales, J. A.–Gersztenkorn, A.–Treitel, S.: Fast Lp solution of large, sparse, linear systems: Application to seismic travel time tomography. Journal of Comp. Phys. 75, 1988, 314–333.
7. Amundsen, L.: "Comparison of the least-squares criterion and the Cauchy criterion in frequency-wavenumber inversion." Geophysics 56, 1991, 2027–2038.

Geosciences and Engineering, Vol. 2, No. 3 (2013), pp. 91–99.

THE HYDROGEOLOGICAL RELATIONS OF THE THERMAL KARST OF THE BÜKK MOUNTAINS BASED ON MONITORING DATA

LÁSZLÓ LÉNÁRT[1]–ENIKŐ SZEGEDINÉ DARABOS[2]
[1]University of Miskolc, Institute of Environmental Management, Associate Professor
[2]University of Miskolc, Institute of Environmental Management, PhD student

ABSTRACT

The Bükk Mountain area is located in Northern Hungary. The size of the naked (cold water) karst of the Bükk is 207 km^2 and the size of the water catchment area is 230 km^2. The thermal karst water system of the Bükk is an estimated 1000 km^2 and its boundaries cannot be delineated exactly.

Firstly, in our research the geological, geophysical and thermal maps of the Bükk have been investigated. Thereafter we prove the relationship between cold and warm karst water in correlation investigations which were based on water level and temperature data of the Bükk monitoring system. According to the correlation investigations the cold and warm karst water bodies are related which cannot be separated into two independent aquifers.

These investigations can help to plan the optimum water utilization and they can provide information for the next water explorations.

INTRODUCTION

The cold karst water area of the Bükk Mountains (Northern Hungary) is surrounded by a significantly extended thermal karst water area (yielding karst water with temperatures exceeding 30 °C) in the east, west and south (*Figure 1*; [1]).

About two dozen karst springs and thermal wells can be found at the rim of the mountains and the surrounding area, yielding tepid or warm (springs), or even warm or hot thermal water (wells) (*Figure 2*). The area around the mountains is covered with a sediment layer. Their water catchment areas are situated in the limestone areas of the Bükk Mountains. The cold karst water system of the Bükk is regarded as a unified system. The data presented by Nv-17 karst water monitoring well are accepted to represent typical karst water levels. In the present paper we are concerned with the relations of the open and covered karst in the area with regards to karst waters.

Miskolc is the third largest city (with a population of around 170.000) in Hungary with a famous Miskolctapolca cave-bath based on the thermal groundwater coming from the deep section of the karstic Bükk Mountains. This huge karst reservoir is also the main water resource for the city water supply in Miskolc. The city waterworks carries out intensive water production from the two main wells (namely the New-well and the Thermal-well) at the rim of the Bükk Mountains. The New-well discharges the upper cold part of the karst aquifer system with an average rate of 30.000 m^3/day. The Thermal-well provides warm water for the world-famous cave-bath from the deeper section of the karst system with an average production rate of 2.700 m^3/day [2, 3].

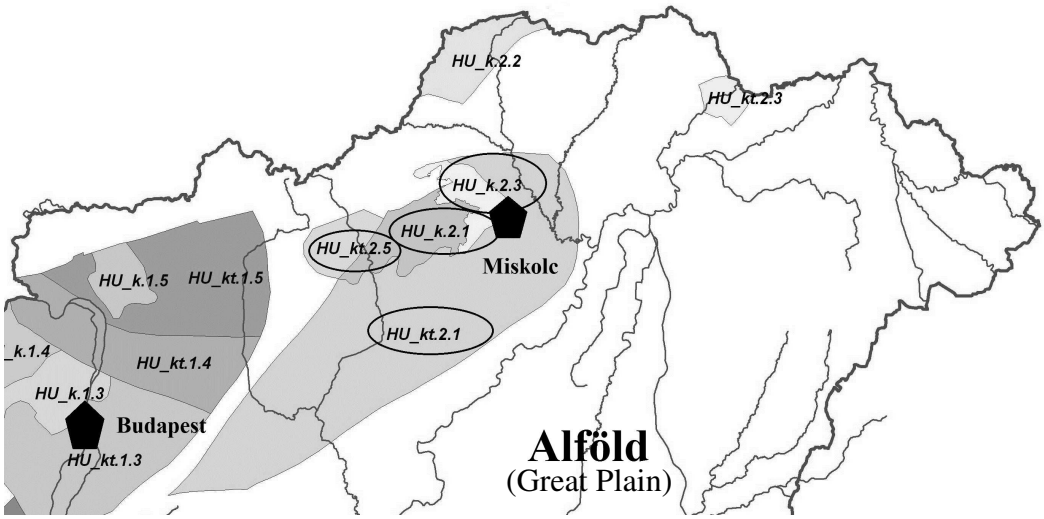

Figure 1.
The karstic water bodies of Northern Hungary represented by the grey areas [1]
k: cold karst; kt: thermal karst; k.2.3 = Bükk eastern karst; k.2.1 = Bükk western karst; kt.2.1 = Bükk thermal karst; kt.2.5 = Recsk-Bükkszék thermal karst

MATERIALS AND METHODS

The size of the unconfined (open) karst system is about 207 km^2 (marked by numbers 116; 118; 130; 134 in *Figure 2*) and stretches from the east to the west in patches. It means that the line of bearing of Carboniferous-Permian (134; 141) and Triassic-Eocene (116; 118; 130) carbonate rocks is east to west. (The most significant faults are also oriented from the east to the west but at the rim of the mountains faults perpendicular or at an angle to it are also to be found.)

The precipitation on the open (unconfined) karst of the Bükk infiltrates the karst, and either leaves it through springs, or moves towards the Alföld (Great Plain) region through the limestone layers stretching beneath the Cenozoic sediment layer, due to the pressure differences of the karst water relief of the Bükk.

Due to ground heat (convection) the cold karst water warms up along its flowpaths. (Note: the convection value of 100 mW/m^2 measured at the Great Plain (Alföld) is gradually decreasing as it reaches the rim of the mountains. In the middlemost area of the Bükk it is as low as 40 mW/m^2 [4].

For technological reasons, the dividing line between cold and warm (karst) water is drawn at a temperature of 30 °C in Hungary. (Nature doesn't allow for such sharp line to be set but for technological and legal reasons let us accept this value as the dividing line.)

The 30-degree-Celsius isotherm is located under the Bükk Mountains at a depth of 900–1400 m. Its depth is rapidly decreasing towards the rims. There is no possibility of exploiting the thermal karst water in the Bükk, it could only take place in the covered karst, further away from the Bükk's rim. The reason for this is that the thermal karst water can be found at great depths, and it has direct hydrological connection to the cold karst water. Caves containing thermal karstic formations are found at the brim of the Bükk. These formations were created by upwelling karst water. Despite this, the thermal karst genetics remains questionable for many scientists.

The largest karst spring of the Bükk (cold and warm water spring group) is at Miskolctapolca. The location of thermal karst water springs and wells are specified on Figure 2. The Miskolctapolca spring group is located at 127 m aBS (above Baltic Sea) level.

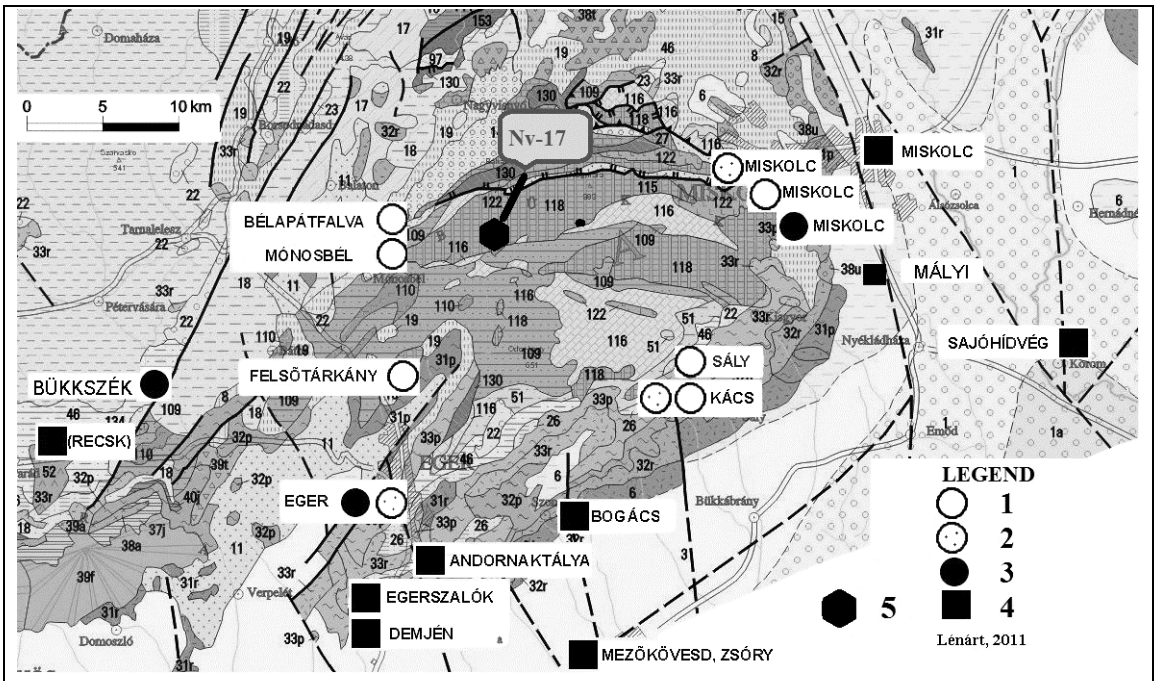

Figure 2.
The thermal karst draft of the Bükk region with location of the Nv-17 cold karst water monitoring well [based on the map of Lexa et. al 2000; Lénárt 2012;
1: cold tepid karst water, 10–16 °C; 2: warm tepid karst water, 16–25 °C; 3: warm karst water, 25–37 °C; 4: hot karst water, above 37 °C; 5: Nv-17: Bükk, Nagy-fennsík, standard level measurement site of cold karst water;]

The maximum karst water level at the Bükk Plateau (Nv-17) has been measured 550 m aBS level. The average of karst water level between 1992 and 2012 was 530 m aBS level. This means that since the karst water level at Miskolctapolca is at 127 m aBS, and the average and maximum water level of the open karst water system in the Bükk area is at a much higher level, it generates a 40–42 bar pressure difference, thus causing the water to flow [5].

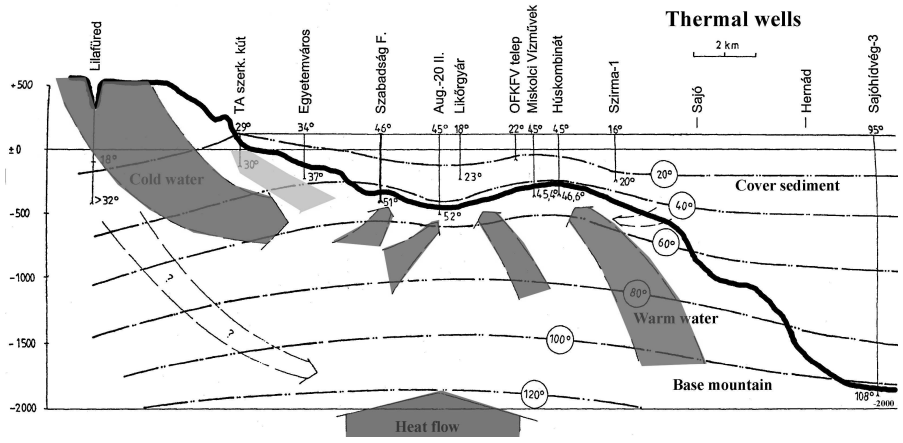

Figure 3.
The overview of the thermal karst system in Miskolc surroundings, NE to SW [6]

The large open karst is "well karstified" from the surface to 300 m underground. The cold water infiltrating the large open karst is moving in the upper zone of the karst limestone

layer which stretches under the sediment layer in the Miskolc pilot area of the Bükk (*Figure 3*) [6].

The thickness of the "well karstified" zone is probably about the same in the case of covered (confined) karst but drillings did not penetrate to deeper than 100 meters. The carbonate layers are located deeper and deeper. Around Köröm (Sajóhídvég), the base temperature exceeds 100 °C at a depth of 2000 m below Baltic Sea level. The 30 °C isotherm is not marked on the Figure. The presentation of values 20 and 40 °C was based upon, among others, the published data of the Pávai Vajna well which is highly debated even today [13].

In order to determine the exploitability of karst water it is very important to have more accurate data, but based on the data of the karst water monitoring wells, caves and springs, we can conclude that the 30 °C isotherm is located in more depth even in the area marked than it is shown on the Figure 3. The drilling at Mályi in 2010 reached a 2300-meter depth. It is not shown on the relevant figure as the investor treats the official data of the drilling confidential. The temperatures measured in the drill are very similar to the values measured in the monitoring well at Köröm.

The open karst water catchment area of Eger (including Egerszalók and Demjén) is neither as large nor as unified as the Miskolc aquifer. Due to heavily tectonized structure and significant karsting, the karst water warms up in the depth and moves along the faults (*Figure 4*) [7]. The temperature of the karst water reaching the surface is almost the same even if it comes from depths of 300 or 900 m below Baltic Sea level (65–68 °C). At the brim of the mountains, some wells yield water colder than this. The well K-12, drilled in 2011 in Demjén, is 1514 meters deep. The highest temperature measured in the K-12 well is 79 °C, and karst water that reaches the surface is 73 °C. The water cools 6 degrees on its way. In the Miskolc area, from the depth of 400–500 m below Baltic Sea level, the temperature of the karst water is 40–45 °C.

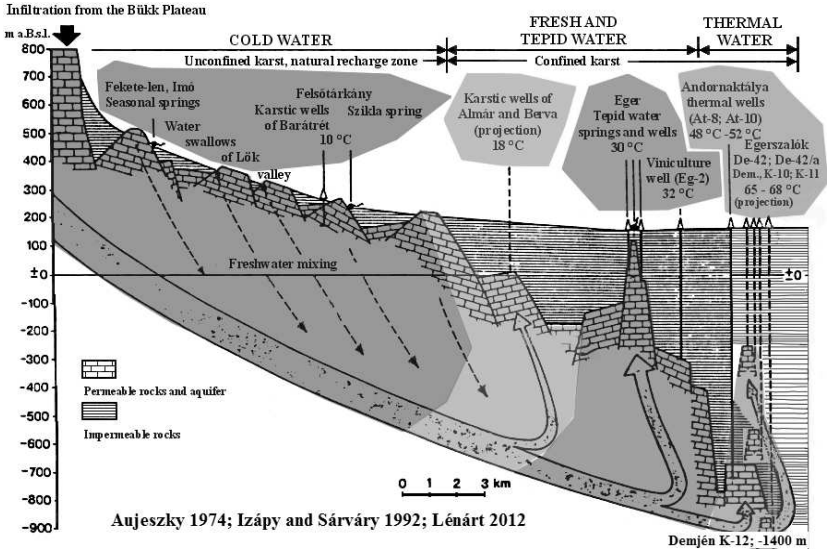

Figure 4.
Overview of the thermal karst system in Eger surroundings, without Demjén K-12
[Based on Aujeszky 1974; Izápy and Sárváry 1992; Lénárt 2012]

RESULTS

Figure 5 shows the fluctuation of the annual volume of water, exploited in the surroundings of the Bükk and discharging from springs at the brim of the mountain.

The water is mostly used for medical, therapeutic and bathing purposes in the region, but the communal use is also significant. At certain places it is also sold as drinking water. The greatest possibility for development is for energy production. Most of the bathing establishments cool the water by using heat exchangers, but the utilization of the wasted heat for energy production is still very limited. Drillings have been done in Mályi and Kistokaj in order to support the central heating system of Miskolc city but the system is not yet completed.

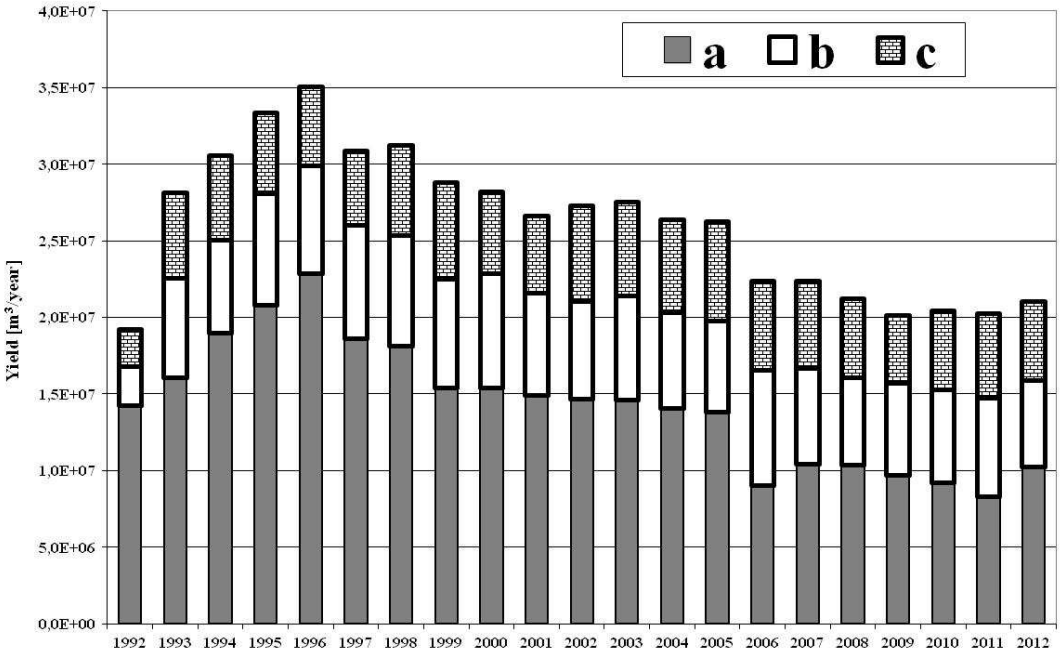

Figure 5.
The karst water exploitation of the Bükk Mountains by temperature
[a: cold; b: warm tepid; c: warm and hot]

The closest relationship is considered to be the one between the water levels of Nv-17 and the Termál spring (*Figure 6*).

(In *Figure 2* the Thermal spring is marked as "Miskolc warm karst water".) One of the reasons for this is that the distance of the cold and warm springs at Miskolctapolca is about 80 m, and between them limestone and mountains rim gravel layer can be found. Also, the flood overflow of the warm spring (Termál spring) is located only less than a meter above the flood overflow of the cold spring. It means a tight spatial relationship. (About 100 years ago there were many dozens of cold, tepid and warm springs but in order to concentrate the water yields, for water exploitation reasons, the number of springs basically decreased to two.) Also, above all the water yielding objects under examination, the Termál spring is situated closest to the karstic feeding area [8–11]. The sole most important use of the water of the Termál Spring is to supply water to the Cave Spa (Barlangfürdő). We consider the relationship very tight (*Figure 7*) between the pressure levels of Nv-17 and the Vízmű and Selyemréti I. thermal well of the water company. (These two thermal wells are under "Miskolc thermal water" on *Figure 2*, and their distance is about 1 km.) Both thermal wells basically react immediately in the same way and for longer durations when the cold karst

water pressure level is on its peak. (Naturally due to the fluctuation of water exploitation it is not possible to follow the changes of smaller magnitudes.) They are situated at a greater distance from the feeding area, and they yield the water moving in the limestone layers that are the subsurface extensions of the east-to-west patches of the open karst aquifer. The relationship is much looser in case of the Nv-17 and the wells of Egerszalók and Demjén (*Figure 8*). For one thing, these are located much further away from the feeding area, and also situated perpendicular to the carbonate patches stretching east to west [12]. These are shown in *Figure 2* as "Egerszalók, Demjén thermal karst water". The distance between the two wells of Demjén is 1 km. The distance between the wells of Egerszalók – De-42 and De-42a – is about 15 meters. Well De-K-11 is closest to the Mátra Mountains. The Mátra is a mountains range whose surface is non-karstic rock. The above-mentioned Demjén K-12 well is the deepest in the area, with its depth of 1514 meters. During its test run it affected the Demjén K-10 and Demjén K-11 wells the most.

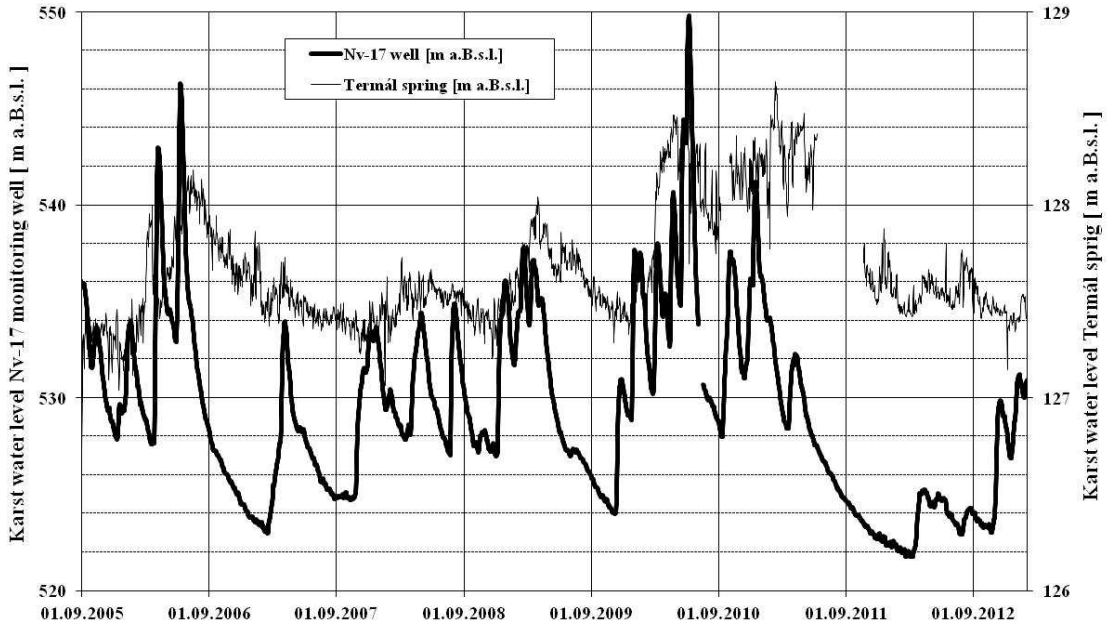

Figure 6.
Comparison of the water levels recorded at the Nv-17 karst water monitoring well and the Termál spring of Miskolctapolca

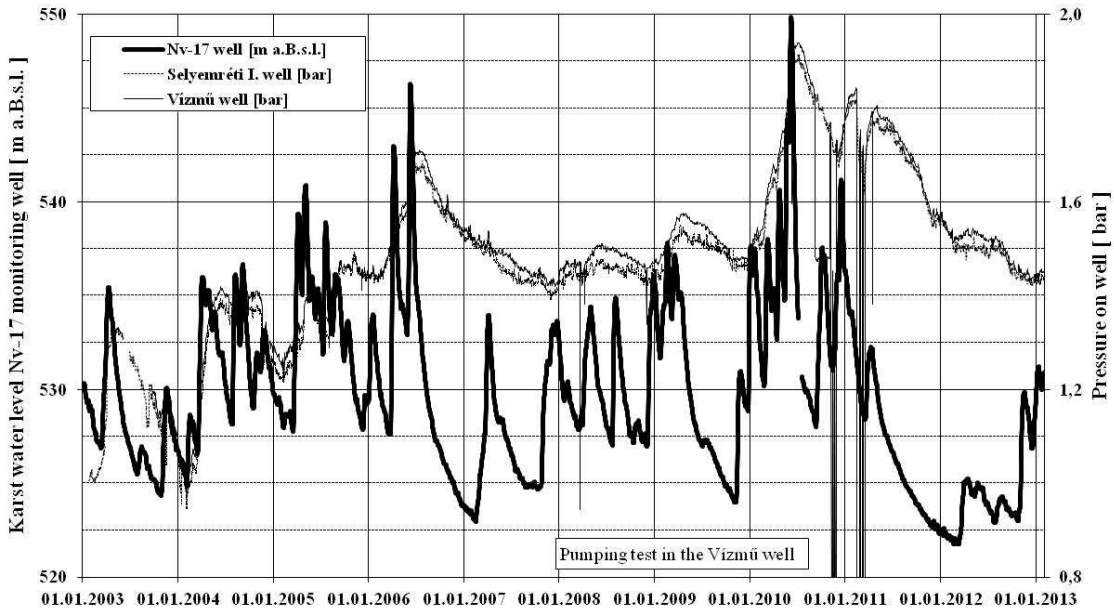

Figure 7.
The relationship of the Nv-17 karst water monitoring well and 2 thermal karst water wells of Miskolc

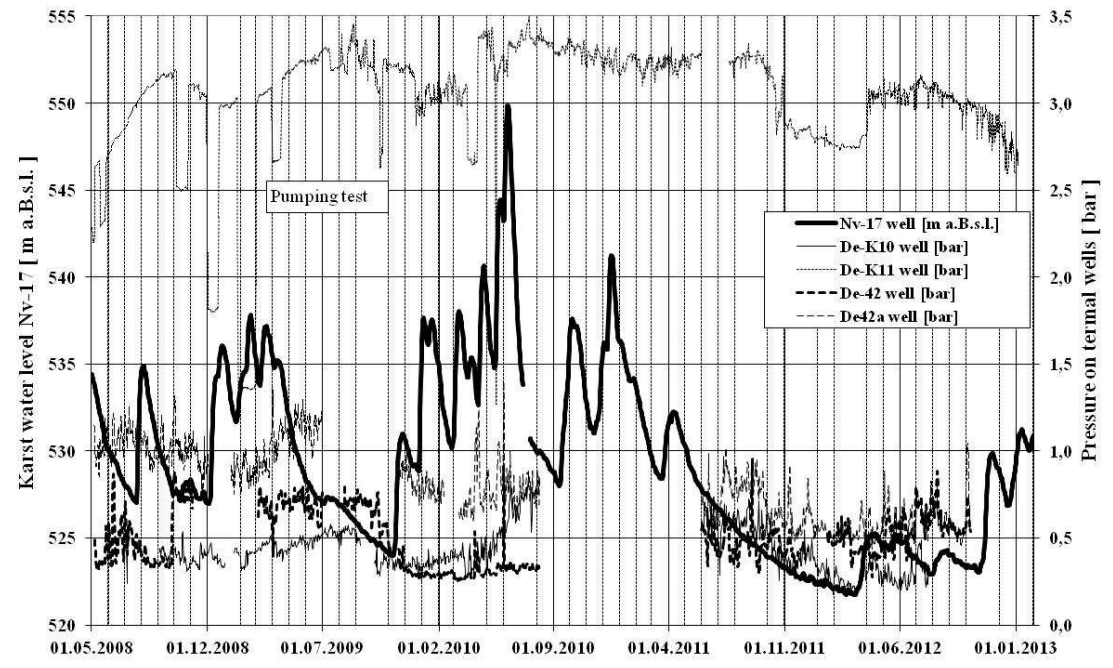

Figure 8.
The relationship of the Nv-17 karst water monitoring well and 4 thermal karst water wells of Egerszalók-Demjén

CONCLUSIONS

According to the correlation investigations which have been based on the water level data of 20 years long measurements, the relationship between the cold karst water level and warm karst water level (pressure level) is clear but its tightness differs. The tightness of the relationship increases in case of wells situated in the east-west carbonate patches, but it weakens in case of wells situated perpendicular to such patches.

Comparing the temperature data with geological and thermal maps, it can be stated that the temperature of the thermal karst water increases when moving further away from the mountain boundaries, evenly with the depths in the Miskolc area. But due to the horst structure in the area of Egerszalók and Demjén the increase of temperature is independent of depth.

The thermal karst water moves along tectonic zones (Egerszalók, Demjén area) or in the karstic zones which were naked (unconfined) karst surfaces (Miskolc area) in the earlier geological ages.

According to available data, the cold karst water of the Bükk with its 42 bar pressure pushes the thermal water (30 °C) into 900–1400 m deep layers. So the thermal water explorations in the centre of the Bükk Mountains and its rims are needless. Because the zone with the necessary temperature is at great depths or the porosity of the aquifers in these depths is very low (it cannot serve enough water). If there was adequate porosity (for example a cave) in the required depths, the cold karst water would flow into the well and it would cool off the thermal karst water. Also a confirmation of this statement is the thermal karst water exploration work of F. Pávai-Vajna in the centre of the mountains near Lillafüred, which actually failed.

ACKNOWLEDGEMENT

This work was carried out as part of the TÁMOP-4.2.1.B-10/2/KONV-2010-0001 project in the framework of the New Hungarian Development Plan. The realization of this project was supported by the European Union and, co-financed by the European Social Fund.

REFERENCES

1. Liebe, P. [Editor]: *Guide groundwaters in Hungary.* Compiled by The Hydrological. Institute of VITUKI Plc. Ministry of Environment and Water. Budapest, 2002.
2. Szűcs, P.–Horne, R. N.: "Applicability of the ACE Algorithm for Multiple Regression in Hydrogeology.", Computaltional Geosciences 13., 2009, pp. 123–134, Springer.
3. Darabos, E.–Szűcs, P.–Németh, Á.: "Application of the ace algorithm on hydrogeological monitoring data from the Bükk mountains." Acta Geodaetica et Geophysica Hungarica, Volume 47, Number 2, 2012, pp.: 256–270 Akadémiai Kiadó, Budapest.
4. Dövényi, P.–Horváth, F.: "A review of temperature, thermal conductivity, and heat flow data for the Pannonian basin." In: Royden L. H., Horváth F. (Eds.), The Pannonian Basin. A study in basin evolution. AAPG Memoir, 45, 1988, 195–233.
5. Lénárt, L.: "The Interaction of Cold and Warm Karst Systems in the Bükk Region." Proc. of the 1th Knowbridge Conference on Renewables, 2010, pp. 111–118, Miskolc.
6. Szlabóczky P.: „Karsztvíz tározó rendszer termohidraulikai vizsgálata Miskolc környéki adatok alapján." *Hidrológiai Közlöny,* 1974, Vol. 54, No. 11, pp. 516–523.
7. Izápy G.–Sárváry I.: *Tájékoztató a karsztos termálvizek állapotáról*. Miskolctapolca, Mezőkövesd, VITUKI, Budapest, 1992.
8. Kovács, B.–Lénárt, L.–Tamás, J.–Bíró, T.: "Determination of the hydrogeologic protection area of the cold and warm karstic water regime of Miskolctapolca using numerical methods", COST629 WG1 Workshop, September 4–5, 2006, CAGLIARI Sardinia.

9. Lénárt, L.: *Some aspects of the „3E's" (Economics-Environment-Ethics) model for sustainable water usage in the transboundary Slovakian and Aggtelek karst region based on some examples from the Bükk Mountains*. PhD thesis work, Kassa/Kosice, 2005a
10. Lénárt L.: Termálkarsztok Észak-Magyarországon és Dél-Szlovákiában; hévizes barlang-képződésre utaló nyomok e területek barlangjaiból. (Summary: Thermalkarsts in Northern Hungary and Southern Slovakia; Traces of Thermal-cave Forming in the Caves of these Areas) Hévizes barlangok genetikája és képződményei. MKBT, 2005b; pp. 54–60, Budapest.
11. Mádai, F.–Németh, N.–Szendi, A.–Lénárt, L.–Hevesi, A.: "Minerals, history and vines – trip to Miskolc, Miskolctapolca and the Bükkalja region." Acta Mineralogica-Petrographica, Field Guide Series, Vol. 12, 2010, pp. 1–12.
12. Lénárt L.–Hernádi B.: „A bükki termálkarsztvíz hőmérsékletének morfológiai, földtani és vízföldtani okai." A Kárpát-medence ásványvizei IX. Nemzetközi Tudományos Konferencia, 2012.08.30–09.01, (ISBN 978-973-7625-37-3) pp. 25–36, Herkulesfürdő, Románia.
13. Pávai Vajna F.: A lillafüredi kutató mélyfúrás eddigi története és geológiai viszonyai. *Hidrológiai Közlöny*, 9. évf. 1929, pp. 38–50, Budapest.

Geosciences and Engineering, Vol. 2, No. 3 (2013), pp. 101–109.

POTENTIAL TEPID AND HOT WATER RESOURCES IN THE TOKAJ MOUNTAINS

ZOLTÁN FEJES–PÉTER SZŰCS
MTA-ME Research Group of Geoengineering,
Department of Hydrogeology and Engineering Geology,
University of Miskolc

ABSTRACT

Thermal water exploration in volcanic areas is a more complex task than in porous systems. The literature has negligible information about potential thermal reservoirs of the Tokaj Mountains; furthermore, the hydraulic parameters of the volcanic rocks are also unknown. In our study the possible occurrences, locations and hydrogeological parameters of potential thermal water aquifers Tokaj Mountains will be investigated. The geothermal gradient and hydraulic parameters of volcanic formations were calculated by several methods to find the best method. According to our calculations the aquifers associate with fissured rocks and the highest discharge is experienced along fault lines. The final aim of our research is to provide information and data to plan the geothermal water supply in the region.

INTRODUCTION

The Tokaj Mountain range, located in the north-eastern part of Hungary as part of the Carpathian Basin, is one of the most famous volcanic mountains of Hungary. Its strike is to the north-south, and it is approximately 100–120 km long. The mountain runs between Tokaj and Eperjes (Prešov) [1]. The thermal and geothermal research in the Tokaj Mountains has always had secondary importance from the point of view of hydrogeologists, due to its complex geological structure and the insufficient number of deep exploration wells. In 2012 the Department of Hydrogeology and Engineering Geology at the University of Miskolc started a very detailed hydrogeological survey of the wells of the entire Northern Hungary region. During our research we have observed that many potential thermal aquifers can be found in the investigated area, despite the complex geological structure. The aim of our research was to characterize the hydrological parameters of the thermal aquifers and the geothermal gradient of the area with numerical methods.

MATERIALS AND METHODS

We have defined the investigated area mainly by natural boundaries. The boundary in the North is the Hungarian–Slovak border, while the western boundary runs along the Hernád Valley, which is a north-northeast south-southwest structural line, known also as the ALCAPA-Tisza tectonic line, a part of the Central Hungarian lineament. The southern boundaries of the area are the Tisza and Sajó Rivers. Finally, the eastern borders are the Tisza and Bodrog Rivers (*Figure 1*). The geological structure of the Tokaj Mountains is very complicated and elaborated. The depth and the material of the basement are still in question, although many of basement maps show that it is at approximately 1500–2000 m depth, and the material of the basement is probably metamorphic mica.

Concerning the geological structure of the investigated area, it has been proved by the thermal karst of Sárospatak and Bükk that shallow marine carbonate sediments were deposited in the research area in the Triassic. Neogene vulcanite formations settled to the basement materials with hundreds or – in some places thousands – of meters in thickness. The reason for the extraordinary thickness is that the volcanism started in the Miocene and

ended in the Lower-Pannonian. The Pannonian Lake gradually lost its salinity, and it was charge by the river-drift. The Upper Pannonian clastic sediments pinched out on the southern part of the research area, but toward the Great Plains their thickness increases. In several areas above the Pannonian layers Pleistocene fluvial sediments have settled in large thickness. In those areas the Holocene formations are negligible.

The hydrogeology of the research area is very diverse and complex, confirm the geological structure. We have classified potential groundwater bodies by the 2010 Watershed Management Plan (WMP). The WMP divides the Tokaj Mountains into two parts: the northeastern part is the Tokaj Foothills and the southwestern part is the watershed of the Hernád and Takta rivers. Four groundwater body types can contain potential hot water aquifer formations. *Table 1* shows the groundwater bodies in the research area [2].

Table 1

Potential warm water aquifers in Tokaj Mountains

Type of groundwater body	Name of area	Surface
Mountainous	Zemplén Mountains–Hernád Watershed	504.1 km^2
	Zemplén Mountains–BodrogWatershed	615.1 km^2
Porous	Sajó–Hernád Valley	458.2 km^2
	Sajó–Takta Valley, Hortobágy	303.1 km^2
	Bodrogköz	61.9 km^2
Porous thermal	Basins of the Northern Mountains	1142.6 km^2
	Northern Great Plains	28.7 km^2
Thermal karst	Thermal karst in Sárospatak	62.2 km^2
	Thermal karst in the Bükk Mountains	174.3 km^2

It is a difficult task to define precisely the boundaries of the groundwater bodies boundaries, but estimated values show the potential hot water reserves in each area. In the last few years, many wells have been screened to these groundwater bodies, and their effluent water temperature was warm (25–37 °C) or sometimes hot (37–60 °C). *Figure 1* shows the wells in the research area, which have an effluent water temperature, higher than 18 °C. The temperature limits are corresponding with the temperature classification of Bélteky–Papp–Schmidt [3] (75 p.). As the first step of the geothermal exploration of the research area, we defined the geothermal gradient using four different numerical methods from the bottom-temperature values of 18 wells. With the resulted geothermal gradient values we calculated the bottom temperatures, and by the comparison of the calculated and measured bottom-temperature values we got the variance

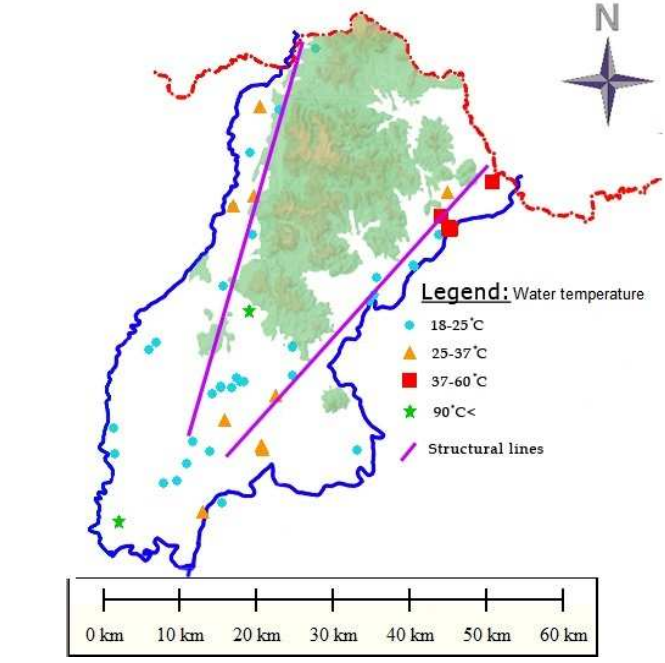

Figure 1.
Tepid- and warm water wells in the Tokaj Mountains with the main structure lines

and applicability of the different numerical methods. The geothermal gradients were calculated using the following approaches:

1. *Bobok–Tóth* equation [4]

$$gg = \frac{T_z - 11}{z} \cdot 100 \tag{1}$$

2. *Szlabóczky* formula [5]

$$gg^* = \frac{z - 20}{T_z - 10} \tag{2}$$

3. *Depth vs. bottom-temperature method*: The measured bottom temperatures versus the depth of the wells have been plotted. We have fitted a linear regression curve to the points; the slope of the curve gave the geothermal gradient of the area.

$$T_z = \frac{z + 337{,}75}{18{,}127} \tag{3}$$

4. *The effluent water temperature vs. bottom-temperature method*: From the measured bottom temperature and the effluent water temperature values of the wells we could calculate an average cooling coefficient for the investigated area.

$$h^* = \frac{100 \cdot (T_z - T_{out})}{z} \tag{4}$$

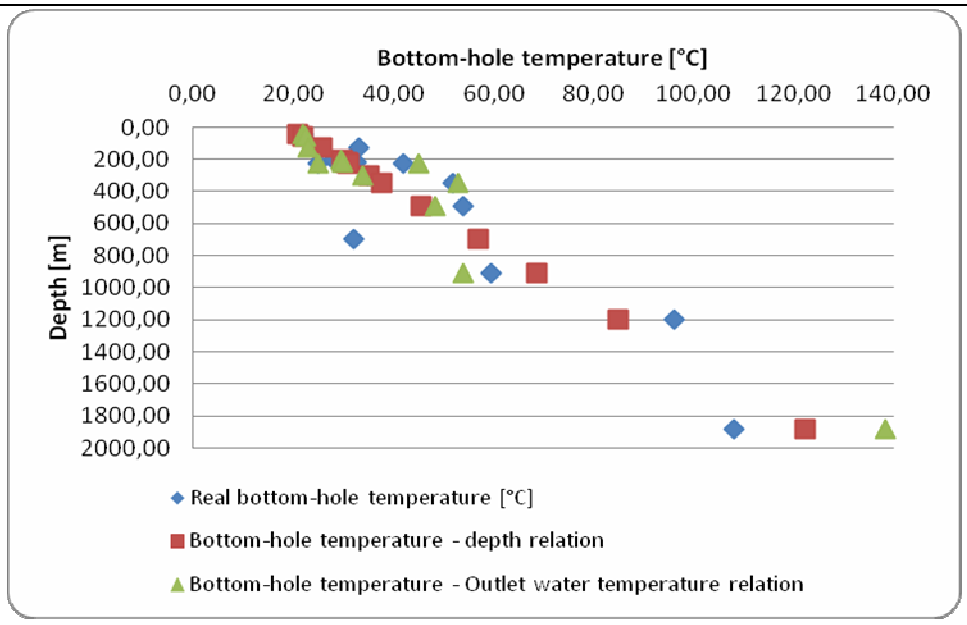

Figure 2.
The measured and calculated bottom temperature values vs. depth

The measured and calculated geothermal gradient values showed that the depth vs. bottom temperature and the bottom temperature vs. effluent water-temperature equations shown in *Figure 2* gave the most precise values of the four approaches (all of correlation coefficient are higher, than 0,9, but the bottom temperature vs. effluent water-temperature

equations have the best maximum difference value [25,03 °C]). *Figure 1* shows, that all wells located in the edge of the mountains. In the research area, there are many thermal water aquifer formations. Wells in the southern part of the research area are dominantly screened to porous aquifers (Pleistocene and Pannonian layers), the thicknesses of these layers are increasing to the increases southwards; therefore, the effluent water temperature is also increasing. These Pleistocene and Pannonian formations are excellent aquifers, they consist of high porosity sediment layers with good porosity and excellent aquifer properties, but they are too shallow, and the geothermal gradient cannot prevail. Only in the southern parts of the area did the Pannonian layer reach a sufficiently large depth to provide hot water.

By using the results of pumping tests, we have determined with different methods the average hydraulic conductivity of the Upper Pannonian formations:

1. *Logan–Schieder* equation [3] (299 p.):

$$k = 3.11 \cdot \frac{Q}{s_0 \cdot l}. \tag{5}$$

2. Dupuit–Thiem equation with iteration [3] (291 p.):

$$Q = \frac{2 \cdot m \cdot \pi \cdot k \cdot \left(H - h_0\right)}{\ln \frac{R}{r_0}} \tag{6}$$

$$R = 5000 \cdot \sqrt{k} \cdot s_0. \tag{7}$$

3. *Krasznopolszkij* equation [5]:

$$k = \frac{Q}{2 \cdot \pi \cdot m \cdot \sqrt{s_0 \cdot r_0}}. \tag{8}$$

The calculated hydraulic conductivity values of Pannonian sediments are presented in the next section. Within the research area main aquifers are Pleistocene sands and Upper Pannonian sand and gravel. The yield of these aquifers is high (k = ~4,1 m/d) (*Table 2*) and increases with depth, but the recharge of the wells is limited, due to the poor infiltration conditions from the mountain side. The groundwater level can dramatically decrease because of the inadequate production rates of the wells. (In the case of Prügy Waterworks, the dynamic water level sinkage was 43 m!). In spite of its favorable hydrological and geothermal conditions, only a few deep wells were settled in the south part of the investigated area. In Kesznyéten and Girincs the depth of the wells did not reach 100 m, but the bottom of the Upper Pannonian formation is at more than 1000 m depth. From the calculated geothermal gradient, at this depth we can expect the water temperature to be approximately 70 °C with a yield of 900–1100 l/min.

The most significant Neogene thermal aquifer formations are cracked tuff layers, in which thermal water flows in a rift system to the wells. At the research area thermal wells are located along the Hernád and Bodrog tectonic lines; thermal water updraft is possible through these wells (*Figure 1*). The greater part of the Tokaj Mountains was formed from high and medium strength porous Miocene (Tertiary) volcanic rocks and debris [5]. These rocks have medium hydraulic conductivity (k = ~0,2 m/d) (*Table 2*). The lava rocks (rhyolite, dacite and andesite) and tuffs store fissure water, with their hydraulic conductivity depending on the

fracture system. It is important to take into consideration that hydrogeological and geothermal properties of host rocks cannot be determined with single values; the change in their parameters can be described with frequency curves. The curve requires a great deal of data, but for the characterization of the rocks this is the most accurate method. In the case that measured data is lacking, the characterization is made using the minimum, maximum and the most frequent values.

Due to weathering, the lava rocks near the surface crack and their porosity increases, however, deep lava rocks are very poor porosity. In these rocks, the groundwater could leak into micro-fissures. The temperature of the subsurface lava rock can be higher than its surroundings; in Vajdácska the 200 m deep andesite formation raised the water temperature of the overlying aquifer (*Figure 3*).

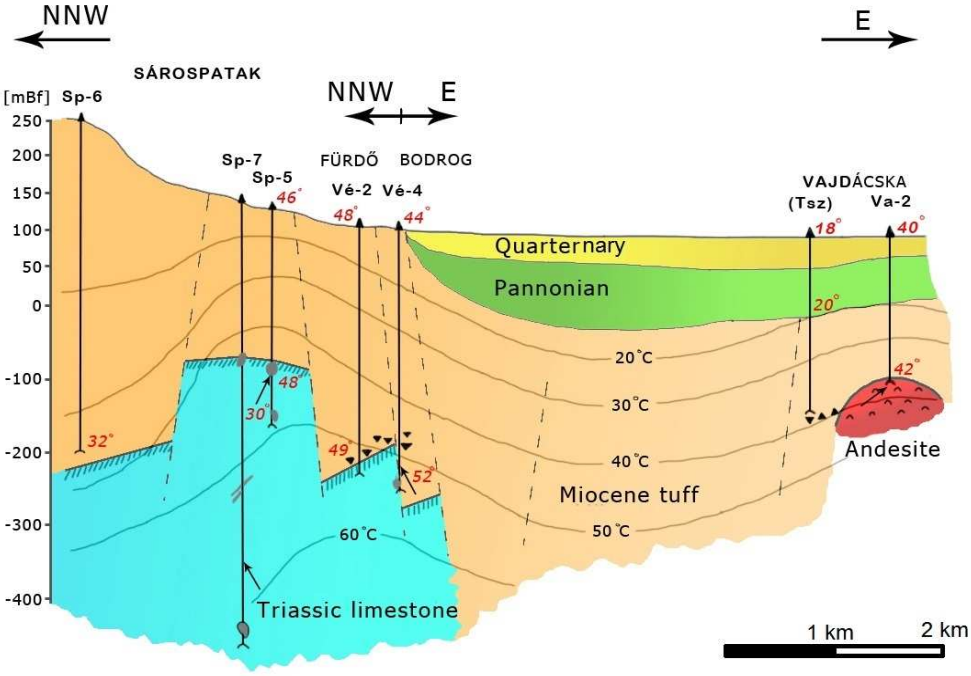

Figure 3.
Geothermal profile between Sárospatak and Vajdácska [6]

Characterization of hydraulic properties of subsurface lava rocks was carried out from the literature and from the evaluation of the pumping tests evaluation on Tállya-15 well. The pumping-test equations presume a porous, homogenous aquifer; therefore, the calculated values are equivalent hydraulic conductivities. The equivalent hydraulic conductivity was determined by the pumping tests of wells screened to the tuff formations. Hydraulic properties of a fractured system depend on the depth, the tectonic effects and the ratio of clay minerals. The water warms up in the subvolcanic formations, the silica content increases, and thereafter flows upward through a fracture system. During the flow, the water cools and the silica precipitates along the flow path. The most conspicuous occurrence of these formations is the top of Árpád Roof in Szerencs. Electrical Resistance Survey (ERS) measurement detected hydrothermal quartzite lead; the estimated sinkage of the lead is determined by the surface outcrops and the data of deep-wells *(Figure 4)*. The hydraulic conductivity depends on the rate of the clogging, the lead could behave as an aquitard if clay minerals fill the lithoclases.

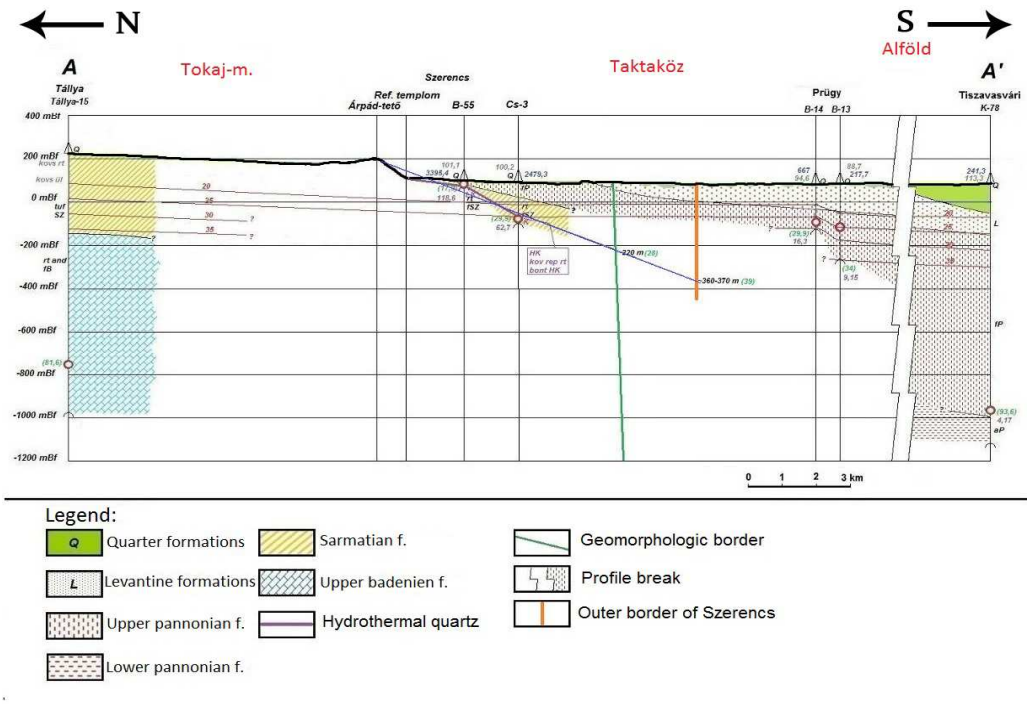

Figure 4.
The estimated sinkage of the hydrothermal quartzite

The covered thermal karst aquifers in the northeastern and southwestern part of the investigated area have the maximum water temperature values; the effluent water temperature is about 40 to 70 °C from the depth of 300–1000 m. The deeper wells (1800–2000 m) of the thermal karst give higher temperature water. The Bükk karst formation and Sárospatak karst formation have quite different recharge conditions. The Bükk karst bodies have high recharge from the Bükk, but the Sárospatak karst has very poor recharge conditions from the Tokaj Mountains, and thus the static water level has been decreasing for years in the thermal wells in Végardó thermal wells (Vé-2, Vé-4) *(Figure 3)* [7]. The equivalent hydraulic conductivity has been determined by the pumping tests of the wells of Végardó screened to the karst aquifer formations.

RESULTS

We have performed hydrogeological investigations on many thermal water aquifers of the Tokaj Mountains to characterize hydraulic properties of the formations. The calculated values (geothermal gradient and hydraulic conductivity) can provide a good basis for the further geothermal exploration of the area. *Table 2* presents hydrogeological parameters of groundwater aquifer formations in the research area.

Table 2

Hydrogeological parameters of potential warm water aquifers in the Tokaj Mountains

Formation	Hydraulic conductivity [m/d]	Permeability [m^2]	Transmissivity [m^2/s]		
			min.	max.	med.
Pannonian sand	4.1	2×10^{-9}	3	300	77
Miocene tuff	0,2	1.9×10^{-8}	-	-	-
Miocene rock (compact)	4.6×10^{-3}	-	8.7×10^{-5}	4.3	0.3
Hydrothermal quartzite	8.1	1.3×10^{-7}	3	289	118
Carbonate rock	0.9	2.3×10^{-9}	3.8	68	20

Results were as follows:

- The average cooling coefficient for the investigated area is 2.3 °C/100 m, but there was high variance in the average cooling coefficient values; therefore we used **7.4 °C/100 m** for the geothermal gradient, based on the depth vs. bottom-temperature equation.
- From the calculated geothermal gradient value, the isotherm of 30 °C temperature is located at a depth of 270–280 m. *Figure 5* shows the depth of the Upper Pannonian formations in the southern part of the Tokaj Mountains (based on the map of Csíky G. et al. [8]); formations that are potential thermal aquifers are highlighted in green.
- We performed infiltration tests in Szerencs to characterize the vertical hydraulic conductivity of the upper weathered part of the tuff. Based on these measurements the values of hydraulic conductivity were in the range of 2.7–5.1 m/d.

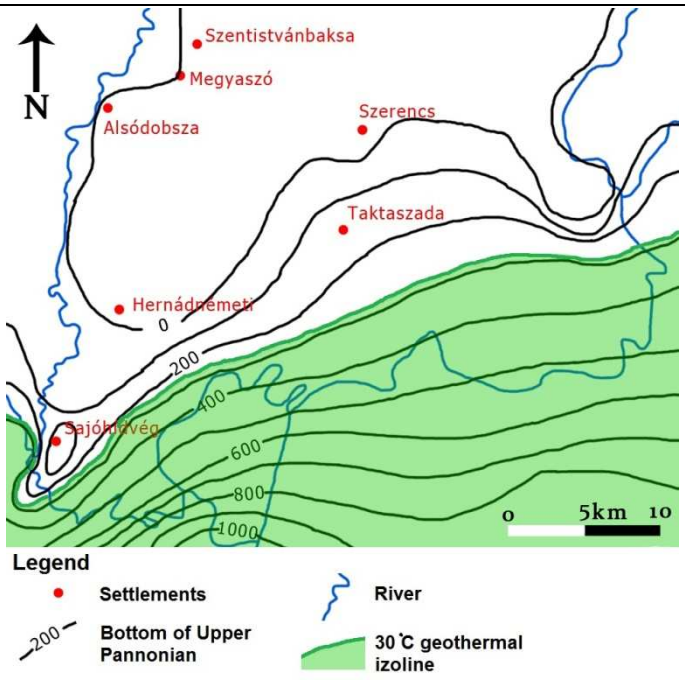

Figure 5.
Depth of the Upper Pannonian formations in the southern part of the Tokaj Mountains

- The temperature of the water in the quartzite strike is approximately 30 °C, with a yield of 1500–1700 l/min.

DISCUSSION

The calculated geothermal gradient value corresponds to the geo-isotherm map of Dövényi and Horváth [9]. The geothermal gradient value is 6.5–7 °C/100m on the geo-isotherm map. It gives good agreement with the calculated value. Many hydrogeological parameter values of volcanic formations were collected from the literature. The most important measurements were the hydraulic conductivity, permeability and transmissivity of the lava rock aquifers. The transmissivity of subvulcanic andesite is in the range of 2.7×10^{-6} – 4×10^{-4} m^2/s [3] (318 p.). Szilágyi [10] determined this value to be between 10^{-9} and 5×10^{-5} m^2/s. The hydraulic conductivity value of the lava rocks proved that the andesite formation is solid, and contains micro-fissures *(Figure 6)* [11]. We have compared the results with the measured values of Szűcs and Ritter [7], and according to these data the equivalent hydraulic conductivity of tuff for the investigated area is 0.85 m/d. Our measured values agree well with those in the literature.

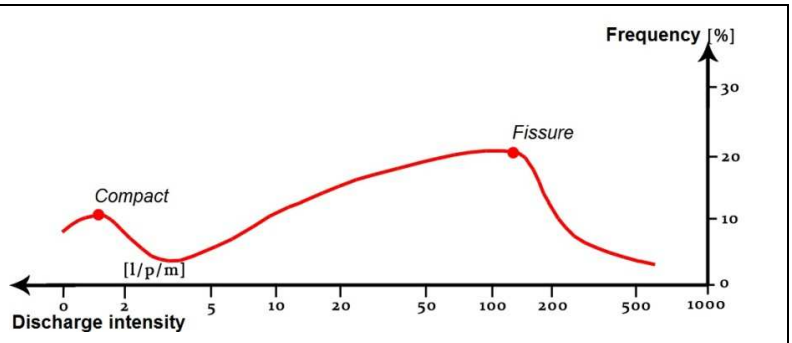

Figure 6.
Discharge intensity in lava rocks

CONCLUSIONS

The Tokaj Mountains have the most complex structure of any of the mountains in Hungary. Until now, the Tokaj Mountains were not the main target of warm water exploration, due to the poor hydraulic information on the formations and the large thickness of the volcanic sequence.

However, the different geophysical methods and the wells screened in the Pannonian, Miocene and Karst aquifers proved that we can discover warm-water aquifers with sufficient geological and hydrogeological properties within the investigated area.

LIST OF SYMBOLS

Variable	Name	Unit
z	depth	[m]
gg	geothermal gradient	[°C/100m]
gg*	geothermal step	[m/°C]
H	static water level	[m]
h*	cooling	[°C/100m]
h_0	measured water level in the well	[m]
k	hydraulic conductivity of aquifer	[m/s]
l	thickness of the screened layer	[m]
m	thickness of the aquifer layer	[m]
R	distance from piezometer to the pumping well	[m]
r_0	radius of the pumping well	[m]
s_0	depression	[m]
T_{out}	effluent water temperature	[°C]
T_z	bottom-temperature	[°C]

ACKNOWLEDGEMENT

The described work was carried out as part of the TÁMOP-4.2.2/B-10/1-2010-0008 project in the framework of the New Hungarian Development Plan. The realization of this project is supported by the European Union, co-financed by the European Social Fund.

REFERENCES

1. Kiss G.: *A Zempléni Tájvédelmi Körzet; A hegység elnevezése, lehatárolása és tájai*. Eger, Bükki Kiadó, 2007, 9–12.
2. VKKI–ÉKÖVIZIG: *Vízgyűjtő gazdálkodási terv,* 2–5. Tokaj-hegyalja, 2010.
3. Juhász J.: *Hidrogeológia*. Budapest, Akadémiai Kiadó, 2002.
4. Bobok E.–Tóth A.: *Megújuló energiák*. Miskolci Egyetemi Kiadó, 2005, 149.
5. Szűcs P.–Fejes Z.–Szlabóczky P.: *Melegvízkutatás nagymélységű adathiányos környezetben Szerencs térségében.* Szolnoki Főiskola, Műszaki Tudomány az Észak-Kelet Magyarországi Régióban 2012 Konferencia, ELEKTRONIKUS MŰSZAKI FÜZETEK 11: 303–313.
6. Lénárt L.: *Hévíz feltárására vonatkozó megvalósíthatósági tanulmányterv Vajdácska területére*. Miskolc, Karsztvízgazda Bt., 2008.
7. Szűcs P.–Ritter Gy.: *Sárospatak-Végardó termálfürdő hévízkútjainak hidrodinamikai modellezése*. Csíkszereda, A Kárpát-medence ásványvizei: V. nemzetközi tudományos konferencia, 2008, 51–61.
8. Csíky G.: *Magyarország Pannóniai (S. L.) képződményei*. Budapest, MÁFI, 1987.
9. Dövényi, P.–Horváth, F.: *Map of geoisotherms at 1000m depth in the Pannonian Basin*. Budapest, ELTE, 1982.
10. Szilágyi G.: A recski mélyszinti ércesedés helyzete. *Földtani Közlöny,* 105. évf., 1975, 740–754.
11. Deák J.–Szlabóczky P.: *Borsod és Környékének Vízföldtani Atlasza*. Budapest, 1987.

Geosciences and Engineering, Vol. 2, No. 3 (2013), pp. 111–116.

VACUUM ENHANCED COMPRESSION OF RECSK TYPE FLOTATION SLURRY

NÓRA GONDA–BALÁZS KOVÁCS
Department of Hydrogeology and Engineering Geology,
Institute of Environmental Management
University of Miskolc

ABSTRACT

Several significant types of environmental damage were caused by copper ore mining in Recsk; therefore, remediation of the area is important. The ore was processed using flotation technology; the flotation slurry was deposited at several sites decades ago, but its moisture content has not changed significantly since then. The dumps formed using this material have low stability, which is a significant problem for remediation work when temporary slopes are formed. Thus the investigation of the water-releasing capability of the slurry is very important, as well as the comparison of the behavior of the dewatered slurry. Oedometer tests and shear tests were carried out on samples, some of which were dewatered. The oedometer tests showed that the compressibility due to vacuum dewatering of the slurry did not change significantly. This result was confirmed by the results of the shear tests, where almost the same cohesion and angle of internal friction were measured. Thus dewatering alone is not enough to improve the bearing capacity of the flotation slurry, and other supplementary methods will be needed to stabilize the site.

INTRODUCTION

The mining of copper-containing ores in the Recsk area began in the 19th century [1]. In 1925 a flotation unit started to help the production that produced a large volume of flotation sludge with high heavy-metal content [2]. The slurry was deposited into several deposits that are nowadays active pollution sources, where the remediation is required. The slurry has very special geotechnical behavior; therefore, a straightforward investigation of the material was performed. During the investigations the material was investigated also in its natural condition, where due to its high sorbed water content the deformability was found to be very high while the bearing capacity was very low. The very low permeability of the sludge hinders the reduction of moisture content, but the construction work planned to be done at the site during the remediation require the slurry to be dewatered.

The aim of this paper is to present the recent geotechnical characteristics of the slurry and to focus on the possibilities for "reinforcing" the material through dewatering and artificial compaction. We performed vacuum procedure to extract a part of the water content of the slurry and we made some comparative geotechnical shearing and oedometric tests to evaluate the changes in compressibility and shearing resistance of the material.

The investigations presented provide some additional information that will be of use when designing the remediation of the site in the near future.

MATERIALS AND METHODS

To investigate the problem, tests of water adsorption capacity, the dewatering characteristics at vacuum and bearing capacity were performed. The bearing capacity of a material can be characterized by its compressibility and shear resistance; therefore, oedometer and direct shear tests were carried out.

Due to the very fine grain size and the low permeability the "natural" water content of the slurry is high (w ≈ 40%). The bearing capacity of the fine-grained materials is influenced by the moisture content; thus, we investigated the water absorption capacity of the slurry. The water absorption capacity is the amount of water which the fine grains (d < 0.06 mm) can absorb at dry condition, which can be measured using the Enslin apparatus (*Figure 1*).

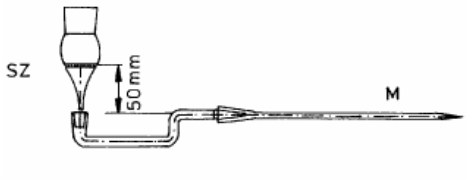

Figure 1.
Enslin apparatus

Dewatering by vacuum wells

Vacuum wells can be used effectively for the reduction of water content of fine-grained materials. Compared to gravity-driven dewatering, not only the gravitational force takes part in the development of the depression but also the effect of the vacuum (negative relative pressure) evolves suction of the pore water. Another advantage of the vacuum well is that it may stabilize the wall of a possibly existing open pit due to the seepage opposite to the potential sliding direction.

Figure 2 shows the vacuum system which we constructed in the laboratory:

1. vacuum pump
2. pressure receptacle
3. pressure sensor
4. precipitating vessel
5. sample (with membrane isolation)

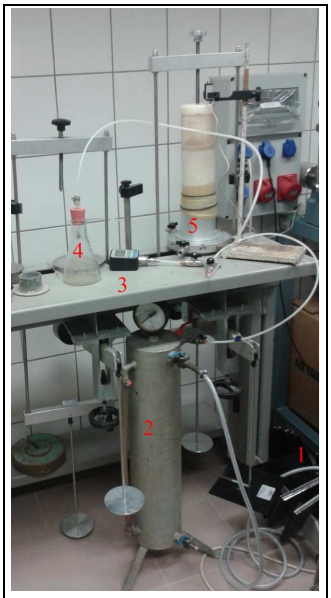

Figure 2.
Dewatering by vacuum

Figure 3.
The oedometer

Oedometer tests

The compressibility of the different materials can be characterized by oedometric tests where the function of the Δh / h unit strain versus normal load function is determined in a rigid cylinder, where h is the sample height and Δh is the change of the height at a given load [3, 4]. The equipment is shown in *Figure 3*.

Direct shear tests

The shear strength of the materials can be characterized by the Coulomb equation:

$$\tau = \sigma \, tg\varphi + c \quad (1)$$

In the equation the c and φ are material properties which are called shear strength parameters. According to Coulomb, the failure of the material is caused by the friction between the particles and the cohesion being exceeded by the shear stress [5].

Figure 4.
The shearing machine

During the shear box test, the shear takes place along a predefined surface while the sample body is loaded vertically with a given amount of force. Both the deformations and the horizontal shear force are measured. The shear box used in the test is shown in *Figure 4*.

Both the different shear and normal stresses are measured simultaneously, and are plotted using the σ – τ coordinate system. The failure line is determined by a linear fit plotted on the measurement data, the internal friction angle is given by the slope of this linear fit and the cohesion is determined by the intersection with the y axis.

RESULTS

The results of the water absorption capacity tests are shown in *Table 1*.

Table 1

Water absorption capacity of the investigated material

Recsk type flotation slurry (Maximal water absorption capacity: **40.83**%)					
Elapsed time [s]	**15 sec**	**30 sec**	**1 min**	**2 min**	**4 min**
Test 1. [ml]	0.215	0.34	0.41	0.37	
Test 2. [ml]	0.23	0.34	0.41	0.385	
Test 3. [ml]	0.21	0.31	0.38	0.405	0.35

During the oedometer tests the sample body has been vertically loaded stepwise and the vertical deformations have been recorded (*Figure 5*). The result of the measurement is the compression curve, which can be obtained if the maximum values of the unit strains at each loading steps are plotted as a function of the σ normal stresses.

This is shown in *Figure 6* at the "natural" (cca. 40%) moisture content. Samples of 20 and 44 cm^2 cross section were measured in several repetitions. The compression curve was drawn based on the average of several measurements.

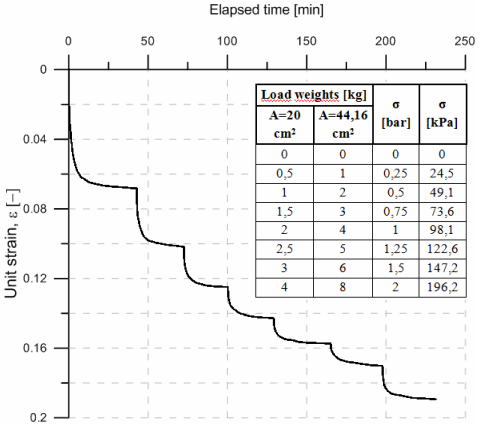

Load weights [kg]		σ	σ
A=20 cm²	A=44,16 cm²	[bar]	[kPa]
0	0	0	0
0,5	1	0,25	24,5
1	2	0,5	49,1
1,5	3	0,75	73,6
2	4	1	98,1
2,5	5	1,25	122,6
3	6	1,5	147,2
4	8	2	196,2

Figure 5.
The relation between time and unit strain (ε) and the applied loading steps

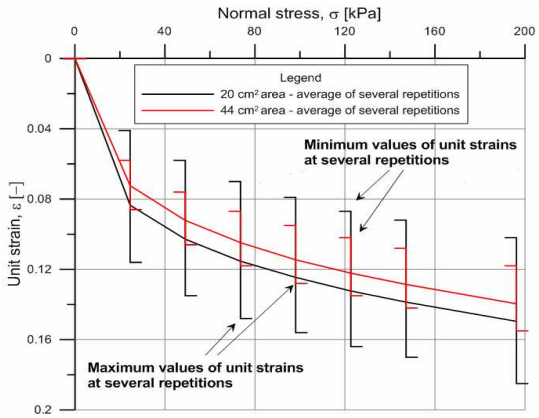

Figure 6.
The compression curve of the flotation slurry at "natural" (~ 40%) moisture content using different sized oedometers

The compressibility of the same slurry material was also determined after applying 2 hours of vacuum at different intensity (0, 40, 65, 90 kPa), which resulted in a reduction of moisture content and increase in the initial level of compaction.

The results of one-loading-step oedometer tests are shown in *Figure 7.* The normal load corresponds to the pressure applied to the slurry by the coverage clays at the original deposit.

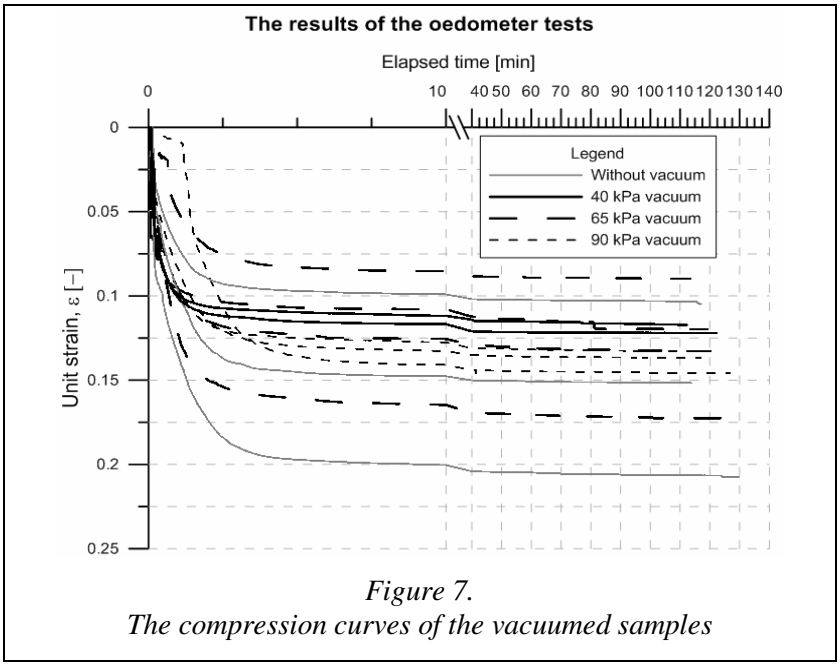

Figure 7.
The compression curves of the vacuumed samples

During the shear box tests, the shear strength parameters of the Recsk flotation slurry were investigated at two moisture levels. In the first series of measurements the samples from the test area were investigated at the "natural" (~ 40%) moisture content, in the second one the samples were tested after 2 hours of vacuum dewatering at 90 kPa.

In both cases the samples were consolidated for 1 hour at different normal stresses in the 70–200 kPa range. The results of shear box tests are shown in *Figure 8*.

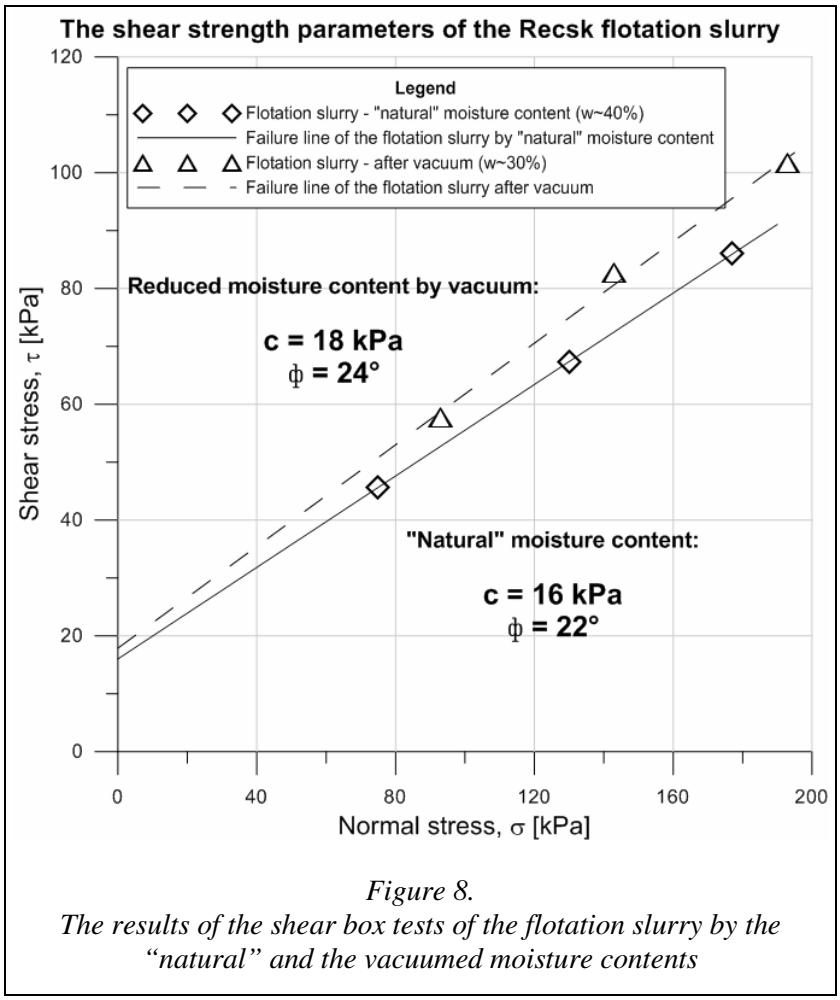

Figure 8.
The results of the shear box tests of the flotation slurry by the "natural" and the vacuumed moisture contents

DISCUSSION

According to the results of the tests using the Enslin apparatus, the water absorption capacity of the flotation slurry is rather high. The sorbed water on the grains interface is difficult to remove, as shown by the water content of the vacuumed samples. After the 90 kPa vacuum dewatering the moisture content of the sludge reduced from 40% to 30% (*Figure 8*).

Based on the results of the oedometer tests (*Figure 7*) it could be proven that the dewatering by vacuum slightly affects the compressibility, but this cannot be accepted as the main factor influencing the consolidation procedure of the slurry.

The results of shear box tests show that the vacuum handling of the sludge raised the shear strength of the slurry a bit, but the change from a geotechnical point of view is almost irrelevant.

The tests performed prove the fact that the low shear resistance of the sludge is assured not by its high water content but by the presence of the different surfactants that are bounded chemically to the materials originated from the original processed ore. This explains why dewatering alone cannot be enough to increase the stability of the sludge. Dewatering must be applied in addition to chemical treatment that destroys the structure of the slurry and that compensates for the charges on the surface of the grains.

CONCLUSIONS

Although the flotation slurry was deposited in the Recsk area decades ago, its moisture content is still very high. The low stability of the material poses a significant problem during remediation. A comparison was made of results for dewatered slurry from oedometer and shear tests. From the results of the oedometer tests, it can be determined that the compressibility due to vacuum dewatering of the slurry did not change significantly. Shear test results confirm this finding, since cohesion and the angle of internal friction of the compacted slurry was measured in the 16–18 kPa and in the 22–24° intervals, both at natural conditions and at vacuum-reduced water content. We conclude that dewatering is insufficient to ensure the stability of the slurry.

Other methods will be investigated for increasing stability at the remediation site. One approach is to develop a geotechnical model for the stability of slopes. Another possibility worth investigating is slurry-specific chemical treatment to destroy the existing structure of the material.

ACKNOWLEDGEMENT

The described work was carried out as part of the TÁMOP-4.2.2/A-11/1-KONV-2012-0049 project in the framework of the New Hungarian Development Plan. The realization of this project is supported by the European Union, co-financed by the European Social Fund.

LIST OF SYMBOLS

c	cohesion	kPa
ε	unit strain	-
σ	normal stress	kPa
τ	shear stress	kPa
φ	internal friction angle	°

REFERENCES

1. Csifáry G.: *Az ércbányászat története a recski Lahócában (1850–1979).* Ore- and Mineral Mining Museum Fundation Rudabanya, Z-press Publishing and Printing Ltd., Miskolc, 2009, 143.
2. Földessy, J.–Szebényi, G.: "The mineralizations of Recsk deeps and Lahóca – short geological overview." Geosciences, Recsk and Lahóca geology of the paleogene ore complex, Series A, Mining, Volume 73, University of Miskolc, 2008, 87–100.
3. Kézdi, Á.: "Soil Mechanics I.", Talajmechanika, Budapest, 1972.
4. Szabó, I.–Faur, K.: "Geotechnika." Digital interactive lecture notes, Faculty of Earth Science and Engineering, University of Miskolc, 2011. (http://digitalisegyetem.hu/elearning/contents.php?subject_ID=MFKHT6504SI)
5. Szepeshazi, R.: *Geotechnika*. Győr, 2008, 41–3. (http://www.sze.hu/~szepesr/anyagok/oktatas/SZR-GEO-2010mm.pdf)

Geosciences and Engineering, Vol. 2, No. 3 (2013), pp. 117–123.

BIOENERGY PRODUCTION IN MÁTRA POWER PLANT

TORSTEN HAUCK
Mátrai Erőmű Plc.,
member of the Board of Directors

ABSTRACT

The paper presents the establishment conditions of energy crop (false acacia) plantations on the recultivated opencast stockpiles (K-I, K-II mines) of Mátrai Erőmű Plc., the agro technical solutions of the planting and treatment of the crops and the machinery of gathering. Specifications of the 'fuel' produced, the utilization parameters of the amount produced (heat amount, electricity produced), the costs incurred in the years 2006–2010, the revenue derived from the sales of electricity and CO_2 quota savings, and the rate of return of 'investment' are given. Future plans of bioenergy utilization are also referred to.

1. INTRODUCTION

1.1. Preliminaries

Mátrai Erőmű Public Limited Company, as one of the largest carbon dioxide emitters in Hungary, has faced a new challenge with the resolution of the Council of the European Union, according to which Hungary should increase the rate of renewable energies in its energy balance to 13% by 2020, which amounts to about 20% in the case of electricity production. At the same time, this requirement has provided a motivation to exploit new opportunities offered by renewable energy sources. The company, possessing two opencast brown coal mines, regarded the elaboration of the condition system of biomass co-firing and the introduction of this technology as an obvious solution to considerably increase the rate of electricity coming from renewable energy sources.

The legal environment prefers small power plants with combined heat power and of an output below 50 MW. However, recent public protests have routinely made it impossible to establish such power plants. The experts of Mátrai Erőmű Plc. were seriously concerned with the idea of establishing an energy crop plantation so they elaborated the technology of biomass co-firing. Both the experts in the power plant and in the mine were aware of the fact that electricity produced from plants may only be competitive if the company can purchase the base material at the most favorable price possible and there is a relatively short distance between the places of establishment and processing of the plantation.

In awareness of all these facts, the company decided to examine the quality parameters of the large and flat mining areas already abandoned and technically recultivated, and if they proved to be suitable for the planting of energy crops, the company decided to start the licensing procedures necessary for practical implementation. The place of processing the vegetable base material coming from the plantation was marked out in the close neighborhood of the company site already in the planning phase [1].

2. MATERIALS AND METHODS

2.1. Starting the experiment in the framework of recycling

In the possession of the necessary licenses, Mátrai Erőmű Plc. established an experimental energy crop plantation of 20 hectares in the uncultivated stockpile area of mine K-II at the end of 2006, On the one hand, the objective of the experiment was to determine the growth potential of the plantation, and, on the other hand, to create a solid basis for the future decisions to establish plantations of even greater areas. For the first time, Mátrai Erőmű Plc. was awarded a license for the energetic utilization of biomasses until 31 December, 2010. This license has been extended until 31 December, 2015.

During their post-utilization of landscape, mines mostly apply the usage mode of afforestation as in the course of stockpile construction, such landforms (slopes) also come into being for which afforestation is the most suitable form of utilization from the point of view of erosion protection. In line with its landscape planning tasks, the Company makes an effort to perform landscape rehabilitation, keeping the local needs of the neighboring settlements in mind in order to reduce environmental pollution. The result of the enhanced rate of forest area is that it is the forest that utilizes areas of reduced productiveness with the greatest efficiency. In its recent recultivation activities, the Company has mostly used false acacia to afforest stockpile and slope surfaces but in the last years it has planted several other indigenous trees in both mining areas (such as e.g. aspen, weeping birch, blackthorn, field maple, Tatar maple, Cornelian cherry, goat willow, oak, sessile oak, brambleberry), thus improving the planting rates of the tree species in the present continuous biological landscape planning. At present, this rate is 70% in favour of the planting of non-alien, indigenous tree species.

2.2. Major considerations in the selection of the species to be planted and in that of the area

The tree species planted on the stockpile of mine K-II in autumn 2006 was determined by the soil quality in the 20 hectare area marked out for this purpose. In general, the soils are slightly alkaline and calciferous. Their lime content rarely reaches the amount of soil deficiency although physiological drought should be taken into account due to the presence of limestone. The soils of the areas are characterized by loam and clay texture, which means good water holding capacity and hydraulic conductivity. The soil of the stockpile is poor in black mould and has a low nutritive content. Its surface has an inhomogeneous structure. It is rough. Mostly, machines can move on it. In some sunken patches, stagnant water can be found.

The expert team found false acacia (Latin name: Robinia pseudoacacia), a tree species belonging to the family papilionaceae, most suitable for planting. This tree species, indigenous in North America, was first planted in Hungary in the 18th century to bind the sand. As regards its biological characteristics, it is a long-living, fast-growing tree species. It requires warmth and light, it is sensitive to freezing weather, bears drought well and shoots easily. With the help of the azotobacters living on its roots, the false acacia is capable of binding vital nutritive elements from the air, thus improving the nutritive level of the soil. Due to these biological and ecological characteristics, the false acacia proved to be the optimum choice.

2.3. Planting parameters and major cultivation characteristics of the plant

The steps and devices of the technological process applied during planting and those of treatment are presented in the following brief summary:

- Species applied: False acacia, Robinia pseudoacacia
- Count: 8,400–8,500 pcs/hectare
- Row space: 3,00 meters
- Stock space: 0.40–0.50 meter (planting with wedge-shaped hand spade)
- Planting roster: 3.0 m x 0.48 m
- Preparation of soil: the surface affected by plantation of the technically arranged area was ploughed 30 cm deep at the end of summer and in autumn (in October). This was followed by closing the soil surface (harrowing, smoothing) and then fertilization was done. With this, the soil became suitable for planting (*Figure 1*).
- Planting: following the manual marking out of row space, at the distance of every 3.0 meters, a planting ditch was made. Then 1/0[1] sapling per bed was planted with wedge-shaped hand spade. Before planting, any injured roots were cut back.
- Fertilization: in the case of litho soils, poor in black mould, nutritive supply is absolutely necessary. Upon planting, 10 quintals of combined fertilizers (N 33%, P 33%, K33%) were placed per hectare next to the planted saplings followed by the cutting back of the stems of the planted saplings on soil surface level.
- Treatment: in the first vegetation year following planting, earthing was done in the rows (hoeing at the stems of saplings), and harrowing was done between the rows. Treatments between the rows should be repeated according to the level of weeding. In general, three treatments between the rows are necessary per year. Gap filling: if any saplings are missing in the rows after the first planting, these gaps should be filled with 1/0 sapling per bed before the start of the second vegetation period.
- Further treatments: hoeing, harrowing or mowing between the rows at least twice in the second vegetation period. In the third vegetation year, it is recommended to do harrowing or mowing between the rows at least twice.

In the fourth vegetation year, no further treatments are necessary. Following the end of vegetation, wood may be gathered depending on the size of growing stock (*Figure 2–3*).

Figure 1.
Preparation of plantation area

[1] one-year old root system (1), cut back (0)

Figure 2.
False acacia saplings in plantation

Figure 3.
False acacia plantation ready for gathering

2.4. Legal status of the areas selected for plantation

Relying on the experience with the first 20 hectare energy forest, planted as a pilot project in 2006, in 2010, Mátrai Erőmű Plc. decided on establishing a further experimental 100 hectare ligneous energy crop plantation, thus underlining the necessity of biomass production. We had surfaces suitable for energy crop plantation in 80 hectares in mine K-II in Visonta, in 20 hectares in stockpile K-I and in 20 hectares in the northern stockpile surface of Bükkábrány mine. The contractors capable of the implementation of the establishment of ligneous energy crop plantations were selected in a tender.

The areas of Mátrai Erőmű Plc. covered with energy crop plantations are put into the uncultivated category according to the land registry. Both the Visonta and Bükkábrány energy crop plantations were reported to the relevant county forestry directorates. Following the closure of the necessary procedures, the directorates issued a ruling about the acknowledgement and registration of these energy crop plantations.

2.5. Technological description of the establishment of energy crop plantations

In the stockpile surface of mine K-II, 60 hectares and in 2011, 20 hectares of energy crops were planted. 8,500 pcs/hectare, altogether 680,000 saplings were planted in the area. The data concerning planting and the treatment of plantations are summarized in Table 1. The first row of the table includes the establishment and treatment costs broken down to years of the 20 hectare energy crop plantation, planted in December 2006 as a pilot project. As these crops have already been gathered, the table includes these costs, as well. The experience gained during the establishment, treatment and harvesting of the first crops provided useful information for the later plantations (for example, the determination of actual growth potential and the increase of the original 3 m row space to 4 m due to machine gathering). Figure 2 shows the growing false acacia saplings.

2.6. The mechanical system of first gathering

The experimental crops were machine gathered in February 2010. A specialized external company was also involved in the gathering. The necessary equipment was provided by the contractor so all the jobs were done in an integrated way. The harvester can be seen in Photo 4. It was a Jaguar 850 engine. Moving along the rows of the plantation, the harvester, equipped with a special adapter, cut the plants from the stems with 2 rotating-cutting plates. The feed system of the adapter pulled the cut stalks into the mincer, cut them up and then

blew the minced coil into the lorry standing next to the harvester (*Figure 5*). The grain size of the minced coil was in the range of few centimeters (*Figure 6*).

The optimum time of harvesting is always the end of the vegetation period (wintertime) as without foliage, the plant has low water content, resulting in higher heating value.

Table 1

Table summarising the costs related to the establishment, treatment and harvesting of the plantation [thousand HUF]

Phase	**Establishment**			**Soil preparation and planting costs**	**Treatment cost Year I**	**Treatment cost Year II**	**Gathering**	**Total**
	place	time	size		Treatment I + II + III	Treatment I + II		
Phase I	Stock-pile K-II	December 2006	20 hectares	10600	4200	3600	2140	20540
Phase II	Stock-pile K-I	December 2010	20 hectares	8530	3140	1040	-------	12710
Phase II	Stock-pile K-II	April 2011	20 hectares	7650	3140	1040	-------	11830
Phase II	Stock-pile K-II	December 2010	60 hectares	22950	9420	3120	-------	35490

Figure 4.
Harvester

Figure 5
Harvesting system (mincer and transporter equipment)

Figure 6.
Minced coil on transportation vehicle

2.7. Fuel parameters

The harvesting results of the minced coil coming from the first plantation are included in *Table 2*.

Table 2

Harvesting data of the first plantation

Harvesting of energy forest (false acacia) Results calculated for 20 hectares			
Samples	Heating value (kJ/kg)	Amount (t)	Heat amount (GJ)
1	12362	5.06	62.55
2	13496	112.78	1522.08
3	13311	80.81	1075.64
4	13631	153.35	2090.34
5	13441	74.86	1006.19
Total	**13486**	**426.86**	**5756.80**

3. RESULTS

3.1. Profitability expected from energy crop plantations

For making the decision to establish the plantation, it was not only necessary to present a process and set of tools of technological feasibility but the profitability of electricity production from the ligneous plants produced in the plantation had to be proved, too.

In order to filter out uncertainties and reduce risks as much as possible, the technical experts and economists of the Company made dynamic rentability calculations covering a longer period from 2006 to 2025. The calculations also took into account the effect of external market factors such as producer price index (PPI), CO_2 quota price and fluctuation in currency exchange rates. With the help of the technical parameters specified by power plant experts such as the average heating value, oxidation and CO_2 emission parameters of lignite, the amount of CO_2 quota that could be saved and the specific value of quota release were also determined. Specific costs were determined on the basis of the data supplied by mining experts such as the costs of country planning, area preparation, planting, treatment and gathering. As regards specific prices, the price of electricity in the competitive market, the premium takeover price of electricity produced from renewable energy sources and their expected changes were determined in accordance with forecasts. Revenues included the sales returns of electricity produced at an ordinary price and those of green electricity, supported by law, and the savings of CO_2 quota costs.

Even preliminary rentability calculations revealed the fact that the profitability of energy crop plantations was fundamentally determined by two factors:

- the specific price of carbon dioxide quota, which cannot be determined precisely due to the changes in demand and supply,
- the premium takeover price of electricity produced from renewable energy sources, which is significantly higher than the price of ordinary electricity.

In addition to the above, it is yield from the gathered plants, that is, the heat amount that affects profitability. In case of unfavorable weather, yield may be reduced even with proper treatment. Preliminary dynamic rentability calculations prognosticated a 7% expected yield, which indicated a positive result even in consideration of all the risk parameters.

3.2. Cost-benefit analysis on the basis of harvesting results

The cost-benefit analysis was made on the basis of facts and figures following the harvesting of energy crops from the plantation established in phase I. This contrasted the costs of the period between the establishment and harvesting of the plantation (2006–2010) with the revenues of the same period. One of the most important figures in the calculations is that the heat amount of the biomass/minced coil gathered in the 20 hectare area was 5,716 GJ, of which the amount of saved CO_2 quota was 6,506 tons, taking the values of CO_2 emission and oxidation factors into account.

The establishment costs of the plantation in 2006 were 10,600 thousand HUF, the costs of cultivation and treatment in 2007 were 4,300 thousand HUF, the costs of treatment in 2009 were 3,600 thousand HUF and the 2010 'gathering' costs amounted to 2,140 thousand HUF. [2] The revenues of the plantation come from two sources: one is the value of carbon dioxide quota savings, expressed in HUF, and the other is the revenue of green electricity, which means a significantly higher takeover price of 28.7 HUF/kWh in comparison with the 18 HUF/kWh takeover price of ordinary electricity. The revenue in 2010 from 440 MWh green electricity was 12,619 thousand HUF with 21,469 thousand HUF as CO_2 quota savings.

On the basis of the assessment of the rate of the result of the investment in phase I and all the expenses incurred to achieve this result, CF balance amounted to 31,948 HUF and the internal rate of return was 13% so the actual yield of the plantation was 13%. The efficiency of the investment was positively influenced by the fact that the actual growth potential of the plantation was more favorable than expected so harvesting could be done at the end of the fourth year instead of the fifth year as expected.

4. CONCLUSIONS

Dumps of open cast coal mining are suitable for plantation intended for energetic purposes after technical and biological land reclamation. The energy crops can be optionally fast-growing acacia plantation. The planting and maintenance as well as harvesting and grinding are possible using common agricultural technology. The efficiency of consumption/heating together with the saving of CO_2 quota ensures cost-effective electricity generation.

ACKNOWLEDGEMENT

This work was carried out as part of the TÁMOP-4.2.1.B-10/2/KONV-2010-0001 project in the framework of the New Hungarian Development Plan. The realization of this project was supported by the European Union and, co-financed by the European Social Fund.

REFERENCES

1. Dinya, L.: Biomassza-alapú energiatermelés és fenntartható energiagazdálkodás. *Magyar Tudomány*, 2010/8. pp. 912–919. HU ISSN 0025 0325
2. Kovács, F.: "Coal Rates in Electricity Production: The Reality of Climate Causes." ARPN Journal of Science and Technology, Vol. 2. No. 10. Nov. 2012. pp. 976–981. ISSN 2225 7217

University of Miskolc, Department of Research Management and International Relations
Responsible for publication: Prof. Dr. Kékesi Tamás
Miskolc-Egyetemváros
Published by the Miskolc University Press under leadership of Erzsébet Burmeister
Editor: Balsai Gyula Pálné

Put to the Press on 2013

HU ISSN 2063-6997